Electronic Structures of Novel Quantum Materials Studied By Spatially Angle-Resolved Photoemission Spectroscopy

Cheng Chen

St Cross College

University of Oxford

A thesis submitted for the degree of

Doctor of Philosophy

Trinity 2018

Electronic Structures of Novel Quantum Materials Studied By Spatially Angle-Resolved Photoemission Spectroscopy

Cheng Chen, St Cross College, Oxford

Thesis submitted in fulfilment of the requirements for the degree of Doctor of Philosophy at the University of Oxford. Trinity, 2018

Abstract:

This thesis describes the studies on the electronic structures of several novel quantum materials by using the Angle-Resolved Photoemission Spectroscopy (ARPES) technique:

1. Topological Dirac semimetals represent a new state of quantum matter that offers a platform for realizing many exotic physical phenomena. Our ARPES experiment systematically revealed the electronic structures of *M*SiS (*M*=Zr, Hf) family and confirmed the Dirac line-nodes states in both compounds. By comparing the spin-orbit coupling (SOC) effect, we demonstrated that the degeneracy of bands at certain positions of Brillouin zone (BZ) are protected by non-symmorphic symmetry of the crystal.

2. Two dimensional (2D) semiconductors with high carrier mobility and moderate band gap are particularly attractive for their potential broad applications in electronic devices. By using both ARPES and scanning tunneling microscopy (STM) techniques, we comprehensively revealed the electronic structure of newly discovered air-stable oxide semiconductor Bi_2O_2Se. Surface patterns (consisting of 50% Se vacancies) were found on the cleaved sample surface. Remarkably, we found no evidence of undesired in-gap states even in the presence of these surface defects.

3. Spatially resolved ARPES technique has been recently developed, which features its ability to focus the incident beam into submicron region. By using the technique, we studied the electronic structure of square graphene system. The sides of the graphene are found to be aligned with underlying Cu <110> direction, indicating the important role of substrate during the growth of graphene. In addition, large domain twisted bilayer graphene (tBLG) was artificially constructed. The van Hove singularity in its band structure caused by interlayer interaction was directly revealed by our ARPES measurement.

Acknowledgement

The last four years of DPhil study in Oxford have been an incredible time in my life and I will cherish it forever. I am more than glad to see that I have accomplished it. This work would not have been possible without all the support I have received. Here I would like to take this opportunity to express my sincere appreciations to all those who have helped me throughout this long journey.

I would like to begin by expressing my deep gratitude to my supervisor, Yulin Chen, for always inspiring me, encouraging me, and supporting me throughout my entire study in Oxford. I have been extremely lucky to have a supervisor who cared so much about me and my work. He has taught me more than I could ever give him credit for. Everything from gluing the sample to writing the paper, which made me become a skilled experimentalist and more importantly, an independent thinker. His incredible physics intuition and enthusiasm on the scientific researches has greatly motivated me.

I would also like to thank Thorsten Hesjedal and Cephise Cacho for being the examiners of my thesis, which I really appreciate.

My colleagues at Chen's group in Oxford: Han Peng, Niels Schroeter, Sandy Ekahana, Yiwei Li, Ding Pei and Chaofan Zhang- ensured I was constantly engaged and entertained along the way. I cannot thank our exceptional friendship enough. Also, I would like to thank all the senior members in the big Chen's group in China: Zhongkai Liu, Lexian Yang, Meixiao Wang, Juan Jiang, Haifeng Yang, Aiji Liang, Defa Liu, and Shengtao Cui. I am grateful that I had the opportunity to get involved in different amazing research projects which open up my mind. Thanks to all the graduate students: Xu Xiang, Lei Shen, Yujie Chen, Shucui Sun from Tsinghua University and Chengwei Wang, Tao Deng, Shuai Liu from Shanghai Tech University, for all your assistance and collaboration during the beamtimes and data analysis.

I am grateful to all of those with whom I have had the pleasure to work with during related projects. Friends in Clarendon Laboratory has provided me extensive professional guidance on my research. I still remember that Jian Huang patiently taught me how to use the EBL and AFM; Shilei Zhang helped me with XRD experiment; Dharmalingam Prabhakaran always provides me fantastic single crystal samples; Penglin Cai always shares his understanding on transport measurement.

Besides, I am also very grateful for all the support from the scientists at I05 beamline, Diamond Light Source: Moritz Hoesch, Pavel Dudin, Timur Kim and Hideaki Iwasawa. You have made one of the greatest high-resolution ARPES end station in the world with an incredible level of automation. The same thanks goes to the scientists at Spectromicroscopy, Elettra synchrotron: Alexey Barinov, Viktor Kandyba, and Alessio Giampietri. The unique spatially resolved ARPES system developed serves to be a pioneer in the field. Your patience and enthusiasm made my every beamtime a pleasant journey.

My thanks are also due to all our collaborators outside Oxford, for providing the amazing samples, performing STM and transport experiments, and carrying out theoretical calculations. They are, Hailin Peng's group from Peking University, Yanbin Chen, Shuhua Yao and Hongyao Yuan's group from Nanjing University, Chunlan Wu from Stanford University, Jianmin Xue's group from Shanghai Tech University, Yan Sun and Binghai Yan's group from Max Planck Institute.

In particular, I wish to acknowledge with gratitude the financial support from China Scholarship Council - University of Oxford Scholarship.

Nobody has been more important to me in the pursuit of this thesis than the members of my family. I wish to thank my parents, Shengjun Chen and Hong Xia, for their unconditional love and tremendous support. The harmony of the family has greatly shaped my personality and gave me the strength to face all the difficulties and hardships in my life.

Finally, I would like to thank my fiancée, Meidi Li, for her understanding and support. My life has always been full of sunshine since the first day I met you.

Publications

(2016-present, Total citation: 335)

Chapter 1:

1. Haifeng Yang, Aiji Liang, **Cheng Chen**, Niels B.M. Schroeter and Yulin Chen
   "Visualizing Electronic Structures of Quantum Materials by Angle-resolved Photoemission Spectroscopy"
   Under review in Nature Reviews Materials

Chapter 2:

2. **C. Chen**, X. Xu, J. Jiang, S. -C. Wu, Y. P. Qi, L. X. Yang, M. X. Wang, Y. Sun, N.B.M. Schröter, H. F. Yang, L. M. Schoop, Y. Y. Lv, J. Zhou, Y. B. Chen, S. H. Yao, M. H. Lu, Y. F. Chen, C. Felser, B. H. Yan, Z. K. Liu and Y.L. Chen
   "Dirac Line-nodes and Effect of Spin-orbit Coupling in Non-symmorphic Critical Semimetal MSiS (M=Hf, Zr)"
   Physcal Revivew B, 95, 125126 (2017)

3. Guang-Hao Hong, Cheng-Wei Wang, Juan Jiang, **Cheng Chen**, Sheng-Tao Cui, Hai-Feng Yang, Ai-Ji Liang, Shuai Liu, Yang-Yang Lv, Jian Zhou, Yan-Bin Chen, Shu-Hua Yao, Ming-Hui Lu, Yan-Feng Chen, Mei-Xiao Wang, Le-Xian Yang, Zhong-Kai Liu, Yu-lin Chen
   "Measurement of the bulk and surface bands in Dirac line-node semimetal ZrSiS"
   Chinese Phyiscs B, 27, 017105 (2018)

Chapter 3:

4. **C. Chen**, M.X. Wang, J.X. Wu, Y. Sun, H.F. Yang, Z. Tian, T. Tu, H. Peng, G. Li, H.X. Fu, X. Xu, J. Jiang, N.B.M. Schröter, Y.W. Li, D. Pei, S. Liu, S.A. Ekahana, H.T. Yuan, J.M. Xue, J.F. Jia, Z.K. Liu, B.H. Yan, H.L. Peng and Y.L. Chen
   "Electronic Structures and Unusually Robust Bandgap in a High Mobility Layered Oxide Semiconductor, Bi_2O_2Se"
   Under review in Science Advances

5. Jixiong Wu, Hongtao Yuan, Mengmeng Meng, **Cheng Chen**, Yan Sun, Zhuoyu Chen, Wenhui Dang, Congwei Tan, Yujing Liu, Jianbo Yin, Yubing Zhou, Shaoyun Huang, Hongqi Xu, Yi Cui, Harold Hwang, Zhongfan Liu, Yulin Chen, Binghai Yan, and Hailin Peng
   "High electron mobility and quantum oscillations in non-encapsulated ultrathin semiconducting Bi_2O_2Se"
   Nature Nanotechnology, 12, 530 (2017)

Chapter 4:

6. H. F. Yang*, **C. Chen***, H. Wang*, Z. K. Liu*, T. Zhang, H. Peng, N.B.M. Schröter, S. A. Ekahana, J. Jiang, L. X. Yang, V. Kandyba, A. Barinov, C. Y. Chen, J. Avila, M. C. Asensio, H. L. Peng, Z. F. Liu and Y. L. Chen
* These authors contributed equally to this work
"Single Crystalline Electronic Structure and Growth Mechanism of Aligned Square Graphene Sheets"
APL Materials 6 (3), 036107 (2018)

7. Zhenjun Tan*, Jianbo Yin*, **Cheng Chen***, Huan Wang, Li Lin, Luzhao Sun, Jinxiong Wu, Xiao Sun, Haifeng Yang, Yulin Chen, Hailin Peng, Zhongfan Liu
* These authors contributed equally to this work
"Building Large-Domain Twisted Bilayer Graphene with van Hove Singularity"
ACS Nano, 10, 6725 (2016)

8. Huan Wang, Xiaozhi Xu, Jiayu Li, Li Lin, Luzhao Sun, Xiao Sun, Shuli Zhao, Congwei Tan, **Cheng Chen**, Wenhui Dang, Huaying Ren, Jincan Zhang, Bing Deng, Ai Leen Koh, Lei Liao, Ning Kang, Y. L. Chen, Hongqi Xu, Feng Ding, Kaihui Liu, Hailin Peng, Zhongfan Liu
"Surface Monocrystallization of Copper Foil for Fast Growth of Large Single-Crystal Graphene under Free Molecular Flow"
Advanced Materials, 28, 8968 (2016)

Others:

9. Z. K. Liu, L. X. Yang, Y. Sun, T. Zhang, H. Peng, H. F. Yang, **C. Chen**, Y. Zhang, Y. F. Guo, D. Prabhakaran, M. Schmidt, Z. Hussain, S.-K. Mo, C. Felser, B. Yan and Y. L. Chen
"Evolution of the Fermi surface of Weyl semimetals in the transition metal pnictide family"
Nature Materials, 15, 27 (2016)

10. J. Jiang, Z. K. Liu, Y. Sun, H. F. Yang, R. Rajamathi, Y. P. Qi, L. X. Yang, **C. Chen**, H. Peng, C.-C. Hwang, S. Z. Sun, S.-K. Mo, I. Vobornik, J. Fujii, S. S. P. Parkin, C. Felser, B. H. Yan, Y. L. Chen
"Signature of type-II Weyl semimetal phase in $MoTe_2$"
Nature Communications, 8, 13973 (2017)

11. Han Peng, Niels B. M. Schröter, Jianbo Yin, Huan Wang, Ting-Fung Chung, Haifeng Yang, Sandy Ekahana, Zhongkai Liu, Juan Jiang, Lexian Yang, Teng Zhang, **Cheng**

Chen, Heng Ni, Alexey Barinov, Yong P. Chen, Zhongfan Liu, Hailin Peng, Yulin Chen
"Substrate Doping Effect and Unusually Large Angle van Hove Singularity Evolution in Twisted Bi- and Multilayer Graphene"
Advanced Materials, 29, 1606741 (2017)

12. A.J. Liang, J. Jiang, M.X. Wang, Y. Sun, N. Kumar, C. Shekhar, **C. Chen**, H. Peng, C.W. Wang, X. Xu, H.F. Yang, S.T. Cui, G.H. Hong, Y.-Y. Xia, S.-K. Mo, Q. Gao, X.J. Zhou, L.X. Yang, C. Felser, B.H. Yan, Z.K. Liu, and Y.L. Chen
"Observation of the topological surface state in the nonsymmorphic topological insulator KHgSb"
Physical Review B, 96, 165143 (2017)

13. C.W. Wang, Y.Y.Y. Xia, Z. Tian, J. Jiang, B.H. Li, S.T. Cui, H.F. Yang, A.J. Liang, X.Y. Zhan, G.H. Hong, S. Liu, **C. Chen**, M.X. Wang, L.X. Yang, Z. Liu, Q.X. Mi, G. Li, J.M. Xue, Z.K. Liu, and Y.L. Chen
"Photoemission study of the electronic structure of valence band convergent SnSe"
Physical Review B, 96, 165118 (2017)

14. Yiwei Li, Yunyouyou Xia, Sandy Adhitia Ekahana1, Nitesh Kumar, Juan Jiang, Lexian Yang, **Cheng Chen**, Chaoxing Liu, Binghai Yan, Claudia Felser, Gang Li, Zhongkai Liu, Yulin Chen
"Topological origin of the type-II Dirac fermions in PtSe2"
Physical Review Materials, 1, 074202, (2017)

15. J. Jiang, N. B. M. Schröter, S.-C. Wu, N. Kumar, C. Shekhar, H. Peng, X. Xu, **C. Chen**, H. F. Yang, C.-C. Hwang, S.-K. Mo, C. Felser, B. H. Yan, Z. K. Liu, L. X. Yang, and Y. L. Chen
"Observation of topological surface states and strong electron/hole imbalance in extreme magnetoresistance compound LaBi"
Physical Review Materials, 2, 024201 (2018)

Abbreviations

ARPES	Angle-Resolved Photoemission Spectroscopy
SOC	Spin-Orbit Coupling
BZ	Brillouin Zone
2D	Two Dimensional
STM	Scanning Tunnelling Microscopy
PES	Photoemission Spectroscopy
XPS	X-ray Photoemission Spectroscopy
UPS	Ultraviolet Photoemission Spectroscopy
EUPS	Extreme-Ultraviolet Photoemission Spectroscopy
UHV	Ultra-High Vacuum system
TOF	Time-of-Flight
DLS	Diamond Light Source
LC	Lower Chamber
UC	Upper Chamber
IC	Interface Chamber
LL	Load Lock
LEED	Low Energy Electron Diffraction
FET	Field Effect Transistor
SO	Schwarzschild objectives
TI	Topological Insulators
TSM	Topological Semimetals
TDSM	Topological Dirac Semimetals
DSM	Dirac Semimetals
WSM	Weyl Semimetals
LNSM	Line-Node Semimetals
XRD	X-ray Diffraction
BS	Bulk State
SS	Surface State

MDC	Momentum Distribution Curves
TMD	Transition Metal Dichalcogenides
SdH	Shubnikov-de Haas
CBM	Conduction Band Minimum
VBM	Valence Band Maximum
DOS	Density of State
FS	Fermi Surface
EDC	Energy Distribution Curves
STS	Scanning Tunnelling Spectroscopy
FFT	Fast Fourier Transform
Tr-ARPES	Time- Angle-Resolved Photoemission Spectroscopy
CVD	Chemical Vapour Deposition
tBLG	Twisted Bilayer Graphene
vHS	van Hove Singularities
TEM	Transmission Electron Microscopy
SAED	Selected Area Electron Diffraction
PMMA	Polymethyl Methacrylate
hBN	Hexagonal Boron Nitride

Contents

Chapter 1

Introduction to Angle-Resolved Photoemission Spectroscopy (ARPES)

The electronic structure is one of the critical properties that determines the electric, optical and magnetic properties of materials. Angle-Resolved Photoemission Spectroscopy (ARPES) is the most direct experimental technique to reveal the electronic structures of solids[1,2]. In this chapter, we will give a brief introduction to the theoretical background and the experimental setup of this modern technique.

1.1 General principle of photoemission

1.1.1 Photoemission process

The basic principle of the ARPES technique is the photoemission process, which was discovered by Hertz back in 1887. The relation between the quantization of light and the photoemission phenomenon was later explained by Einstein in 1905. In modern scientific research, photoemission has been used as a very efficient and direct way to study the properties of electrons inside matter. There are many books providing detailed explanation of the photoemission process, while here we will only give a brief introduction to the part which is essential for understanding ARPES technique. The main reference of this chapter is the book written by S. Hüfner[3].

Photoemission describes a process in which the electron inside materials (solid, liquid, gas) can absorb an incident photon with an energy larger than the material's work function, and escape. According to the energy conservation law, the process is described by the following equation:

$$E_k = h\nu - \phi - |E_b|$$

where E_k is the kinetic energy of the photoelectron, $h\nu$ is photon energy, ϕ is material's work function, and E_b is the binding energy of the electron inside materials. Figure 1.1 illustrated the energy level diagram inside the material and the energy distribution of the emitted photoelectrons related. Electrons from both the bands near the Fermi level (E_f) and core levels will be emitted, if provided with enough energy. The energy distribution of the emitted electrons often gives a replica of the electron energy distribution in the solid, which is an attractive feature of PES[3]. The reference points inside the material and in the vacuum are taken to be E_f and E_{vac} (energy of vacuum), respectively.

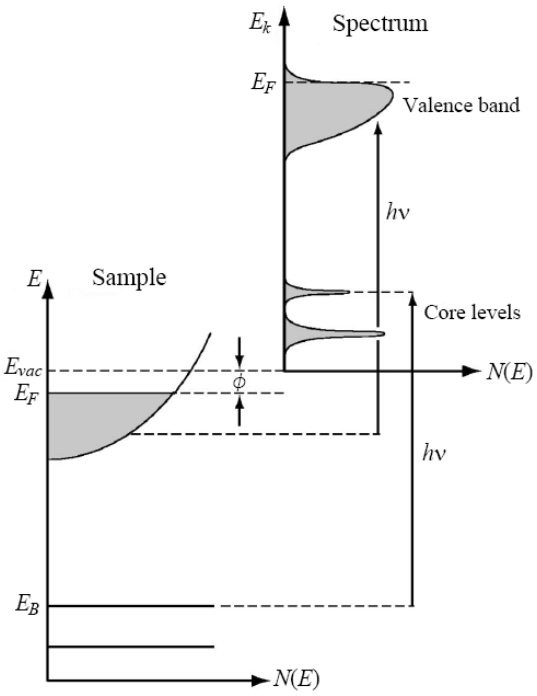

Fig. 1.1 Energetics of the photoemission process. The relation between the energy levels in the materials and the energy distribution of the excited photoelectrons. Adapted from Ref. 3.

To understand what happens during a photoemission process as well as to find the correct model for computing, different approaches have been brought up. A well-known explanation is the very successful three-step model (Fig. 1.2), which breaks up the whole process into three steps:

(1) In the first step, an electron inside solid is excited from initial state to excited state by an incident photon.

(2) Subsequently, the excited electron travels to the sample surface. The transport coefficient is related to the inelastic mean free path of the excited electron in solid, which can be depicted by the "Universal Curve" (Fig. 1.4).

(3) Finally, the electron escapes from the sample surface into the vacuum. Only the electron with energy larger than material's work function can overcome the

surface barrier. Considering the existence of the vertical electric field, related to the work function, only the momentum parallel to the surface remains conserved.

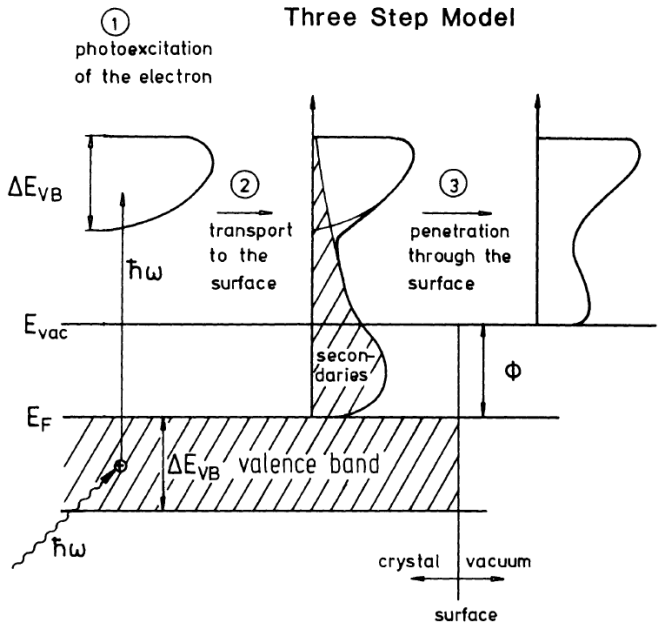

Fig. 1.2 Three-step model. (1) Photoexcitation of electrons. The electron from either the valence band or core level absorbs incident photon, being excited from initial state to an excited state. (2) The excited photoelectron travels to the surface, while losing energy and concomitant producing secondaries electrons (shaded). (3) The excited electron overcomes the surface barrier and penetrate the solid surface, escaping into the vacuum. Adapted from Ref. 3.

During the process, the momentum of the incident photon is typically orders of magnitude smaller than the excited electron; therefore their contribution can be safely neglected[1]. In the third step only the momentum parallel to sample surface is conserved, which is natural since that the translation symmetry along the perpendicular direction is broken by the boundary of solid surface and vacuum. As a consequence, the momentum relation in the photoemission process can be described as following:

$$\hbar k_{\parallel} = \sqrt{2m \cdot E_{kin}} \cdot \sin\Theta$$

$$\hbar k_{\perp} = \sqrt{2m \cdot [E_{kin} \cdot (\cos\Theta)^2 + V_0]}$$

where E_{kin} is the kinetic energy of the emitted photoelectron, $k_{\parallel}$ is the parallel momentum of the photoelectron before photoemission and Θ is the polar emission angle according to direction perpendicular to sample surface (the detailed measurement geometry will be discussed in section 1.2.1). To deal with the perpendicular momentum $k_{\perp}$which is not conserved during the process, a material dependent parameter V_0 is introduced, which is the so-called inner potential. Practically, in an ARPES measurement, the value of V_0 can be determined by comparing the periodicity of the measured band structure along the $k_{\perp}$ direction to the periodicity of Brillouin Zone (BZ) deduced from crystal lattice parameters (an example of detailed data analysis will be illustrated in section 2.2.4).

1.1.2 Signal strength of Photoemission Spectroscopy (PES)

From the above discussion, we can see that by measuring the energy and momentum information of the emitted photoelectrons, the initial electron's states inside the material can be deduced. Assuming the material system contains N electrons, the signal strength of the general photoemission spectroscopy (PES) measurement (or photoemission current *I*) can be described by following expression:

$$I \propto \left|\langle \Psi_{f,N} | H_{int} | \Psi_{i,N} \rangle\right|^2 \delta(E_f - E_i - \hbar\omega) F(T)$$

where $\left|\langle \Psi_{f,N} | H_{int} | \Psi_{i,N} \rangle\right|^2$ is the transition matrix element between the initial electron states $|\Psi_{i,N}\rangle$ of the system and the final electron states $|\Psi_{f,N}\rangle$ after the photoemission process. $H_{int} = \vec{A} \cdot \vec{P}$ represents the photon electric field in the photoemission process.

$\delta(E_f - E_i - \hbar w)$ describes the energy conservation during the process, while *F(T)* is the Fermi-Dirac distribution.

As the number of electrons inside a real material system is huge, it is impossible to directly calculate the matrix element. Therefore, to study the system, approximations are needed to simplify the equations. We start with the simplest approximation that a one-electron wave function can be used to describe the emitted electron while the other N-1 electrons are treated separately. As a consequence, we can describe the initial and final states in following equations:

$$|\Psi_{i,N}\rangle = |\phi_{i,k}\rangle \cdot |\Psi^k_{i,(N-1)}\rangle$$

$$|\Psi_{f,N}\rangle = |\phi_{f,E_k}\rangle \cdot |\Psi^k_{f,(N-1)}\rangle$$

Subsequently, another approximation, the sudden approximation, can be applied, which assumes that the system does not relax after the escape of the photoelectron. In simple words, other electrons cannot "feel" the whole process of photoemission. Therefore, the final N-1 states are identical to the initial states:

$$|\Psi^k_{i,(N-1)}\rangle = |\Psi^k_{f,(N-1)}\rangle$$

As a result, the matrix element can be rewritten as:

$$\langle\Psi_{f,N}|H_{int}|\Psi_{i,N}\rangle = \langle\phi_{f,E_k}|H_{int}|\phi_{i,k}\rangle\langle\Psi^k_{f,(N-1)}|\Psi^k_{i,(N-1)}\rangle = \langle\phi_{f,E_k}|H_{int}|\phi_{i,k}\rangle$$

For most of the weakly interacting systems, this single particle picture (the sudden approximation) discussed above can be applied well. The photoemission current can be expressed as:

$$I \propto \left|\langle\phi_{f,E_k}|H_{int}|\phi_{i,k}\rangle\right|^2 \delta(E_f - E_i - \hbar w)F(T)$$

The measured ARPES experimental spectra will be given in the form of delta functions as illustrated in Fig. 1.3(a).

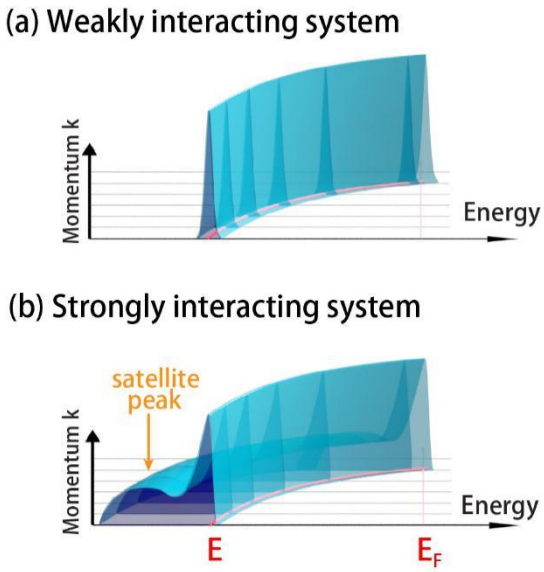

Fig. 1.3 Spectra of ARPES measurement. (a) Momentum resolved ARPES spectra from weakly interacting electron systems. (b) Momentum resolved ARPES spectra from strongly interacting system.

On the other hand, the situation is more complicated for the material systems with strong electron-electron interaction. The assumption that $|\Psi^k_{i,(N-1)}\rangle = |\Psi^k_{f,(N-1)}\rangle$ can no longer be applied, since the final N-1 electron system will readjust its charge distribution to minimize the energy of the system. Accordingly, let's assume that if the final system has S excited eigenstates $|\Psi^k_{f,S(N-1)}\rangle$, with energy $E_{S(N-1)}$, the photoemission current can be expressed as:

$$I \propto \sum_{f,i,k} \left|\langle \phi_{f,E_k}|H_{int}|\phi_{i,k}\rangle\right|^2 \sum_s \langle \Psi^k_{f,S(N-1)}|\Psi^k_{i,S(N-1)}\rangle\, \delta\left(E_{f,E_k} + E_{S(N-1)} - E_i - \hbar w\right) F(T)$$

Though the equation here seems more complicated, it contains more valuable information for the electron-electron interaction in a strongly interacting system (e.g. high temperature superconductors…). The measured ARPES spectra will also become more complicated as the delta function will be accompanied by satellite peaks (Fig. 1.3(b)).

It is important to point out here that, as the studies on topological quantum materials and functional materials discussed in the following chapters are all weakly interacting systems. Therefore, we can safely assume that the ARPES spectra represent the real band structures of these materials.

1.1.3 Surface-sensitive technique

A critical point for PES measurement is that it is a surface technique. A typical PES experiment uses an incident photon beam with photon energy of 10~2000 eV. As a result, the escape depth or mean free path of photoelectrons is around few Å, which is only several atomic layers deep in the material. This means PES is a very surface-sensitive technique, which requires an ultra-high vacuum system and *in situ* cleavage of the sample to maintain the cleanness of sample surface. The escape depth of the photoelectron can be best illustrated by the 'universal curve' (Fig. 1.4).

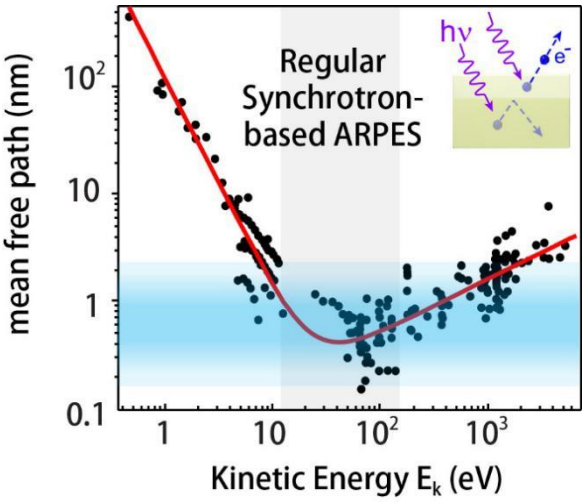

Fig. 1.4 The 'Universal curve' for surface sensitivity in photoemission process. The values of mean free path in various materials are plotted versus their kinetic energy in solids. For regular synchrotron-based ARPES measurement, mean free path range from 0.1 to few nanometers. Reproduced from Ref. 3.

1.1.4 Different photon energy

So far, we have briefly introduced the general principle of photoemission process. Based on that, PES has been used as the most direct way to study the electron states in solids since 1950s. According to the different energy of incident photon, PESs can be classified into X-ray photoemission spectroscopy (XPS), ultraviolet photoemission spectroscopy (UPS), extreme-ultraviolet photoemission spectroscopy (EUPS), etc.

In our ARPES measurement, we generally use a relatively low incident photon energy of 10~200 eV. The lower energy gives better momentum resolution, since the photon energy is inversely proportional to the momentum resolution. As mentioned above, for this energy range, the signal mainly comes from the most top several layers, especially from the surface. Therefore, surface states of the materials can be clearly distinguished. On the contrary, the

use of a higher photon energy (e.g. 1000 eV) will gives us more information from the bulk states.

Practically, in recent studies on topological quantum materials[4,5] (e.g. topological insulators, topological semimetals, new fermions…), most researchers focus on the band structure from both surface and bulk states. Therefore, a combining usage of ARPES system with both ultra-violate photon beam (10-100 eV) and a soft X-ray photon beam (100-1000 eV) often provide more comprehensive observation of the full electronic structure of materials.

1.2 Concept of ARPES experiment

1.2.1 Measuring geometry

Based on the discussed basic principle of the photoemission process, ARPES measurements pick up the photoelectron with a certain angle according to the sample surface and detects its energy and momentum (Fig. 1.5(a)). By rotating the analyzer, we can systematically accumulate the information of photoelectrons with different emitted angles, and then reconstruct the band structure of electrons inside materials.

In a real experiment, as illustrated in Fig. 1.5(b), the hemispherical analyzer often has an entrance slit to detect electrons with different emitted angle ϕ. As a consequence, after resolving the energy distribution of electrons within the analyzer, we actually obtain a 2D cut of spectra $I(k, E)$ for each measurement. Next, the analyzer is rotated along the other angle θ (practically, the sample stage is rotated instead of the analyzer in standard ARPES,

while the analyzer is rotated in spatially resolved ARPES system. Details will be discussed at the end of the chapter). 2D cuts taken from different angle Θ are then combined into a 3D spectra $I(k_x, k_y, E)$.

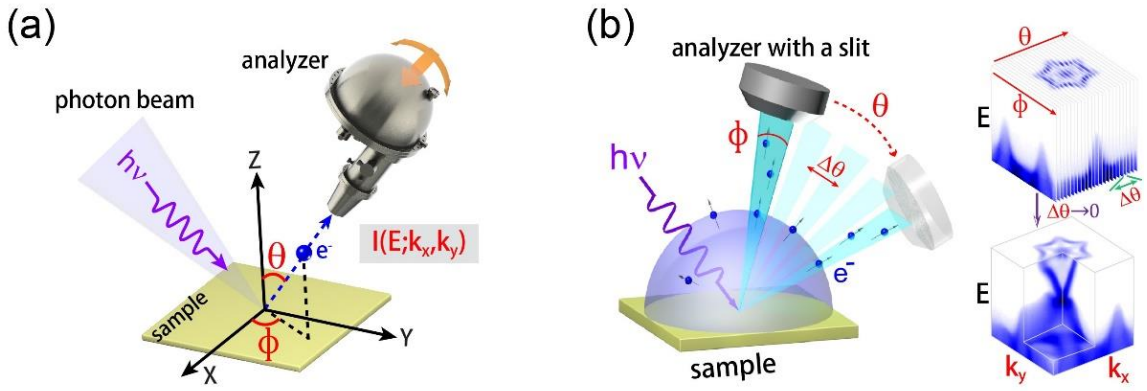

Fig. 1.5 Principle of ARPES measurement. (a) Illustration of an ARPES measurement with photoelectrons' emission angles Θ and ϕ indicated. (b) Schematic of data accumulating. 2D dispersion cuts obtained from different angle Θ can be combined and reconstructed into 3D band structure.

1.2.2 Examples of key parameters obtained

The electronic structure is very important in determining the electrical, magnetic and optical properties of materials. Therefore, many key parameters can be directly obtained from an ARPES measurement. In the following, we will demonstrate some of the parameters obtained by using the example of a 2D free electron system (Fig. 1.6)[6,7].

(1) Fermi surfaces (FSs) and carrier density (n):

In the 2D free electron system, the electronic band structure has a parabolic shape as illustrated in Fig. 1.6(b). By performing an ARPES experiment, 3D spectra of band

structure, shown in Fig. 1.6(c), will be obtained. The FS map, which is a circle here (Fig. 1.6(c)(iii)), can be directly acquired by taking the constant energy contour $I(k_x, k_y)$ at $E = E_F$. The FS area A can also be calculated, which gives the 2D carrier density as $n = A/2\pi$.

(2) Band dispersions, effective mass (m^*) and Fermi-velocity (V_{E_F}):

In the same way, the band dispersion can be directly acquired by taking the constant momentum slice $I(k, E)$ out of the 3D spectra, as illustrated in Fig. 1.6(c)(ii). The dispersion of 2D free electron system has a parabolic shape, which can be fitted by $\frac{\hbar^2 k^2}{2m^{*2}}$, where m^* is the effective mass. The Fermi-velocity can also be deduced as $V_{E_F} = \frac{1}{\hbar}\frac{dE}{dk}|_{k=k_F}$.

(3) Band gap (Δ) and band width:

The band gap of the materials (e.g. topological insulator, semiconductor…) can be directly obtained as the difference between the conduction band minimum and valance band maximum in the measured ARPES spectra. The width of the band is the difference between the maximum and minimum of a certain band, which can also be directly obtained from measured band dispersion.

(4) Carrier life (τ) and mean free path (λ):

The limited life-time and mean free path of the carriers leads to an intrinsic broadening of the measured ARPES spectra. Therefore, if the influence of the instrumental resolution is excluded, they can be estimated by $\lambda = \hbar/\delta k$ and $\tau = \hbar/\delta E$, as shown in Fig. 1.6(c).

With these key parameters, most physical properties of the materials can be estimated, e.g. electrical conductivity $\sigma = \frac{ne^2\tau}{m^*}$, Hall coefficient $R_H = -\frac{1}{ne}$, carrier mobility $u = \frac{\sigma}{ne}$,

Seebeck coefficient ($\frac{8\pi^2 k_B^2 T}{3eh^2} m_d^* (\frac{\pi}{3n})^{2/3}$) etc. Besides, there is also other important information that can be extracted from the measured ARPES spectra, such as superconductivity gap, electron-electron interaction, electron-phonon interaction…[8,9] In addition, if the sample is measured at different temperatures, with different strain, or even under gating geometry, many phase transitions related to these origins can be investigated.

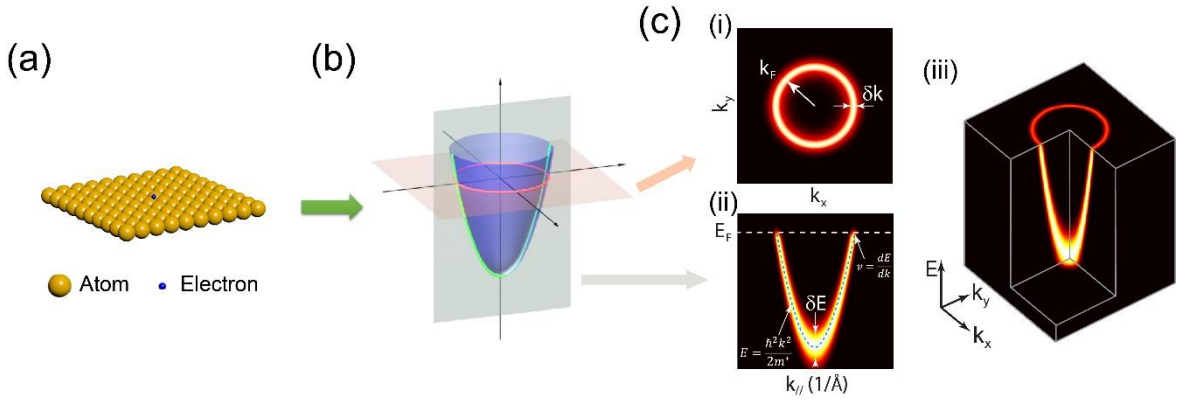

Fig. 1.6 2D free electron system and its band structure. (a) Illustration of a 2D free electron system. (b) Illustration of the related parabolic band structure. (c) Simulated ARPES data of the 2D free electron system. Courtesy to Yulin Chen.

1.2.3 Experimental setup

In general, the ARPES system contains the following main parts, as illustrated in Fig. 1.7:

(1) **Ultra-high vacuum system (UHV)**. As mentioned above, ARPES is a very air-sensitive technique that only probes the electronic structure of the most top few atom layers of the materials. Therefore, a UHV system is required to keep the cleaved surface clean during the entire measurement. In order to perform successful experiments (typically for at least several hours), the vacuum level should be kept

better than 10^{-10} mbar. Various pumping systems are required, including the rough pumping stage (e.g. scroll pumps, rotary pumps), the intermediate stage (e.g. turbo molecular pumps), the UHV stage (e.g. ion pumps or cryogenic pumps).

(2) Light source. In ARPES, the light source provides incident photons with energy higher than the work function of materials, in order to excite the photoelectrons. Currently, synchrotron radiation is considered to be the most versatile and widely used light source for ARPES systems, since it can provide incident photon beam with tunable polarization and a very broad energy range[1,10-12] (will be discussed in following section). For lab-based ARPES, gas-discharge lamps (e.g. halogen lamp) are usually equipped, with different photon energies available by selecting different selections of the working gas[13]. Besides, the vacuum ultra-violet (VUV) laser has also recently become a very good choice as light source[14-16], considering its extreme high flux, and extraordinary energy and temporal resolutions.

(3) Sample manipulation and temperature control system. As mentioned above, in order to gain the information of photoelectrons with different emitting angles, the analyzer needs to be rotated. Practically, instead of rotating the analyzer, which is relatively more difficult, a sample manipulator is usually equipped to rotate the sample with respect to the analyzer. Furthermore, to minimize the temperature broadening of the measured ARPES spectra as well as to study the temperature phase transitions in the material systems, a temperature control system is also integrated into the sample manipulator.

(4) Electron analyzer. Electron analyzer is used to measure the momentum and energy of the excited photoelectrons. Currently, the most widely used analyzer is the hemispherical deflection analyzer, which produces a 2D image of band dispersion $I(E,k_x)$ in one measurement[17]. Besides, there are also other types of analyzer with

different principles. For example, the time-of-flight (TOF) analyzer is often equipped in the time-resolved ARPES system, which measures the full 3D band dispersion in one measurement $I(E,k_x,k_y)$[18-20].

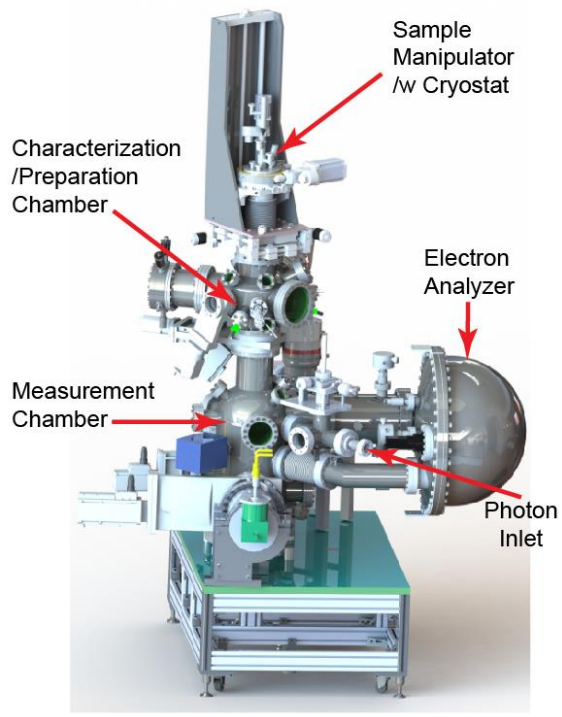

Fig. 1.7 Illustration of real ARPES system. The system usually consists of ultra-high vacuum (UHV) system, sample manipulating and temperature controlling system and light source.

1.3 Synchrotron based ARPES system

1.3.1 Synchrotron light source

A synchrotron is an extremely powerful source of X-ray radiation, which provides researchers with continually tunable photon beam in a very broad energy range[1,2,11,12]. The

basic principle is very simple that electrons will emit light if their moving directions are changed. In the 1960's, scientists started to think about using synchrotron light as a light source for scientific research. First generation of synchrotron facility was built directly from the prototype of collider, which was originally used for high-energy particle physics. Then, second generation of synchrotron facility was built dedicatedly to provide synchrotron light, by using bending magnets. In third generation synchrotron facility (most widely used at the moment), insertion device was used to create more intense and tunable radiation. The next generation of synchrotron facility are the sources with highly coherent beam[21]. There are in total around 70 synchrotron facilities worldwide, providing extraordinary research platforms for modern scientific research. A typical third generation synchrotron facility, Diamond Light Source (DLS) in UK, is illustrated in Fig. 1.8.

Fig. 1.8 Diamond Light Source (DLS), Harwell campus, UK. DLS is the national synchrotron facility of United Kingdom. It produces intense beams of light used in many areas of scientific research. Adapted from Ref. 22.

Synchrotron generate light 10 billion times brighter than the light of the sun. Here, we take DLS as an example, to demonstrate its working mechanism[22]. As shown in Fig. 1.9, electrons are firstly generated by the electron gun and accelerated to very high speeds by linear accelerator (Linac) and the booster synchrotron. The accelerated electrons are then injected into the **Storage Ring,** where they travel at nearly the speed of light for several hours. The trajectories of the electrons inside storage ring are controlled by the synchronized magnetic field exerted by bending magnets. When the electrons' travelling directions are steered by these powerful magnets, they lose energy in the form of light, and generate x-ray radiation. In addition, as a feature of third generation synchrotron facility, **Undulators** (Insertion Devices)[23], which consist of special arrays of small magnets (Fig. 1.9(b)), are also used to generate radiation. Electrons travelling through the Undulators are forced to follow an undulating trajectories, while the light emitted at each bend overlaps and interferes with others to form even brighter and more focused radiation beam. The wavelength of the radiation generated can be easily tuned by changing the gap size of the small magnets.

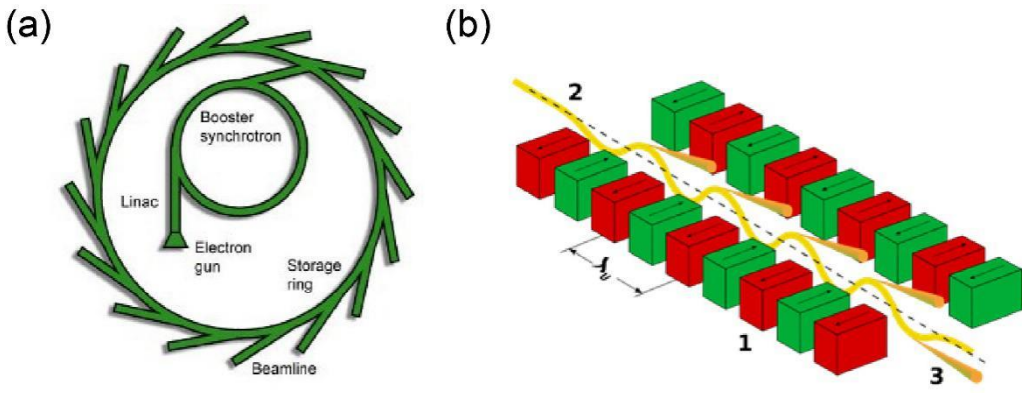

Fig. 1.9 Sketch of DLS and Insertion device. (a) Schematic of sychrotron system in DLS, including electron gun, linear accelerator (Linac), booster synchrotron, storage ring and beamlines. (b) Schematic of the insertion device (Undulator). Electrons are forced to wiggle by the arrays of magnets and generate strong synchronized X-ray radiation. Adapted from Ref. 22.

The radiation generated by either bending magnet or insertion devices are directed into different experimental stations, which are the so-called **Beamlines**. Beamlines are constructed according to different scientific purposes and research field, including physics, chemistry, biology…. For example, as illustrated in Fig. 1.10, there are more than 30 beamlines surrounding the storage ring in Diamond Light Source[24]. The starting letter 'B' indicates that the beamline uses bending magnet, while the letter 'I' means the usage of insertion devices.

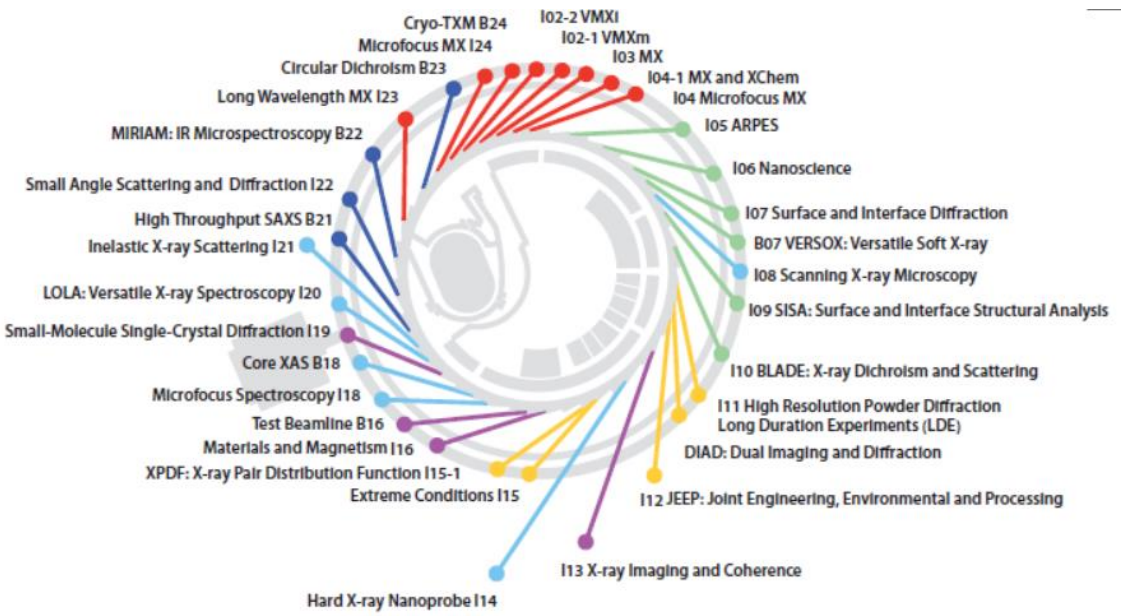

Fig. 1.10 Beamlines at DLS. More than 30 beamlines have been constructed at DLS. They are used for different scientific purpose ranging from spectroscopy, diffraction, scattering... Image adapted from Ref. 24.

The strong x-ray radiation with tunable photon energy generated by synchrotron radiation serves as an extraordinary light source for APRES experiments. Many ARPES beamlines have been constructed worldwide. For most of the data discussed in following

chapters, related ARPES experiments were carried out at I05 beamline of Diamond Light Source (UK) and at the Spectromicroscopy beamline of the Elettra synchrotron (Italy). Therefore, in the following, we would like to give a brief introduction to the equipment setups on these two beamlines.

1.3.2 Beamline I05 at Diamond Light Source

I05 is a specially designed soft X-ray beamline at DLS for surface science research[11]. The optical system provides the photon beam with an energy range of 18-240 eV. As illustrated in Fig. 1.11, a 5-m-long APPLE-II undulator generates X-ray radiation with either linear (horizontal/vertical) or circular (left/right) polarization. The generated beam then passes through the monochromator and cylindrical focusing optical systems, before being directed to the experimental end stations. The beamline is separated into two different branches, both using the ARPES technique.

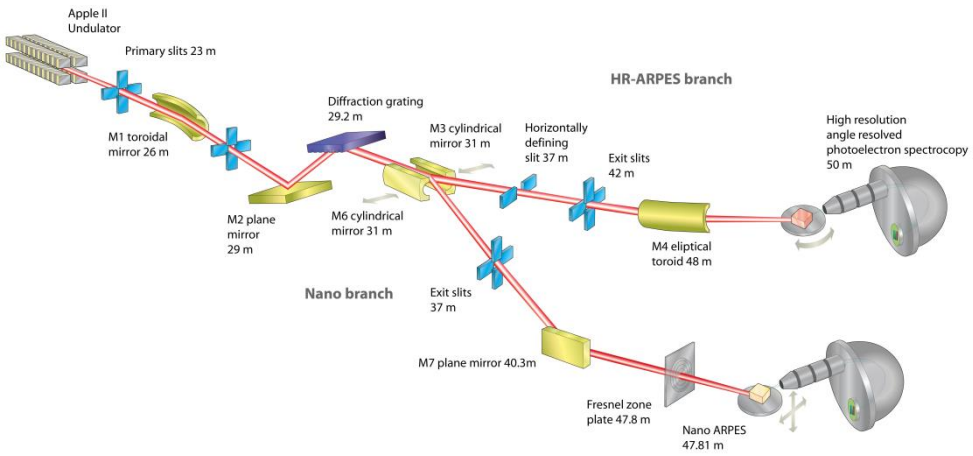

Fig. 1.11 Sketch of optical system of Beamline I05. Two end stations (HR-ARPES and Nano-ARPES) are installed at the beamline. They share the APPLE II undulator as well as the optical devices up to the plane grating monochromator. Adapted from Ref. 11.

The high resolution branch (HR-ARPES) is equipped with a high resolution ARPES system, while the Nano-ARPES branch is equipped with a spatially resolved ARPES system. The HR-ARPES has been open to users since summer of 2013, and witnessed many important breakthroughs in quantum materials research field including the discoveries of topological Dirac semimetals, Weyl semimetals… All the high resolution ARPES data shown in the following chapter (Chapter 2&3) come from this branch. Therefore, here we will only introduce the experimental setup at HR-ARPES branch.

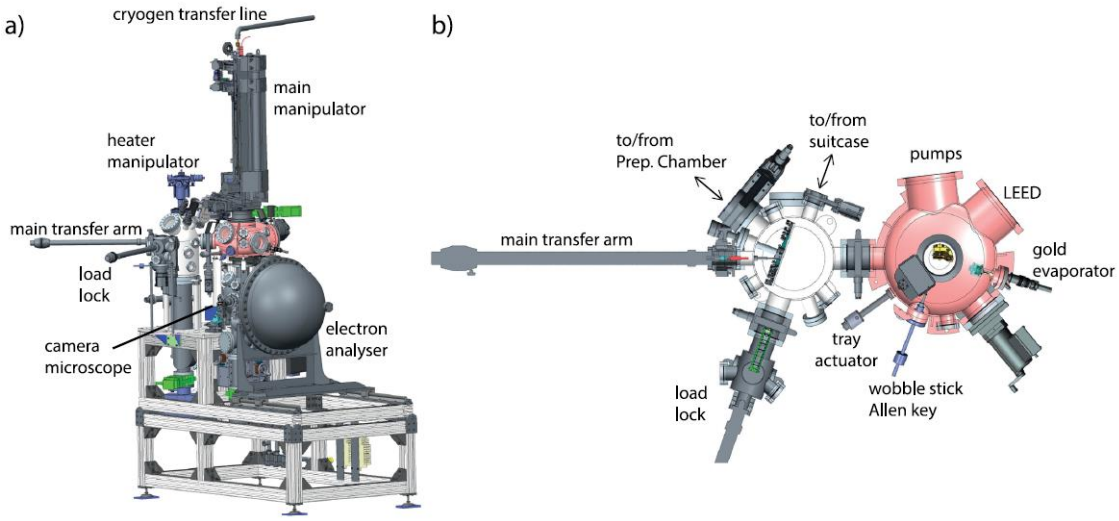

Fig. 1.12 HR-ARPES end station. The vacuum system consists of Lower Chamber (LC), Upper chamber (UC), Interface Chamber (IC) and Load Lock (LL). Transfer arms are used to move the sample within the LL, IC and UC, while the main manipulator is used to perform APRES measurements in LC. A gold evaporator, as well as Low Energy Electron Diffraction (LEED), is also installed in the UHV system. Adapted from Ref. 11.

The sketch of the end station is illustrated in Fig. 1.12. The UHV system consists of three UHV chambers with a fast entry Load Lock (LL). Up to 10 samples can be inserted

into the LL at one time, which are then transferred to the Interface Chamber (IC) after 3-5 hours of pumping. When the vacuum in the IC recovers to ~$5*10^{-9}$ mbar, the sample can be inserted into the cryogenic main manipulator, which travels between the Upper Chamber (UC, for potassium dosing and Low Energy Electron Diffraction (LEED) measurement) and the Lower Chamber (LC, for ARPES measurement). The vacuum in these two chambers is often kept below $2*10^{-10}$ mbar, providing a decent UHV environment for APRES measurements.

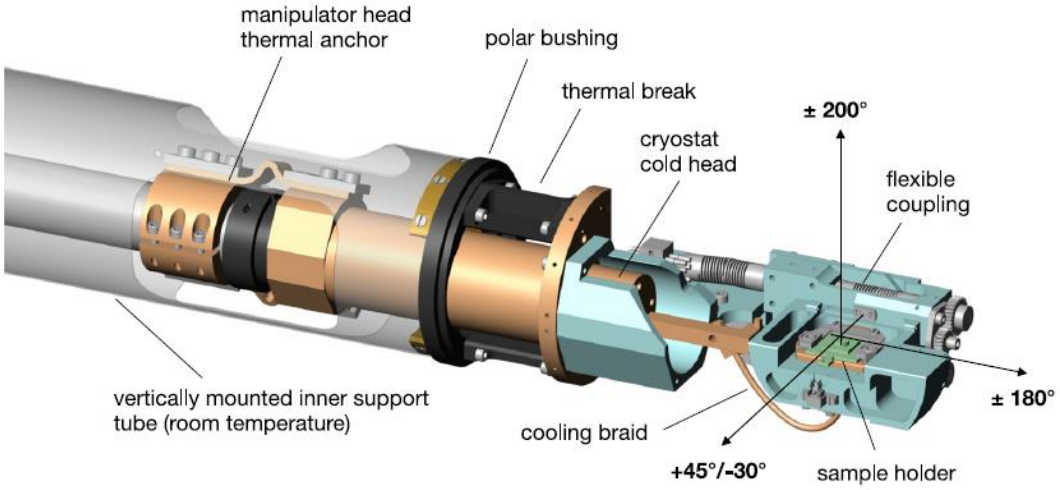

Fig. 1.13 Illustration of the manipulator head. The three rotational axes (polar, tilt, azimuth) with their respective angular ranges are indicated. During the measurement, the head of manipulator is shielded within gold coated copper foil (not shown here) to maintain the low temperature and minimize the distortion of the electrostatic field between surface of sample and analyser entrance lens. Adapted from Ref. 11.

The ARPES system is equipped with a hemispherical electron analyzer (model R4000, VG Scienta), providing great energy and momentum resolution for ARPES measurement. As the analyzer is fixed on the LC, during the measurement, sample needs to be rotated to

access different angles. Therefore, illustrated in Fig. 1.13, a cryogenic sample manipulator, having 6 degrees of freedom, is installed on the system, providing excellent control to the sample. The sample can be easily rotated around the three axes (polar, tilt, azimuth) according to the requirement of ARPES measurement. Specially designed shielding has recently been added to the cryogenic system, which will keep the temperature of the sample below 5 K when using liquid helium.

In summary, the HR-ARPES end station at beamline I05 of DLS provides us with a great platform to carry out ARPES experiment on various samples. I had the opportunity to perform more than 20 beamtimes at this beamline during my entire DPhil study. I really enjoy the excellent performance, high automatic level of the equipment and do appreciate the great help from beamline scientists.

1.3.3 Beamline Spectromicroscopy at Elettra synchrotron

Similar to DLS, Elettra synchrotron, located in Trieste (Italy), is a third generation synchrotron light source. The facility was constructed in 1993 and upgraded in 2009. At the moment, there are in total 25 beamlines surrounding the storage ring (shown in Fig. 1.14)[25], providing great platforms for many research techniques such as spectroscopy, diffraction, scattering, etc.

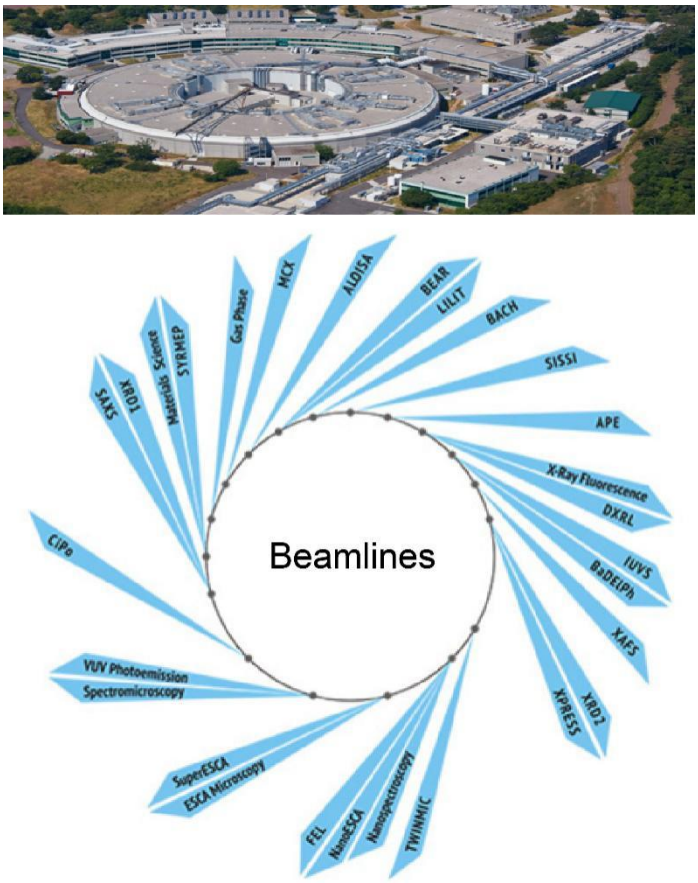

Fig. 1.14 Elettra synchrotron, Trieste, Italy. There are in total 25 beamlines constructed around the storage ring for different scientific research fields. Adapted from Ref. 25.

The spectromicroscopy beamline (BL 3.2L)[26] is specially designed for one of the next generation ARPES: spatially resolved ARPES. This new technique features the ability to focus the incident photon beam into submicron region. Therefore, the electronic structure at different positions of the sample can be accurately probed. This is extremely useful for the studies on spatially limited sample systems, such as cleaved single crystals with multi-domains, exfoliated 2D materials with small geometrical sizes, nanoscale electronic devices with gating geometry (e.g. Field Effect Transistor (FET)) etc. A detailed introduction to the development of this new technique, as well as the recent studies, will be discussed in Chapter 4. In the following context, we will only give a brief introduction to the experimental setup at this beamline.

To achieve spatial resolution in an ARPES experiment is actually more difficult than it sounds to be. In a high resolution ARPES system, e.g. the aforementioned HR-ARPES branch at I05, the electron analyzer is often fixed onto the UHV chamber, while the sample is rotated to gain access to different angles. However, this leads to the shifting of the beam spot position on the sample during the measurement. Therefore, to achieve a spatially resolution down to submicron region, sample stage must be fixed according to the direction of incident beam, while we can only rotate analyzer to access different angles.

The optical system of the Spectromicroscopy beamline[26] is illustrated in Fig. 1.15. X-ray radiation is firstly generated by a U12.5 undulator (not shown here) inserted in the storage ring. Focusing optics, monochromator, and refocusing optics are then used to select the radiation with desired photon energy, ranging from 20 to 310 eV. After passing the pinhole (P), the incident beam is further focused by the Schwarzschild objectives (SO) onto the sample stage (SS) with a spot size less than 1 micron (smallest spot achievable is ~0.5 μm FWHM). The SO consists of two spherical mirrors with high reflectivity, obtained by using periodic multilayer coating technique. There are two sets of SO devices available on the beamline, which operate at photon energies of 27 eV and 74 eV respectively.

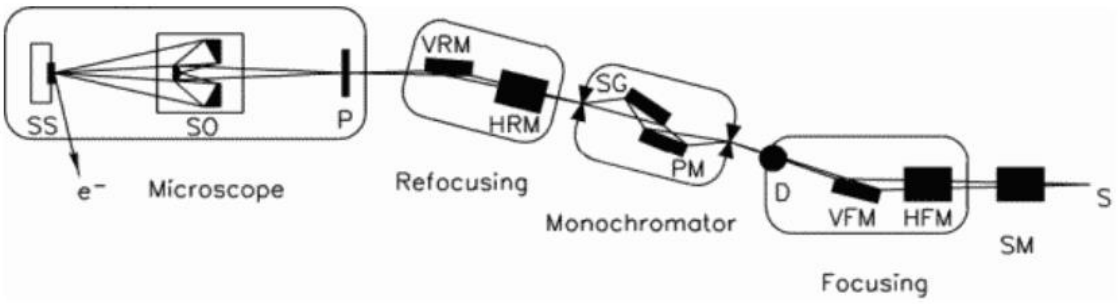

Fig. 1.15 Sketch of optical system of Beamline Spectromicroscopy. The beamline consists of the undulator (not shown), focusing optical, Monochromator, refocusing optical and microscope end station. SS: Sample Stage. SO: Schwarzschild Objectives. P: Pinhole. Adapted from Ref. 26.

Figure 1.16 shows a sketch of the spatially resolved ARPES end station[27]. The sample stage, attached with cooling stage and heater, is fixed according to the direction of incident beam. The x and z motors of the stage enable the scanning of the sample surface during measurement to find the desired sample position, while y motor is used to adjust the focusing position. A small hemispherical electron analyzer on a goniometer with two angular degrees of freedom is installed in the UHV main chamber for ARPES measurement. The small size of the analyzer makes it possible to rotate easily, however, sacrifices the energy resolution. The best energy resolution achievable is around 24 meV when using 27 eV photon beam and liquid helium.

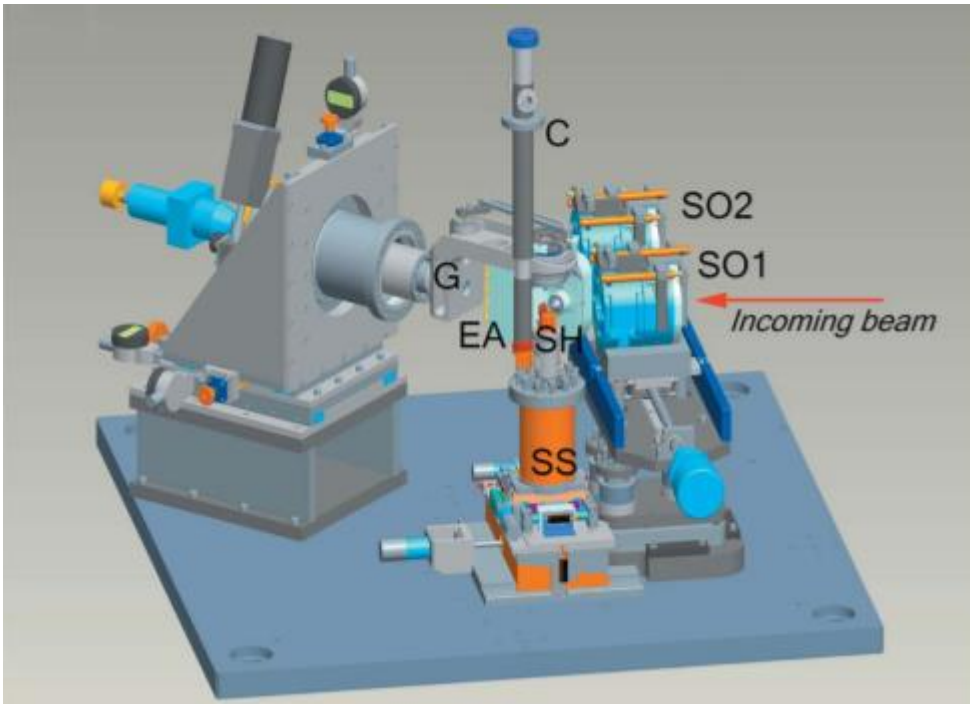

Fig. 1.16 Spatially resolved ARPES end station. The entire system is integrated within the main chamber with ultra-high vacuum. Schwarzschild objectives (SO) are used to focus the incident photon beam. Sample stage (SS) is fixed according to the direction of beam during the experiment, while the analyzer is rotated to accumulate photoelectrons with different emitting angles. Adapted from Ref. 27.

Serving as a pioneer in spatially resolved ARPES, the Spectromicroscopy beamline provides us with a well-designed system to study various material systems with limited geometrical size. All the spatially resolved ARPES data discussed in Chapter 4 was obtained from this beamline. During my DPhil study, I had the opportunity to perform over 10 beamtimes on this beamline.

Before closing the chapter, I would like to discuss more about the fundamental difference between the standard ARPES and spatially resolved ARPES. As mentioned above, the spatially resolved ARPES is designed specifically for the samples with limited geometrical sizes. To achieve that is never an easy task. To begin with, in standard ARPES, the small sample stage is always rotated to gain access to different angles, while leaving the analyzer fixed. However, in the spatially resolved system, rotating of the sample will result in losing the focus of the incident beam. The solution is either using a smaller analyzer which can be rotated inside the main chamber (as used in Spectromicroscopy) or rotate the whole UHV chamber equipped with standard analyzer (as used in Nano-brunch in I05 Diamond). In the former case, both the energy and momentum resolution will be sacrificed due to the limited size of the analyzer. While in the latter one, more complex mechanical designing and operation of the system are required.

Furthermore, the focusing of the incident beam is also not easy. We can either use a SO as discussed above or the zone plate[28] (used in Nano-brunch in I05 Diamond). SO has very good ability to focus the incident X-ray beam without losing much intensity, however, can only be used for a certain photon energy. As a result, the k_z direction of the sample's BZ cannot be accessed by using the traditional way of changing incident photon energy. In contrast, zone plate is suitable for different photon energy. However, since it uses the diffraction instead of refraction or reflection, the intensity of the beam will be significantly reduced.

There are also many other difficulties in the development of spatially resolved ARPES (e.g. consistency between beam focus and analyzer focus…), which are not discussed in details here. Considering that the systems have just been in operation for only few years, the technique is still at a very early stage of development. However, the technique is attracting more and more interest in the scientific research, and we believe it will be in high demand in the future.

References

1 Damascelli, A., Hussain, Z. & Shen, Z. X. Angle-resolved photoemission studies of the cuprate superconductors. *Rev. Mod. Phys.* **75**, 473-541 (2003)

2 Lu, D. *et al.* Angle-Resolved Photoemission Studies of Quantum Materials. *Annu. Rev. Conden. Ma. P.* **3**, 129-167 (2003).

3 Hufner, S. Photoelectron Spectroscopy: Principles and Applications. *Berlin: Springer* (1996).

4 Xu, S. Y. *et al.* Discovery of a Weyl fermion semimetal and topological Fermi arcs. *Science* **349**, 613-617, (2015).

5 Lv, B. Q. *et al.* Observation of three-component fermions in the topological semimetal molybdenum phosphide. *Nature* **546**, 627, (2017).

6 Tusche, C., Krasyuk, A. & Kirschner, J. Spin resolved bandstructure imaging with a high resolution momentum microscope. *Ultramicroscopy* **159**, 520-529, (2015).

7 Ryu, H. *et al.* Photon energy dependent circular dichroism in angle-resolved photoemission from Au(111) surface states. *Phys. Rev. B* **95** (11), 115144,(2017).

8 Richard, P., Qian, T. & Ding, H. ARPES measurements of the superconducting gap of Fe-based superconductors and their implications to the pairing mechanism. *J. Phys. Condens. Matter* **27**, 293203,(2015).

9 Hashimoto, M., Vishik, I. M., He, R. H., Devereaux, T. P. & Shen, Z. X. Energy gaps in high-transition-temperature cuprate superconductors. *Nat. Phys.* **10**, 483-495, (2014).

10 Elder, F., Gurewitsch, A., Langmuir, R. & Pollock, H. Radiation from Electrons in a Synchrotron. *Phys. Rev. 71, 829 (1947)*.

11 Hoesch, M. *et al.* A facility for the analysis of the electronic structures of solids and their surfaces by synchrotron radiation photoelectron spectroscopy. *Rev. Sci. Instrum.* **88**, (2017).

12 Borisenko, S. V. *et al.* Angle-resolved Photoemission Spectroscopy At Ultra-low Temperatures. *JoVE*, 68 (2012).

13 Nicholson, A. J. A gas discharge lamp for the extreme ultraviolet. *Appl. Opt.* , 1155-1158, (1970).

14 Koralek, J. D. *et al.* Experimental setup for low-energy laser-based angle resolved photoemission spectroscopy. *Rev. Sci. Instrum.* **78**, 053905, (2007).

15 Kiss, T. *et al.* A versatile system for ultrahigh resolution, low temperature, and polarization dependent Laser-angle-resolved photoemission spectroscopy. *Rev. Sci. Instrum.* **79**, 023106 (2008).

16 He, Y. *et al.* Invited Article: High resolution angle resolved photoemission with tabletop 11 eV laser. *Rev. Sci. Instrum.* **87**, 011301 (2016).

17 Chen, Y. Studies on the electronic structures of three-dimensional topological insulators by angle resolved photoemission spectroscopy. *Front. Phys.* **7**, 175-192, (2012).

18 Zhang, Y. *et al.* Electronic evidence of temperature-induced Lifshitz transition and topological nature in $ZrTe_5$. *Nat. Commun.* **8**, 15512 (2017).

19 Wang, Y. H. *et al.* Observation of a Warped Helical Spin Texture in Bi_2Se_3 from Circular Dichroism Angle-Resolved Photoemission Spectroscopy. *Phys. Rev. Lett.* **107**, 207602 (2011).

20 Medjanik, K. *et al.* Direct 3D mapping of the Fermi surface and Fermi velocity. *Nat. Mater*. **16**, 615, (2017).

21 Pellegrini, C. X-ray free-electron lasers: from dreams to reality. *Phys. Scripta.* **T169**, 014004 (2016).

22 How Diamond Works. *www.diamond.ac.uk/Home/About/How-Diamond-Works*.

23 Undulators. *https://en.wikipedia.org/wiki/Undulator*.

24 Beamlines. *http://www.diamond.ac.uk/Beamlines.html*.

25 Beamlines at Elettra. *https://www.elettra.trieste.it/lightsources/elettra/beamlines.html*.

26 Spectromicroscopy. *https://www.elettra.trieste.it/elettra-beamlines/spectromicroscopy.html*.

27 Dudin, P. *et al*. Angle-resolved photoemission spectroscopy and imaging with a submicrometre probe at the SPECTROMICROSCOPY-3.2L beamline of Elettra. *J. Synchrotron Rad.* 17, 445-450 (2010).

28 Zone plate. *https://en.wikipedia.org/wiki/Zone_plate.*

Chapter 2

Electronic Structure and Effect of Spin-Orbit Coupling in Non-Symmorphic Dirac Line-Node Semimetal *M*SiS (*M*=Zr, Hf)

Topological Dirac semimetals represents a new state of quantum matter that offers a platform for realizing many exotic physical phenomena. New types of Dirac semimetals with robust Dirac line nodes in momentum space have been proposed that extend the bulk band linear touching from discrete points into one-dimensional lines. In this chapter, we will discuss our ARPES measurement on the electronic structure of the proposed semimetals *M*SiS (*M*=Zr, Hf). From the result, we've confirmed the Dirac line-node states in both of the compounds. By comparing the spin-orbit coupling (SOC) effect, we demonstrate that the degeneracy of bands at certain positions of the BZ is protected by crystalline non-symmorphic symmetry.

2.1 Background and Introduction

2.1.1 Introduction to Dirac line-nodes semimetals

Topological non-trivial states have been a hot topic in condensed matter field over last decades for their rich physics and broad application potentials[1-3]. After the evolution in topological insulators (TI)[1,2,4], topological semimetals (TSM)[3] represent a new state of quantum matter recently discovered that offers a platform for realizing many exotic physical phenomena. Different from TIs (e.g. Bi_2Te_3[5], Bi_2Se_3[6]…), the linear dispersions in the band structure of TSMs are formed by the bulk states (instead of surface states in TI)[7,8]. The bulk conduction and valence bands only touch at discrete Dirac/Weyl points or along nodal-lines in momentum space, of which the degeneracies are protected by certain symmetries. The linear dispersions of the Dirac bands and the presence of unique surface states (e.g. Fermi-arcs[9,10]) lead to exciting physics phenomena and application potentials in these TSM systems (e.g. giant magnetoresistance [11,12]). First TSM states have been realized in the topological Dirac semimetal systems $NaBi_3$[13] and Cd_3As_2[14], which locates at the boundary of quantum phase transition from trivial insulator to TI, as illustrated in Fig. 2.1. Ever since then, the field of TSM has been intensively investigated.

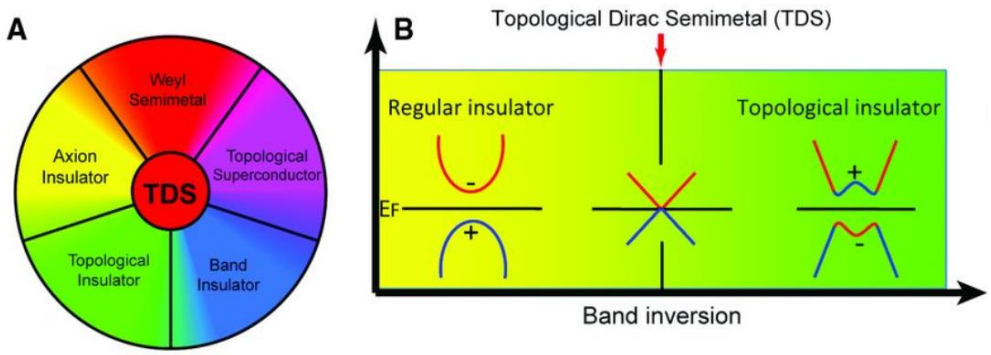

Fig. 2.1 Basic understanding of Topological Dirac Semimetals (TDSM). (a) TDSM states neighbours various novel states. (B) The TDSM state can be realized at the boundary of the quantum phase transition from regular insulator to topological insulator if the degeneracies can be protected by additional symmetries. Adapted from Ref. 13.

The TSMs are generally divided into three groups, which are Dirac semimetals (DSM), Weyl semimetals (WSM) and line-node semimetals (LNSM), as illustrated in Fig. 2.2. Crystal symmetry plays a very important role in realizing different sorts of TSM states.

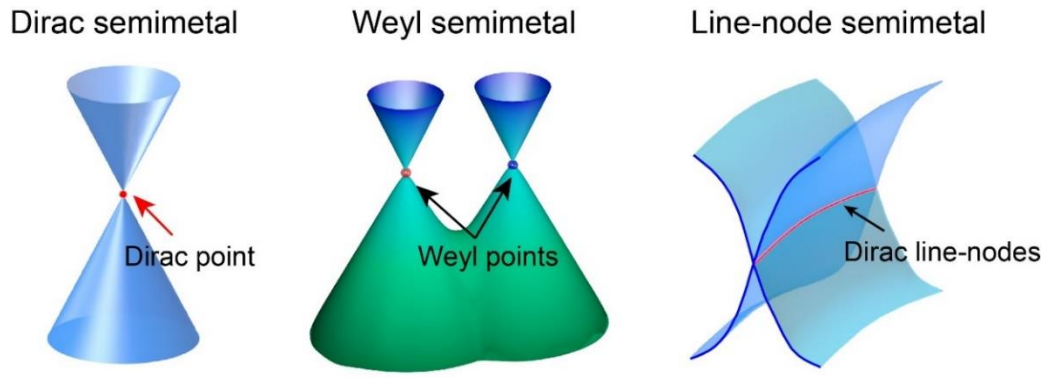

Fig. 2.2 Illustration of different topological semimetal states.

We start with the DSM. In the presence of both time-reversal symmetry and inversion symmetry, doubly degenerated bands cross near Fermi level and form a discrete point in k-

space, which is the so-called Dirac point. Typically, in the currently known DSMs Na_3Bi[13] and Cd_3As_2[15], the degeneracies at Dirac points are topologically protected by the C_3 and C_4 rotational symmetry, respectively, which prevents further gap opening that turns the TS state into a TI state. In the case of point touching, the DSM can naturally host 3D Dirac fermions, making them the 3D analogue of graphene with many exquisite transport properties, including high mobility charge carriers and large magneto-resistance[3,11,12].

If either the aforementioned time-reversal symmetry or inversion symmetry is broken, the DSM state would be turned into a WSM state. The double degeneracy of the bands will be lifted and result in two single degenerated bands which form a pair of Weyl points with opposite chirality. The Weyl points can be viewed as singularity points (either 'source' or 'sink') of Berry curvature, an analogue of magnetic monopoles in k-space. The Fermi arcs, which connect two opposite Weyl points, form unique opening Fermi surfaces which completely violate our traditional understanding of the closed Fermi surface in metals[16]. WSMs represent another intensively investigated topological state with unique physics properties. Several WSM systems have been experimentally realized such as the Ta/Nb monopnictides family (TaAs, NbAs, TaP, NbP)[17,18], $MoTe_2$[19].

Different from DSMs and WSMs, both of which contain band crossings at discrete points (zero-dimensional band crossing), LNSMs have the band crossing in the form of a closed ring or a line (one-dimensional band crossing)[20]. Along some special directions in k-space, the degeneracy of the bands is protected by certain symmetry, which prevents the gap opening from SOC. Compared to the discrete 3D Dirac point, a one-dimensional Dirac line-node is a more significant feature in the band structure and thus can have a stronger contribution to the macroscopic physical properties of these materials (e.g. in transport measurement)[21]. It is natural to infer that LNSMs can be further divided into two types, Dirac

line-node semimetals (e.g. *M*SiS[22]) and Weyl line-node semimetals (e.g. $PbTaSe_2$[23]), according to the degeneracy of the bands.

As discussed above, crystalline symmetry plays a very important role in realizing LNSM states. Introducing non-symmorphic space group symmetry (will be introduced in the next section) is one of the ways to generate LNSM states. In 2015, Steve Young and Charles Kane proposed that non-symmorphic symmetry protects the degeneracy of the bands at certain positions in reciprocal space, which leads to the formation of LNSM states[20]. Moreover, another theoretical work from the Xi Dai's group in Chinese Academy of Sciences gave more detailed calculation on the electronic structure of many LNSM candidates which have similar crystal structures, such as ZrSiO, ZrSiS, HfSiS, ZrSiTe[22]. The theoretical works greatly motivate the relevant experimental research in realizing these novel quantum states.

Nonetheless, the experimental realization of different types of LNSM materials and related research is still insufficient. Only a few of the predicted compounds have been experimentally studied, such as the *M*SiS (*M*=Zr, Hf) family, $PbTaSe_2$ and $PtSn_4$. Among them, $PbTaSe_2$ is inversion asymmetric and hosts "nodal rings" protected by mirror symmetry under SOC[23]. However, various surface states interfering with the bulk features makes the identification of nodal rings difficult. $PtSn_4$ has broken nodal-arcs and its topological character is still under debate, hence is also not a simple system to study[24]. Due to a relatively simple electronic band structure, the *M*SiS family naturally becomes a suitable system for the investigation of LNSM states. Up to date, although recent ARPES reports on ZrSiS[25-27] and the related compound ZrSnTe[28] have shown the existence of the bulk bands with linear dispersion, there has not been a systematic study on the electronic structure in the full 3D BZ to demonstrate the Dirac line-nodes states and their dispersions. It therefore becomes the goal

of our work to clearly illustrate the detailed dispersions of Dirac line-nodes states, discuss the LNSM nature, as well as the SOC effect in different compounds of this family of materials.

In our investigation, by using high-resolution ARPES with broadly tuneable photon energy, we systematically studied the electronic structure of two materials (HfSiS and ZrSiS) of the *M*SiS family. By carrying out broad range momentum space and photon energy dependent measurements, we surveyed multiple BZs along all three momentum directions and were able to identify the electronic bands originating from both the bulk and surface states, which can be well reproduced by our (and previous) ab-initio calculations[25-27]. Moreover, by tracking the Dirac band crossing along different high symmetry directions in the BZ, we clearly observed the Dirac line-nodes states along certain directions and the lifting of the Dirac band degeneracy in other directions due to the SOC effect. The observation of the Dirac line-nodes states in HfSiS and ZrSiS proves the LNSM nature of *M*SiS family of compounds, which have demonstrated many intriguing physical properties (e.g. high mobility electrons and “butterfly" shaped large angular magnetoresistance ~180,000%[21,29-31]).

2.1.2 Non-symmorphic space group symmetry

From the discussion above, we can see that symmetry plays a very important role in the field. The LNSM states in *M*SiS family are protected by non-symmorphic symmetry. Therefore, before going into the experimental details of our work, I would like to first give a brief introduction to the non-symmorphic symmetry space group as well as its protection on the band degeneracy.

A space group is called symmorphic if, apart from the lattice translations, all generating symmetry operations leave one common point fixed[20]. The rotational symmetry operations

and inversion symmetry operations all belong to symmorphic space group. On the contrary, a non-symmorphic space group contains symmetry operations that combine a point group operation *g* with an additional translations *t*, which is a vector fractional to Bravais lattice vector[20].

As a consequence of fractional translation symmetry, the non-symmorphic symmetry brings extra degeneracy in the band structure due to the projection of higher-dimensional representations. This can be easily understood through the band folding theory[20,32].

To start with, let's consider a one-dimensional polymer system as illustrated in Fig. 2.3. To interpret the folded electronic structure, we can impose an infinitesimal super-potential which groups two neighbouring atoms into a pair. The band dispersions after and before the interruption are illustrated in Fig. 2.3(a-b), respectively. The larger unit cell results in a smaller periodicity in reciprocal space. However, in the infinitesimal limit, the electronic structure should continuously evolve to the original one atom case. Therefore, we can understand it in a way that the band structure described in one atom configuration (Fig. 2.3(b)) being folded back to form the dispersion in two-atom pair configuration (Fig. 2.3(b)). The folding process is illustrated in Fig. 2.3(c). Following the same process, if the unit cell is tripled or quadrupled, the band structure will be folded three or four times (Fig. 2.3(d-e)).

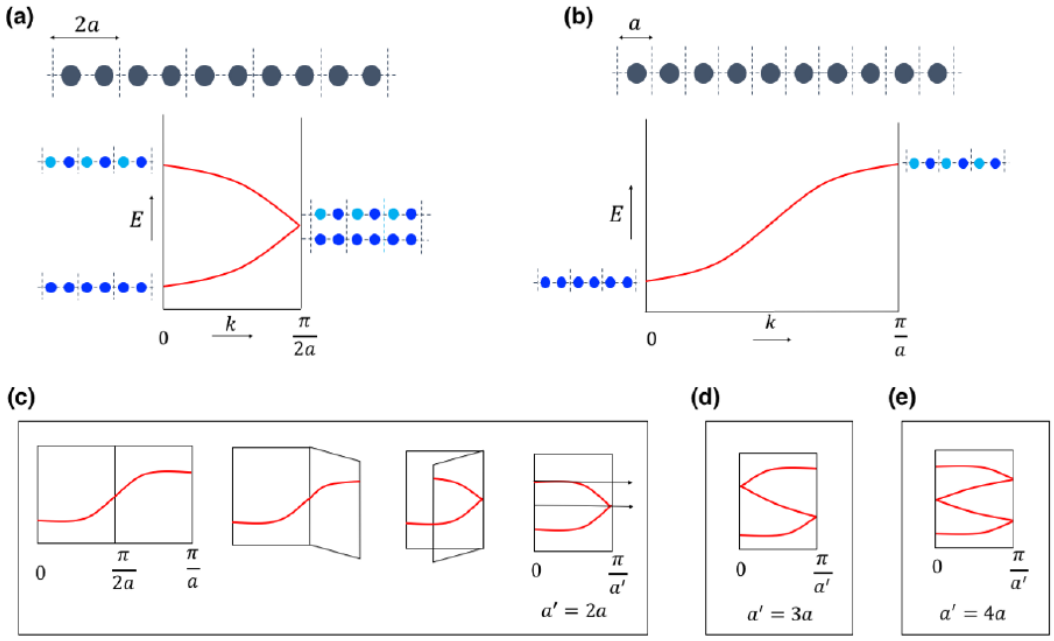

Fig. 2.3 Illustration of band folding in one-dimensional polymers. (a) Band structure of polymers, with a two-atom pair per unit cell configuration. (b) One atom per unit cell configuration. (c) Band folding process. (d-e) Enlargement of the unit cell causes the multiplicity of the bands in tripled and quadruped situation. Adapted from Ref. 32.

Next, let us move on to the 2-dimensional crystal as illustrated in Fig. 2.4. Considering a typical square lattice (Fig. 2.4(a)), the crinkling of the lattice along the z direction between neighbouring atoms will introduce a glide mirror plane and enlarge the unit cell by $\sqrt{2} \times \sqrt{2}$ (Fig. 2.4(b)). Similar to the aforementioned one-dimensional situation, the enlargement of the unit cell will lead to the band folding in momentum space, therefore introduce extra band degeneracy at the boundary of BZ.

The related BZs before (symmorphic symmetry) and after (non-symmorphic symmetry) crinkling of the lattice are illustrated in Fig. 2.4(c), while the dispersions are shown in Fig. 2.4(d). The green area I can be translated back to the green area II, according to the translation symmetry of the red BZ. The green area II is equivalent to the red area II, according to the time-reversal symmetry of the lattice. Therefore, the green area I is

equivalent to the red area II, which means the band dispersion of the non-symmorphic lattice can be generated by folding green area I back to red area II. As illustrated in Fig. 2.4(d-e), band dispersions along Γ–X (M–Γ) direction can be generated by folding band dispersions along previous Γ–X–M' (M'–M–Γ) directions. As can be seen, in this way, extra band degeneracy has been introduced to the system on the boundary of the BZ.

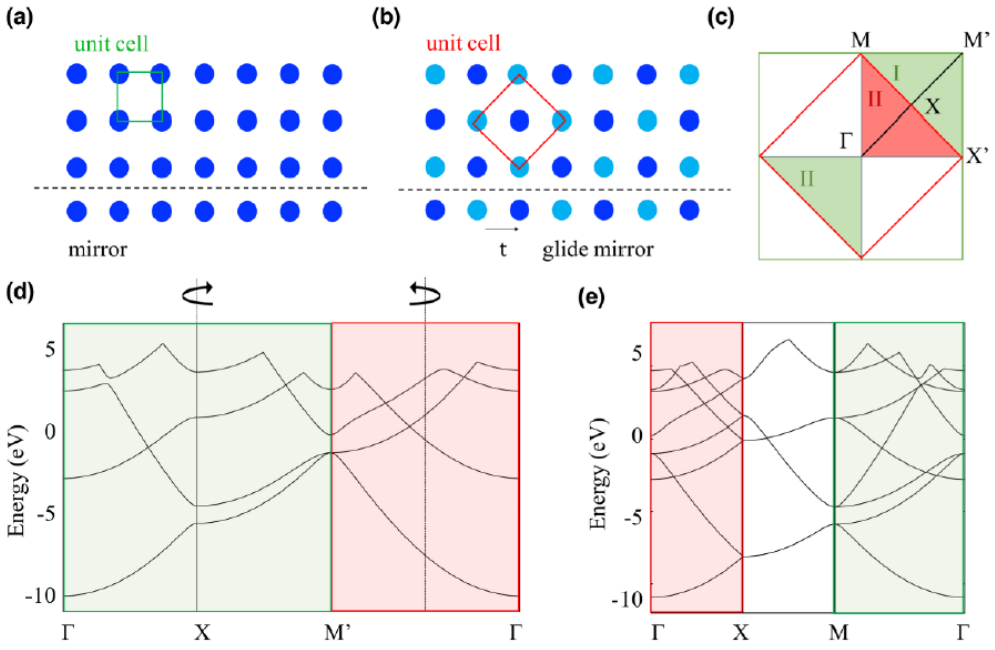

Fig. 2.4 Illustration of band folding in a two-dimensional square lattice. (a) Symmorphic square lattice with mirror symmetry. (b) Non-symmorphic square lattice with glide mirror symmetry. (c) Illustration of BZs of both lattices. (d)-(e) Band folding process to generate the band dispersions of non-symmorphic lattice from the band dispersions of corresponding symmorphic lattice. Adapted from Ref. 32.

It is important to note here that the degeneracy introduced by the band folding in a non-symmorphic system is protected by lattice translation symmetry, which means it cannot be gapped by SOC effect. Detailed explanations of theoretical aspects will not be discussed here but can be found in relevant publications[33,34].

2.2 Electronic structure of HfSiS

2.2.1 Crystal structure and theoretical calculation

Considering that the electronic structure of HfSiS has not been reported and the SOC effect is larger in HfSiS (than ZrSiS), we first focus on this compound. The crystal structure of HfSiS is illustrated in Fig. 2.5(a), clearly showing the Si-Hf/S-Hf/S trilayer structure (PbFCl structure type in the tetragonal P4/nmm space group (No. 129), with lattice constants *a=b=3.52 Å, c=8.00 Å*). Square nets of Si form glide planes in the crystal, while the C_{2x} (C_{2y}) axis of the lattice is screw axis, thus preserving two kinds of non-symmorphic symmetries. The *ab-initio* calculated bulk band structure along high symmetry directions is shown in Fig. 2.5(b), where all the bands at X and M are predicted to be at least doubly degenerated as the glide mirror symmetry $\left\{M_z|\frac{1}{2},\frac{1}{2}\right\}$ requires the band degeneracy at X and the screw axis symmetry $\left\{C_{2x}|\frac{1}{2},0\right\}$ requires the band degeneracy at X and M in the 2D non-symmorphic lattice within P4/nmm group. Extending to 3D, all corressponding lines along k_z (R-X, A-M) still preserve the same symmetries with the addition of inversion symmetry, thus forming degenerated lines, including the Dirac line-nodes formed from the crossing of two linear bands (Fig. 2.5(c)).

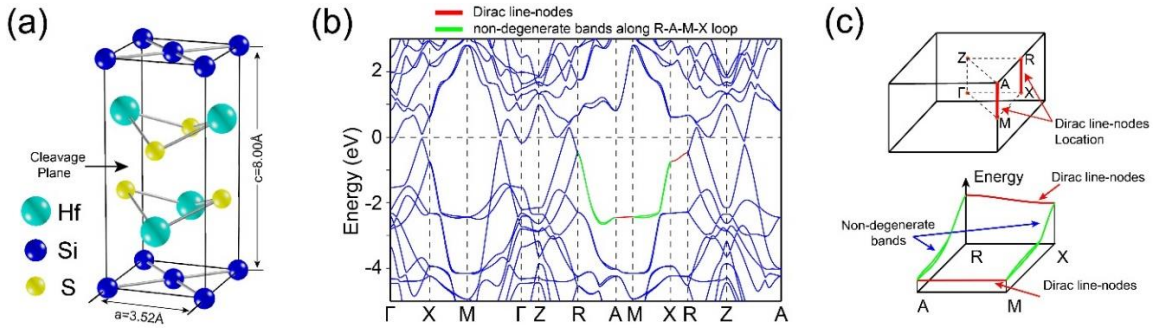

Fig. 2.5 Crystal and band structure of HfSiS. (a) Crystal structure of the HfSiS, showing the stacking of Si and Hf-S planes. The most probable cleavage plane is indicated. (b) Calculation results of the bulk band structure of HfSiS along high-symmetry directions. Green lines indicate the positions where the bands are non-degenerate while the red lines indicate the Dirac line-nodes. (c) Illustration of the Dirac line-nodes location (upper panel) and the dispersion of the line-nodes (lower panel).

The density functional theory (DFT) calculation discussed in this chapter was performed by our collaborator, Binghai Yan's group, by using the Vienna ab initio simulation package (VASP) with the projected augmented wave method (PAW). The exchange and correlation energy was considered in the generalized gradient approximation (GGA) with Perdew-Burke-Ernzerhof (PBE) based density functional. The energy cutoff was set to 259 eV. Experimental lattice constants were used for two compounds in all the calculations. To calculate the surface states in the material (discussed later in the chapter), a (001) slab model of five bulk units thick (40 Å) was constructed with the periodicity in the xy plane and a vacuum layer of 20 Å in the z direction to simulate the (001) surface. The slab band structure was projected to the atomic orbitals of top one unit cell, to identify the surface states.

2.2.2 Crystal synthesis and basic characterization

Single crystals of HfSiS were grown via iodine (I_2) vapor transport in a two steps process. Firstly, the polycrystalline HfSiS powder was synthesized using high-purity elemental Hf piece, Si piece, S powder. Then the polycrystalline powder together with iodine was sealed in a quartz tube under vacuum. The quartz tube was kept in a gradient furnace for 10 days with the powder at 1100˚C, while the cooler end at 1000˚C. Shiny rectangular plate-like crystals were obtained at the cooler end. After cleaving inside the ultrahigh vacuum chamber, large (mm scale) flat and shiny surfaces are exposed (Fig. 2.6(a)(i)), which is ideal for ARPES measurements. The high quality of the crystal can be verified by the X-ray diffraction (XRD) measurements (Fig. 2.6(b)(ii-iv)); and the core level photoemission spectrum clearly shows the characteristic Hf_{4f}, S_{2p} and Si_{2p} peaks (Fig. 2.6(b)). The broad Fermi surface mapping in Fig. 2.6(c) covering multiple BZs confirmed the high quality (001) cleavage plane, which allows us to carry out the ARPES measurements below.

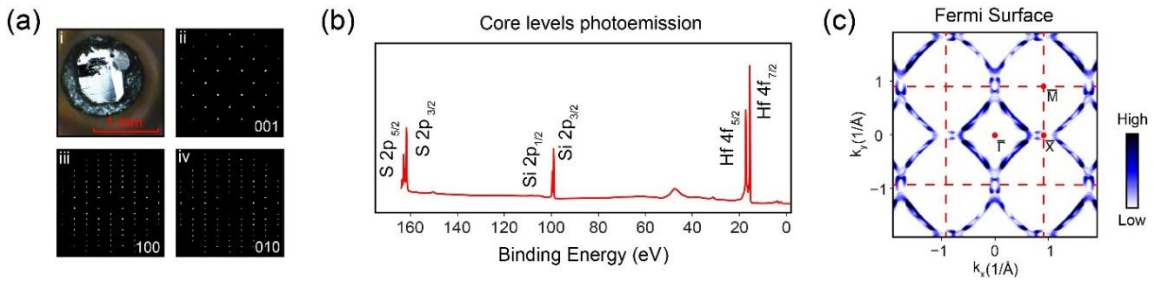

Fig. 2.6 Basic characterizations of HfSiS. (a) (i) Photograph of the HfSiS crystal cleaved along a <001> direction, (ii-iv) XRD pattern of the (001), (100) and (010) surface of HfSiS. (b) Core level spectrum of HfSiS showing characteristic S_{2s}, Si_{2p} and Hf_{4f} core level peaks. (c) Broad range photoemission spectral intensity map of the Fermi-surface covers 9 BZs, showing the correct symmetry and the characteristic FS.

2.2.3 General electronic structure

High-resolution ARPES measurements were performed. We investigated the detailed electronic structure of HfSiS within a BZ with high-momentum and energy resolution, and an example is shown in Fig. 2.7. From the 3D plot of the overall band structure (Fig. 2.7(a)) and the constant energy contours (Fig. 2.7(b)(i-iv)), one could clearly identify two sets of features. One is the large diamond-shaped Fermi surface (FS), forming delicate structures connecting four $\bar{X}$ points; and the other refers to the two concentric ellipses centred at each $\bar{X}$ point. Both features can be well reproduced by our *ab-initio* calculations (Fig. 2.7(b)(v-viii)), which also helped us to identify their bulk (the diamond shape FS feature) and surface (the ellipses) origin.

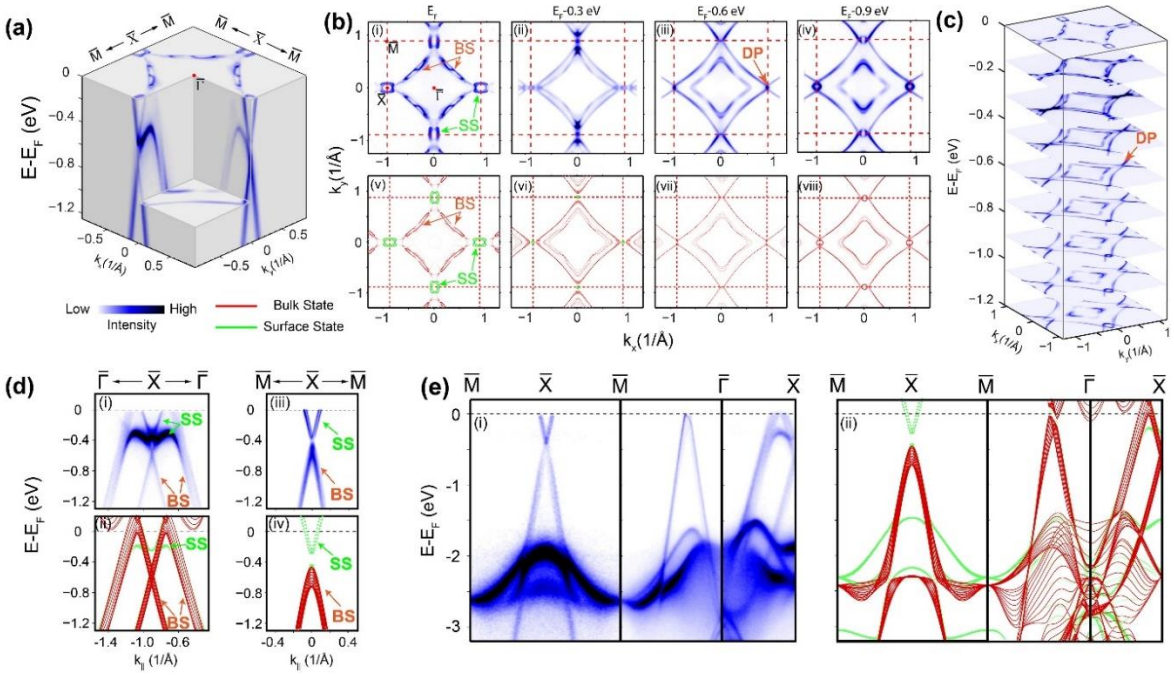

Fig. 2.7 General electronic structure of HfSiS. (a) 3D intensity plot of the photoemission spectra centered around $\bar{\Gamma}$. (b) Top row: Photoemission spectral intensity map showing the constant energy contours of bands at E_B=0 (i), 0.3 (ii), 0.6 (iii) and 0.9 eV (iv), respectively. Bulk state (BS), surface state (SS) and Dirac point (DP) are labelled. Bottom row (v)-(viii): Corresponding calculated constant energy contours at the same binding energies as in experiments above. (c) Stacking plots of constant-energy contours in broad binding energy range show the band structure evolution. (d) High symmetry cut along $\bar{\Gamma} - \bar{X} - \bar{\Gamma}$ (i) and $\bar{M} - \bar{X} - \bar{M}$ (iii) near E_F, together with their corresponding calculated band structure (ii,iv). BS and SS are labelled on the data and represented by red and green color in the calculation. (e) Broad range high symmetry cut along $\bar{M} - \bar{X} - \bar{M} - \bar{\Gamma} - \bar{X}$ (i) and corresponding calculated band structure (ii). BS and SS are represented by red and green color in the calculation.

For the concentric surface state (SS) FSs around the $\bar{X}$ points (see Fig. 2.7(b, c)), one can see that they are formed by a pair of Rashba-split bands (the splitting is most apparent along $\bar{M} - \bar{X} - \bar{M}$, see Fig. 2.7(d)(iii), detailed discussion can be found in section 2.3.3), indicating the large SOC effect in HfSiS. The constant energy contours of this set of SS keep

shrinking in size and eventually terminate at $E_b \approx 0.4$ eV. Meanwhile, the linear bulk band dispersions (Fig. 2.7(b)(iii) and Fig. 2.7(d)(i)) form a Dirac point ($E_b \approx 0.6$ eV) at $\bar{X}$. We note that the slight broadening of the bulk band in Fig. 2.7(d)(i) is due to the k_z broadening effect, as can be clearly seen in the *ab-initio* calculation (Fig. 2.7(d)(ii)), where the overlap of dispersions with different k_z momentum (red curves) well reproduce the k_z broadening. The excellent overall agreement between the experiments (Fig. 2.7(d)(i,iii) and (e)(i)) the calculation (Fig. 2.7(d)(ii,iv) and (e)(ii)) also allowed us to distinguish the additional SSs (green curves in Fig. 2.7(d)(ii,iv) and (e)(ii)) from the bulk states (discussed later in Section 2.2.5). This consistency simplified our investigation of the bulk states and the identification of the bulk Dirac line-node.

2.2.4 Photon energy dependence

Changing the incident photon energy provides us the ability to access the electronic structure of materials with different k_z value. Systematic photon energy dependent ARPES experiments were performed on HfSiS in order to comprehensively reveal its electronic structure and to trace the Dirac line-nodes. The inner potential for HfSiS was determined to be V_0=15.8 eV, as verified from the k-space conversion of the equal energy contour at E_b = 1.8 eV shown in Fig. 2.8(a). From this contour, we can clearly identify periodic band features along the k_z direction which matches very well with the BZ. This allows us to determine the high symmetry points in the BZ and extract the k_z value of each cut measured with certain photon energy. The two cuts measured along X-Γ-X (k_z =0, measured with $h\nu$ =138 eV) and R-Z-R (k_z =π, measured with $h\nu$ =158 eV) are plotted in Fig. 2.8(b). Although the overall band structure looks similar, differences can be observed, such as the band top at

$k_{||}$=0 and the binding energy of the Dirac point at X/R, which are in agreement with the bulk band structure calculation (Fig. 2.8(c)).

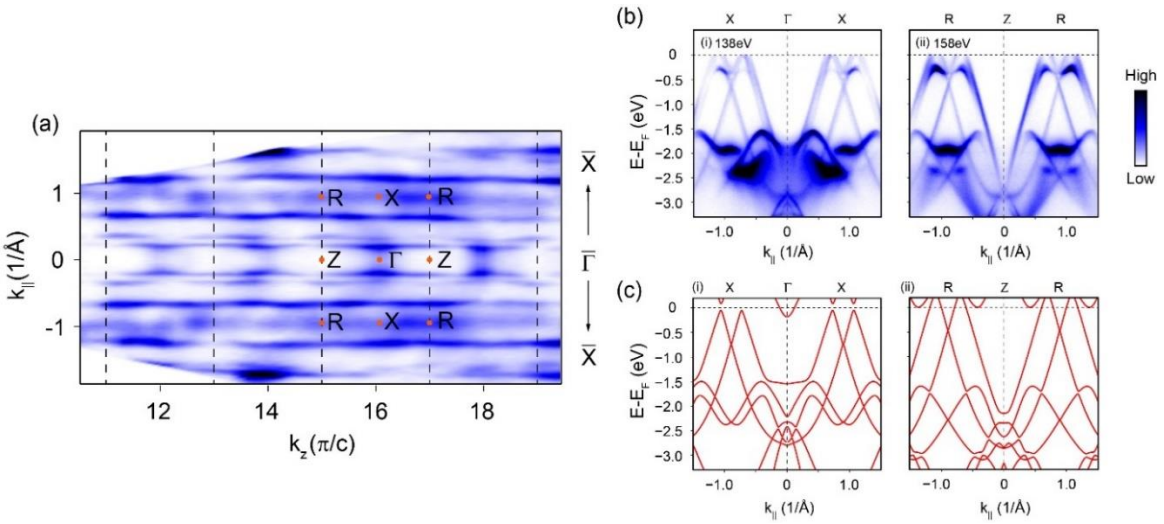

Fig. 2.8 Photon energy dependent ARPES experiment. (a) Constant energy contour at 1.8 eV below E_F in the $k_{||}$ vs. k_z plane of HfSiS. High symmetry points are labeled. (b) High symmetry X-Γ-X and R-Z-R cuts of HfSiS. (c) *Ab initio* calculation results of bulk band structure along X-Γ-X and R-Z-R.

With the help of photon energy dependent ARPES experiments, we are able to analyze some detailed features of the electronic band structure, such as the bulk and surface states at $\bar{X}$ and the evolution of the $\bar{\Gamma} - \bar{M}$ bulk band structure along k_z direction. Detailed analysis will be presented in the following section.

2.2.5 Detailed electronic structures

Firstly, let's focus on the band structure at $\bar{X}$. The surface states (SS) are very close to the bulk states (BS) around $\bar{X}$, making them hard to identify. Therefore, we will present more detailed band structures from both our measurements and *ab initio* calculations, as well as their comparison to explain how the SS and BS can be distinguished.

Fig. 2.9(a) shows calculated band structure of the high symmetry cut around the $\bar{X}$ point along $\bar{\Gamma} - \bar{X} - \bar{\Gamma}$ direction. The electronic states originated from the bulk and surface are of red and green color, respectively. Let's first focus on the region near E_F, where we could clearly observe the dispersion of BS which forms a large "M" shape, and each (red) line reflects the dispersion of the BS at different k_z values. The SS, on the other hand, contains two parts: a "V" shape close to E_F and a flatter "M" shape at higher binding energy, that partially merging into the BS.

The measurement results show good agreement with the calculation results: the flatter "M" shape SS can be easily identified in our data in all photon energies (as shown in Fig. 2.9(b-c)). While the "V" shape SS is very close to the BS, they can still be resolved at a photon energy of 142 eV, as shown in Fig. 2.9(c), with BS and SS marked by red and green dashed line. All these characters show good agreement with the *ab initio* calculations.

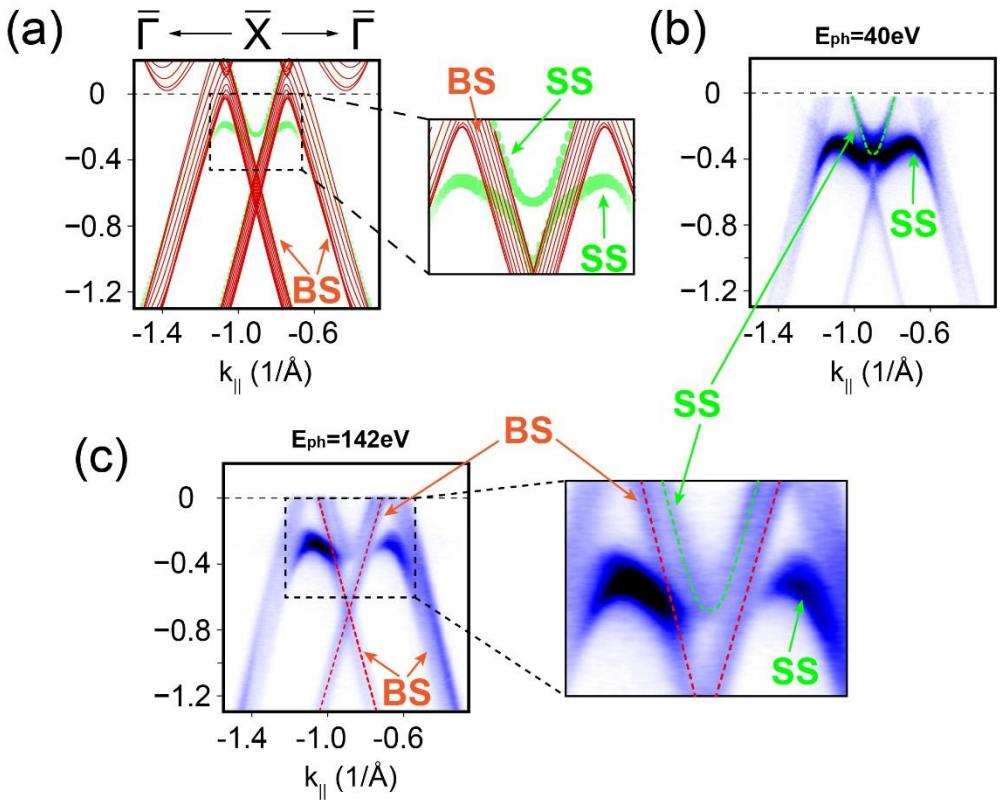

Fig. 2.9 Bulk and surface states at $\bar{X}$. (a) Calculated band structure of the high symmetry cut along $\bar{\Gamma} - \bar{X} - \bar{\Gamma}$ near E_F, the BS and SS are represented by red and green colors respectively. (b),(c) Corresponding photoemission spectra, taken at photon energy 40 eV in (b) and 142 eV in (c). BS and SS are clearly resolved and indicated by red and green dashed lines.

Next, let's move to the other feature: the evolution of the $\bar{\Gamma} - \bar{M}$ bulk band structure along the k_z direction. As can been seen from the calculation in Fig 2.10(b), bulk bands cross along $\bar{\Gamma} - \bar{M}$ direction, which is gapped by the SOC due to the lack of symmetry protection. The gap size is critical for the later comparison of the SOC effect between ZrSiS and HfSiS (Section 2.3.3). However, k_z broadening effect blurs the band dispersion at M. Therefore, the evolution of the bulk band structure along $\bar{\Gamma} - \bar{M}$ should be made clear first. The ZrSiS data is presented instead here for a better illustration due to better data quality. The data for HfSiS is analysed in the same method.

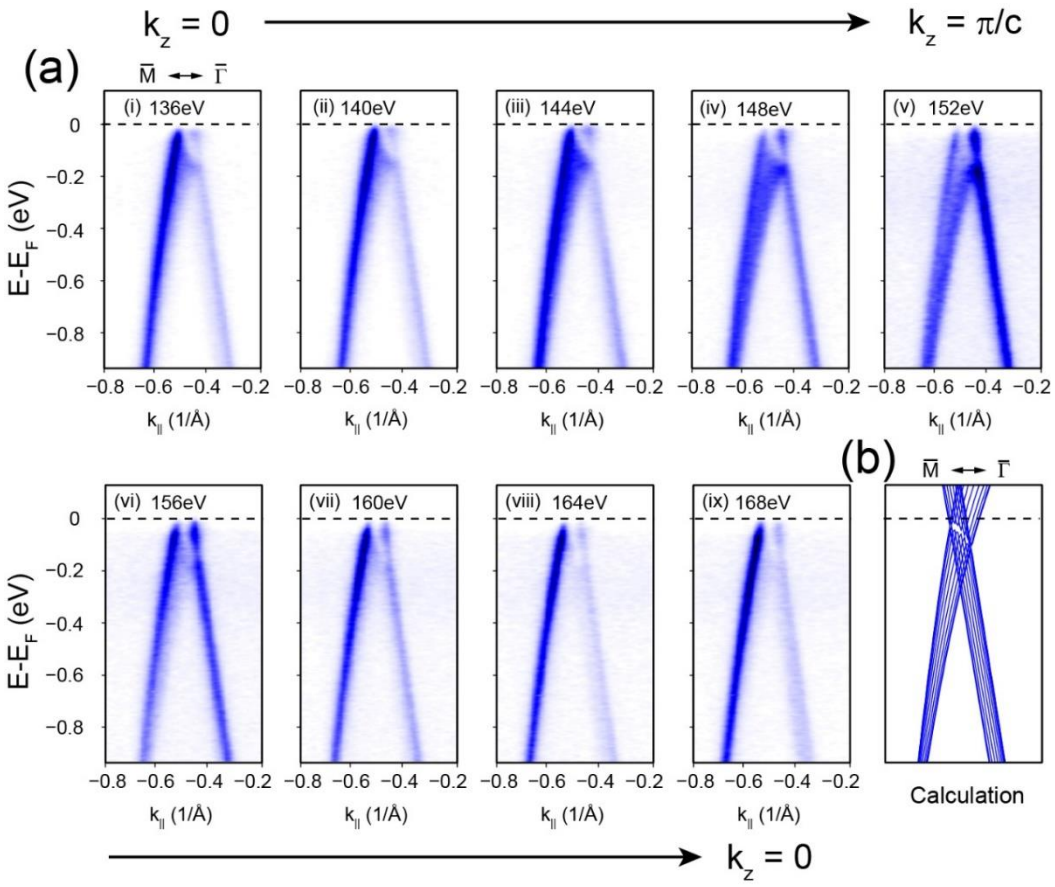

Fig. 2.10 k_z evolution of bulk band structure along $\bar{\Gamma} - \bar{M}$. (a) High symmetry $\bar{\Gamma} - \bar{M}$ cut of ZrSiS measured at various photon energies. (b) *Ab initio* calculation of the bulk bands along $\bar{\Gamma} - \bar{M}$ with bands spanning the whole range of k_z values.

The evolution of the bulk band structure along $\bar{\Gamma} - \bar{M}$ at various photon energies (thus different k_z values) is plotted in Fig. 2.10(a). From the plots of all the cuts, we could see that the electron pocket observed near E_F has the strongest intensity at $h\nu$ =152 eV (close to $k_z = \pi/c$) and becomes weaker when $h\nu$ approaches either 136 or 168 eV (close to $k_z = 0$). This observation is consistent with the band structure calculation (the electron pocket moves up from $k_z = \pi/c$ to $k_z = 0$). However, even at $k_z = 0$ (close to $h\nu$ = 136 eV) we could still observe some remaining intensity of electron pocket which is projected from the strongest

counterpart at $k_z = \pi/c$. Such result clearly reflects the k_z broadening due to the limited k_z resolution from the final state effect in HfSiS and ZrSiS. Taking this consideration into account, we can view the experimental band dispersions along $\bar{\Gamma} - \bar{M}$ as the superposition of bulk bands from all k_z.

In the following, an intuitive picture of the k_z broadening effect, which is a very usual and intrinsic phenomenon in photoemission, is given. Due to the inelastic absorption and elastic reflection from the crystal potential, the final states of the excited photoelectron is intrinsically damped towards interior of the solid[35]. Such confinement in the direction perpendicular to the sample surface is equivalent to certain intrinsic broadening in k_z by the uncertainty principle. As a result, the final state in our experiment is formed by all initial states within the range of k_z broadening. The phenomenon is caused by the fundamental physics in the photoemission process, therefore, cannot be removed by improving the resolution of the equipment. Detailed explanation can be found in *Ref. 35*.

2.3 Dirac line-nodes and effect of SOC

2.3.1 Dirac line-nodes in HfSiS

After establishing the general electronic structure for both HfSiS and ZrSiS (As there are already publications on the electronic structure of ZrSiS, its detailed electronic structure is not discussed here (relevant data was later published in *Ref. 36*). We now focus on the dispersion of Dirac line-nodes along different paths in the BZ. As illustrated in Fig. 2.11, the dispersion along X-R directions was obtained by conducting photon energy dependent ARPES experiments. From a series of measurements at different k_z along (0, 0, k_z) - (π/a, 0, k_z) direction, we clearly observed that the Dirac node formed by linear band crossing disperses

with k_z and results in a line-node along X-R direction. Fig. 2.11(b-c) illustrate the measuring process and describe the dispersing of the Dirac line-node in energy-momentum space.

Similar to the X-R line-node, the predicted bulk band Dirac line-node along the M-A direction was also observed, though less dispersive (Fig. 2.11(e)).

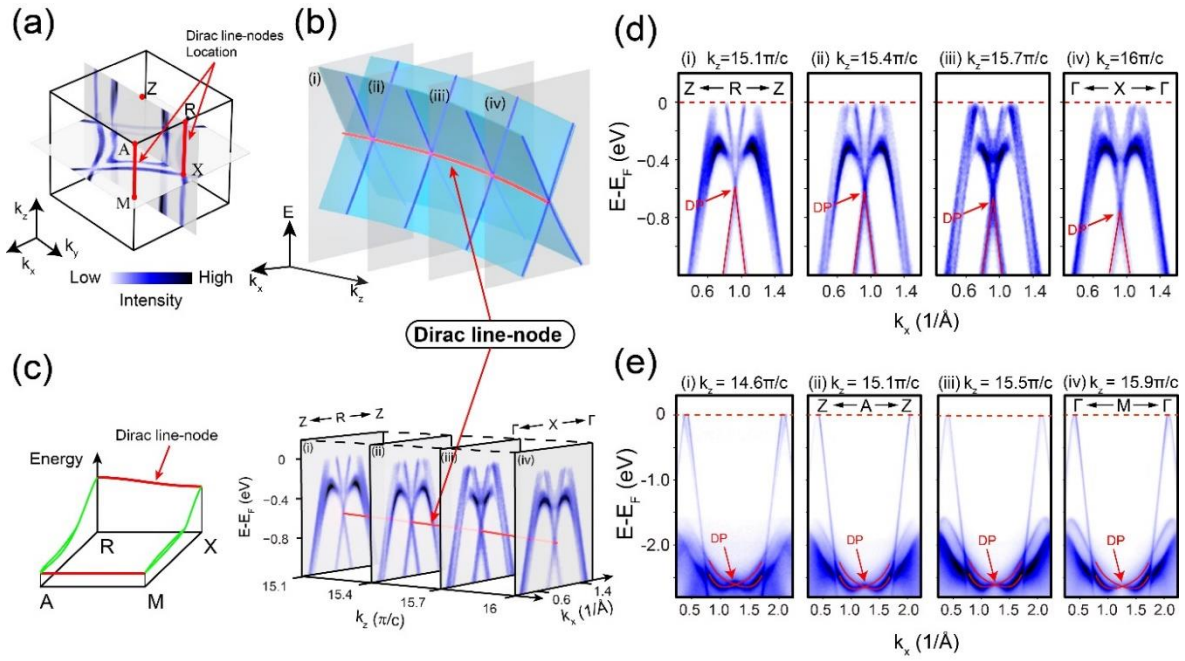

Fig. 2.11 Dispersion of Dirac line-nodes in HfSiS. (a) Illustration of the location of Dirac line-nodes in HfSiS. The 3D BZ also shows the constant energy contours in the k_y-k_z plane (with k_x=0) and k_x-k_y plane (with k_z=0) with energy around the DP. (b) Schematic of the band structure hosting a Dirac line-node along the k_z direction. Grey planes represent locations where each cut in (c) is measured and blue lines represent the Dirac dispersion we would observe in each cut. (c) Left panel, Schematic of the dispersion of the line-node. Right panel, stack plot of the four cuts along (k_x,k_y)=(0,0) to (k_x,k_y)=(0,π/a) with k_z values ranging from 15 to 16 π/c. (d) Detailed analysis of the four cuts shown in (c) with the linear fitting results of the Dirac bands marked by red lines. (e) Plot and band fitting result of four representing cuts along (k_x,k_y)=(0,0) to (k_x,k_y)=(π/a,π/a) with k_z values ranging from 14.6 to 16 π/c. Fitted parabolic dispersions and DP positions are labelled.

By fitting the Dirac dispersions in the aforementioned cuts, exact binding energy of the Dirac point can be easily accessed. As illustrated in Fig. 2.12(a), momentum distribution curves (MDC) were extracted from the measured band dispersion. Linear dispersion of the two Dirac bands below the Dirac point was firstly fitted based on the peak position in MDCs. Then the position of the Dirac point was calculated by the crossing point of the two bands. In this way, with measurements with finer k_z step, the dispersion of the line-node along X-R could be reconstructed. As illustrated in Fig. 2.12(b), the fitted experimental dispersion shows good agreement with our calculations (solid red curve). The dispersion of the A-M line-node is also reconstructed as shown in Fig. 2.12(c-d).

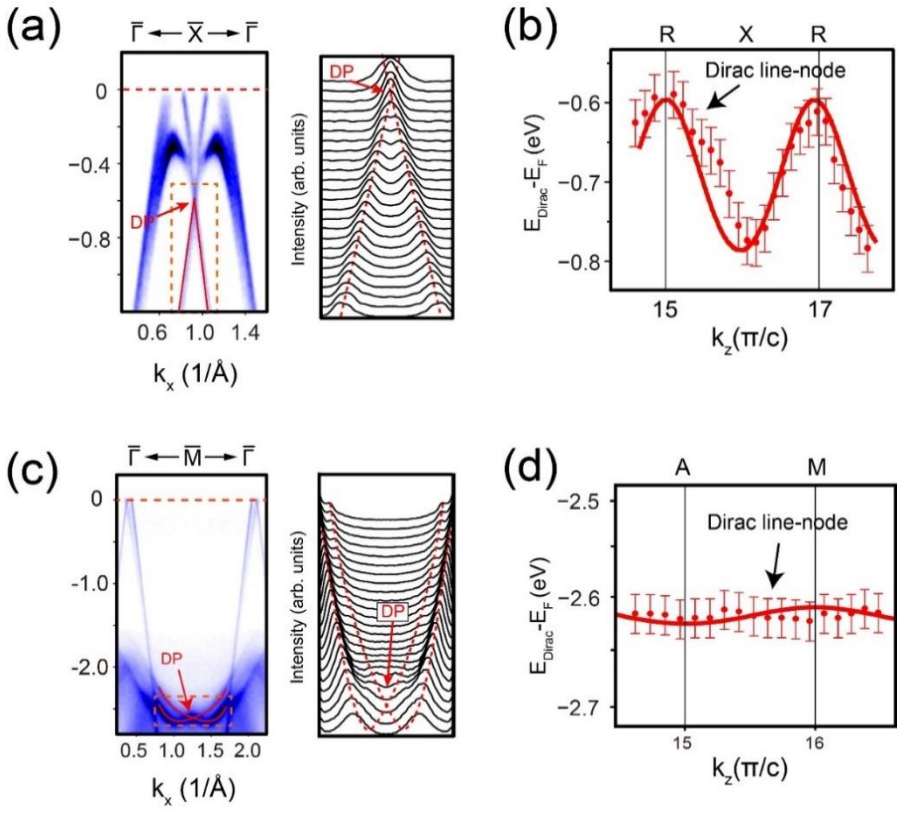

Fig. 2.12 Fitting of the Dirac bands. (a) Dirac band dispersion along $\bar{\Gamma} - \bar{X} - \bar{\Gamma}$ and the related MDC plot of the region around the Dirac point (indicated by the dashed box). (b) The fitted DP positions at various k_z values, the red curve indicates the calculated dispersion along R-X-R. (c-d) Same as (a-b) but for Dirac dispersion along $\bar{\Gamma} - \bar{M} - \bar{\Gamma}$.

2.3.2 Dirac Line-nodes in ZrSiS

Similarly, our measurement on ZrSiS have also obtained similar results on the Dirac line-nodes (see Fig. 2.13), with the Dirac line node along X-R and M-A, but with slightly weaker dispersion along the R-X-R direction (Fig. 2.13(c)).

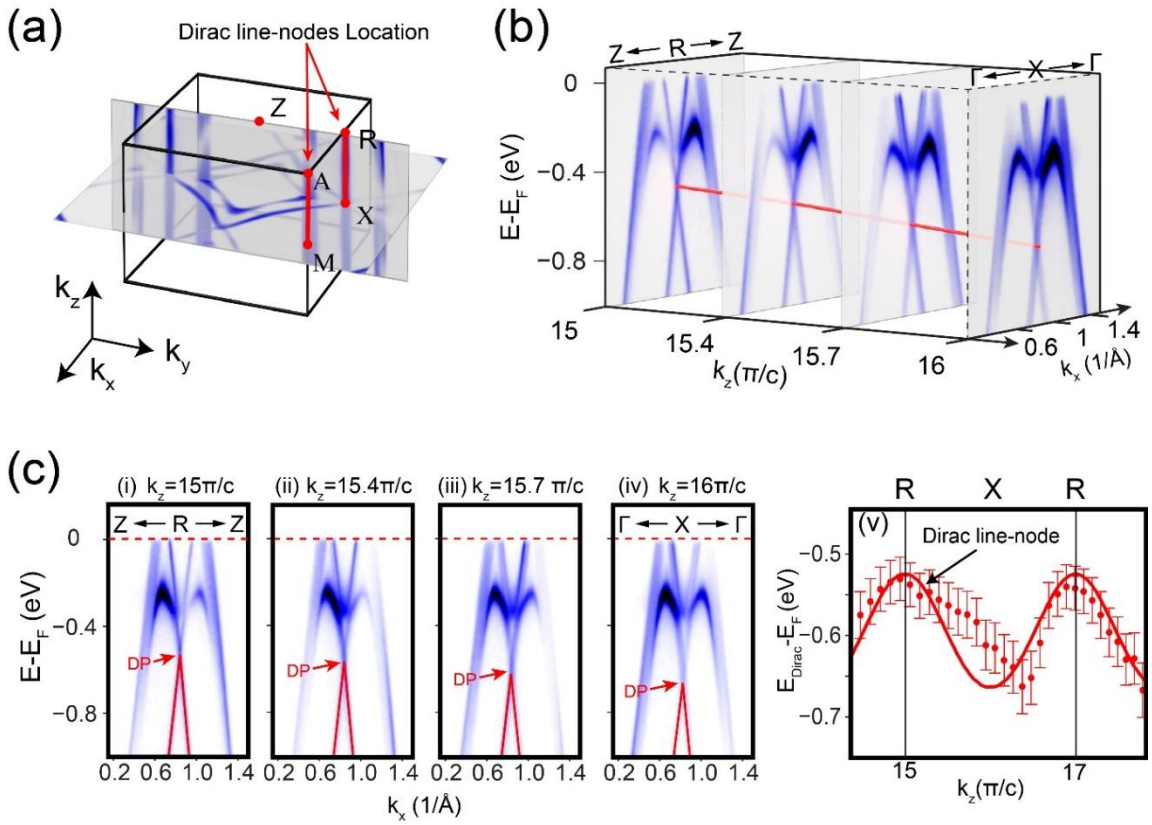

Fig. 2.13 Dispersion of Dirac line-nodes in ZrSiS. (a) Illustration of the location of Dirac line-nodes in ZrSiS. The 3D BZ also shows the constant energy contours in the k_y-k_z plane (with k_x=0) and k_x-k_y plane (with k_z=0) with energy around the DP. (b) Stack plot of four cuts along (k_x,k_y)=(0,0) to (k_x,k_y)=(0,π/a) with k_z values ranging from 15 to 16 π/c. Red curve indicates the Dirac line-node. (c) (i)-(iv) Detailed analysis of the four cuts shown in (b) with the linear fitting results of the Dirac bands marked by red lines and DP labelled. (v) The fitted DP positions at various k_z values, the red curve indicates the calculated dispersion along R-X-R.

In conclusion, we have systematically demonstrated the Dirac line-nodes states along X-R and M-A in both compounds. As predicted in the calculation, these Dirac line-nodes states are protected by non-symmorphic symmetry. Indeed, no evidence of gap opening was observed in our high-resolution ARPES spectra. Our detailed analysis unambiguously confirms HfSiS and ZrSiS to be Dirac line-nodes semimetals.

2.3.3 Effect of SOC

The similarity of the crystal structures provides us a chance to compare the band structures tuned by different SOC between LNSM HfSiS and ZrSiS. In the above discussion, we have already confirmed that the Dirac line-node states in both compounds are robust even when the SOC is switched on. Here, to have a better illustration on that, we now move to other band structures where the degeneracy is not protected by symmetry.

On the Fermi surface maps of both HfSiS and ZrSiS (Fig. 2.14(a)), one clear signature of the effect is the split surface state around $\bar{X}$, where the two concentric pockets with a distinct separation can be seen in HfSiS (Fig. 2.14(b)(i-ii), the Rashba parameter estimated is 3.1 eVÅ). In comparison, due to a weaker SOC effect, the Rashba splitting in ZrSiS is almost invisible as illustrated Fig. 2.14(b)(iii-iv).

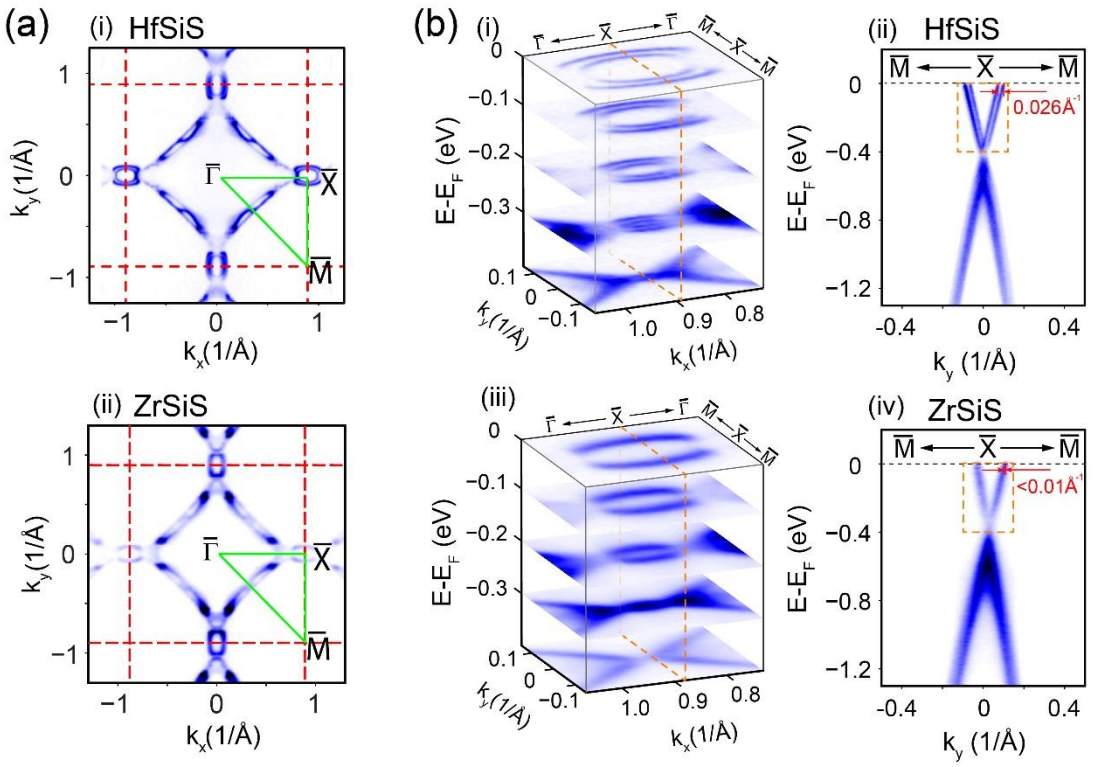

Fig. 2.14 Effect of SOC on the surface states. (a) Constant energy contour on E_F of HfSiS (i) and ZrSiS (ii). (b) (i-ii) 3D intensity plot of the photoemission spectra centered at $\bar{X}$ and the high symmetry $\bar{\Gamma} - \bar{X}$ cut of HfSiS. (iii-iv) Same plot for ZrSiS. The SS Rashba splitting in both materials are estimated and labelled.

In addition to the split surface states, the SOC also results in large bulk band splitting. As an example, along Γ-X (Fig. 2.15), there are two bulk bands at high binding energy showing a large splitting in HfSiS (Fig. 2.15(a)(i)), which is caused by strong SOC effect in this compound. Accordingly, in ZrSiS, the band splitting is clearly smaller (Fig. 2.15(a)(iii)). This difference agrees well with our *ab initio* calculation (Fig. 2.15(a)(ii, iv)). Moreover, as we have mentioned in section 2.5.5, the bulk band along $\bar{\Gamma} - \bar{M}$ is also gapped by the SOC effect. For a comparison, the same dispersion cuts from both compounds are illustrated here in Fig. 2.15(b). We can see that the band gap in HfSiS (~80 meV) is significantly larger than that in ZrSiS (~50 meV), which is consistent with calculation.

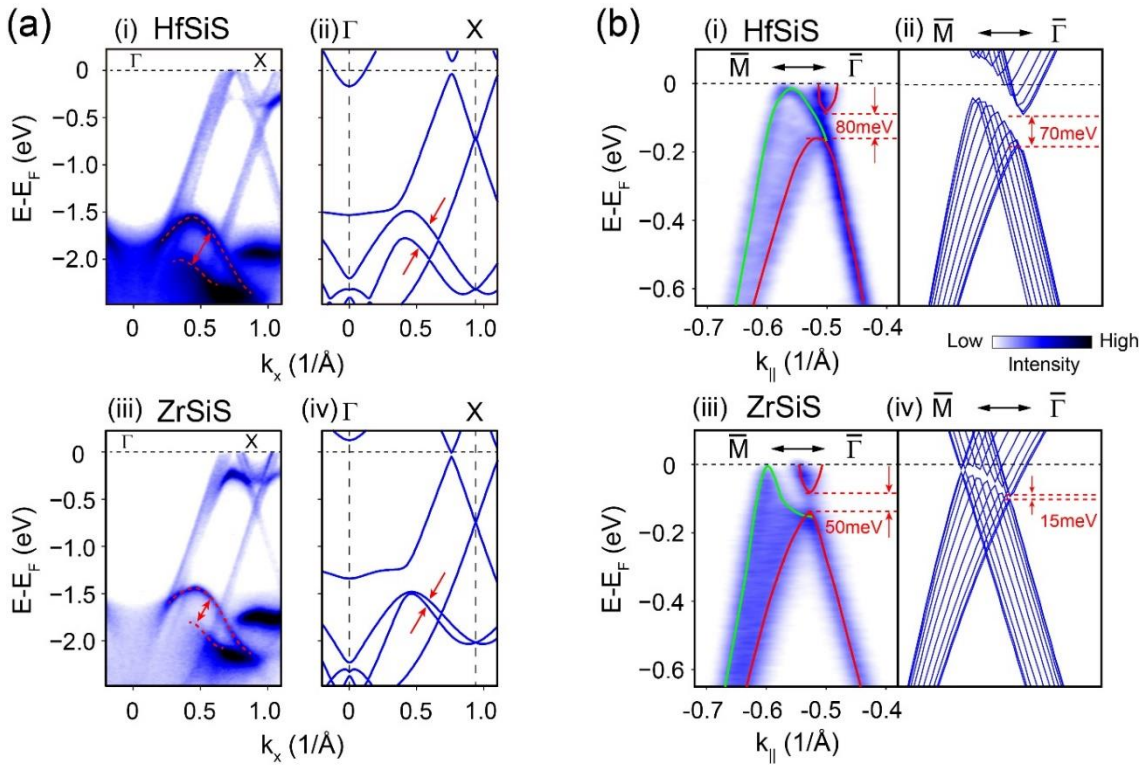

Fig. 2.15 Effect of SOC on the bulk bands. (a) Comparison of the high symmetry Γ-X cut and corresponding band structure calculation of HfSiS (i-ii) and ZrSiS (iii-iv). The band splitting in both materials are labelled. (b) Comparison of the high symmetry $\bar{M} - \bar{\Gamma}$ cut and corresponding band structure calculation of HfSiS (i-ii) and ZrSiS (iii-iv). In the spectrum, red curve labels the contour of the spectral weight at $k_z=\pi$ while the green curve labels the spectral weight from other k_z values. The band gap between the electron and hole pockets are estimated and labelled. In the calculations, the band structure at all k_z values are overlapped to reflect the uncertainty of k_z values that each cut covers. The band splitting between the electron and hole pockets at $k_z= \pi$ are labelled.

In conclusion, we found several examples to illustrate the effect of SOC in both compounds. The comparison between the two compounds demonstrates a larger SOC effect in HfSiS, which is consistent with theoretical predictions. The band splitting and band gap opening illustrated are in great contrast to the Dirac line-nodes states along X-R and M-A, which are robust against SOC effect. Therefore, we now have a deeper understanding of how

the Dirac line-nodes states are protected by the non-symmorphic symmetry in the LNSM materials.

2.4 Discussions and Perspectives

Before going deeper into the discussion, let us first briefly summarize our experimental data presented above:

1. We have revealed the detailed electronic structure of HfSiS, which shows excellent consistency with our *ab initio* calculation.
2. Predicted Dirac line-nodes states in both HfSiS and ZrSiS are confirmed by our high-resolution ARPES data.
3. The effects of SOC on two compounds are compared. The band splitting and gap opening were observed along momentum directions which are not protected by the crystalline symmetry.

From all the data presented, we have systematically revealed the Dirac line-nodes states in the *M*SiS (*M*=Zr, Hf) family, therefore clearly established that these compounds are Dirac line-nodes semimetals protected by non-symmorphic symmetry. The comparison of the effect of SOC on these two compounds illustrates how the crystalline symmetry protects the band degeneracy in certain high symmetry directions. The detailed characterization of the electronic structures of this family of compounds will not only help us understand their intriguing transport properties but also provide a solid base for designing and realizing exotic topological quantum phases and possible future applications using these materials. Especially, by tuning the Dirac point of the *M*SiS materials to the E_F vicinity, it is believed that exotic transport properties might be further enhanced.

Our study on the *M*SiS family greatly motivate the relevant researches on similar material systems. Many recent theoretical and experimental results on the Dirac line-nodes semimetals have been published, e.g. the research on ZrGe*M* (*M* = S, Se, Te)[37], HfGeTe[38],CeSbTe[39].

Before finishing this chapter, I want to discuss the topological nature of the *M*SiS material systems in more detail.

There are several transport investigations that reported evidence for the non-trivial topology in the *M*SiS family. For examples, the experimental signature of topological nodal line fermions (by analyzing the de Haas–van Alphen quantum Oscillations) was demonstrated[30]; and the extraction of the filling factor provides a non-trivial Berry phase of 0.5 which indicates the nontrivial transport and evidences the Dirac cones[27]. In another recent study on ZrSiS[29], extremely large, non-saturating magnetoresistance (MR) was obtained at low temperature ($\sim 1.4 \times 10^5\%$ at 2 K and 9 T, comparable with topological Dirac semimetals and topological Weyl semimetals). The negative MR reported, which weakens and then vanishes with increasing temperature, was observed at 2 K and has been ascribed to the chiral magnetic effect, a characteristic property of the topological Dirac and Weyl semimetals.

Several ARPES papers before our work also used the term ‘topological’ to define the Dirac line-nodes states in the material system[26,27]. However, none of the work has demonstrated the topological origin from either theoretical calculations or the experimental observations. In our study, we did not see any signatures of topological non-trivial states from the Dirac line-nodes studied. Therefore, the question arises whether the *M*SiS family is a topological non-trivial system. If not, how can we understand the non-trivial transport phenomena?

A recent review article from Mazhar N. Ali's group provides suggestion on the issue[32]. As illustrated in Fig. 2.16, several Dirac band crossings were observed in the theoretical calculations for the situation without SOC. They are divided into two groups. The crossings shown by green lines (which are the Dirac line-nodes states in our study) are located within the glide mirror plane, therefore protected by the non-symmorphic symmetry. On the contrary, the crossings labelled with red are not protected, therefore open gaps under the effect of SOC. Other paper suggests that these crossings labelled with red are topological non-trivial, resulted from the inverse band crossing[22]. However, unfortunately, these band structures are located above the Fermi level, which cannot be accessed by the ARPES experiment.

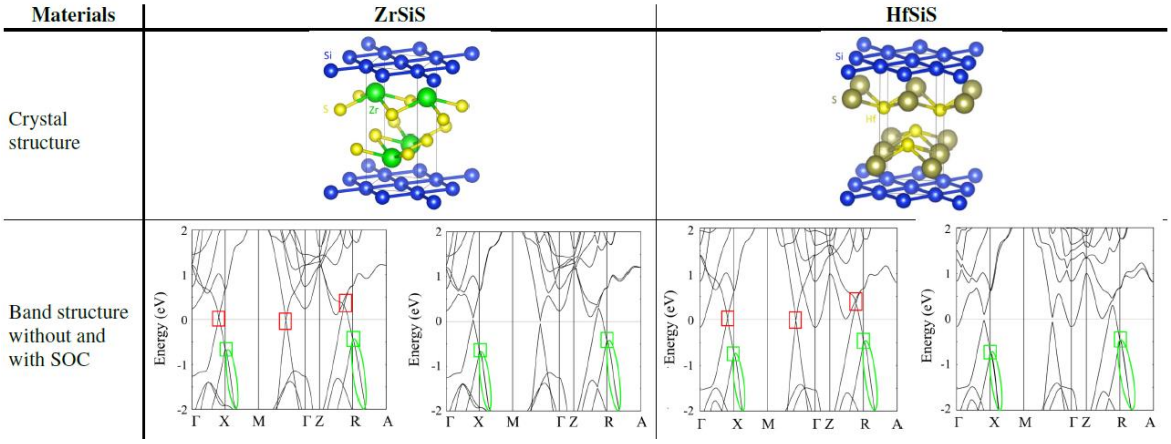

Fig. 2.16 Calculation of the band structures of ZrSiS and HfSiS. In the calculations, Dirac line nodes protected by non-symmorphic symmetry are indicated by green lines, while those not protected are indicated by red lines. Adapted from Ref 32.

Based on these evidences, my understanding of the issue is as following:

1. *M*SiS is a topological non-trivial system that contains topological non-trivial band structures. These would account for the topological non-trivial states observed. However, the topological non-trivial states do not locate at the high symmetry

directions protected by non-symmorphic symmetry. As a consequence, the SOC effect lifts the degeneracy of the Dirac point, preventing the formation of a topological Dirac line-nodes.

2. The Dirac line-nodes states studied in our system do not have a topological origin. The formation of Dirac line-nodes is merely a result of band folding at the boundary of the BZs caused by the non-symmorphic symmetry. Dirac line-nodes systems do not necessarily have to be related to topological states.

For the first point, more experiments should be carried out to examine the topological nature of those Dirac crossing. In a recent work from Ando's group, a suspicious Dirac crossing is observed at the M point in HfSiS, which is very similar to topological surface states[40]. Further experiments on n-doped samples can also be performed to directly visualize the electronic structures which are currently above the Fermi level in the pristine samples.

For the second point, as we have already known that certain crystal structures with non-symmorphic space group would lead to the formation of Dirac line-nodes states, we did find several examples in our recent studies, e.g. $TaSe_2$[41], InBi[34] and BiCuSeO (not published yet). We found very clear evidence of Dirac line-nodes at the predicted momentum positions in all these material systems, which were not discussed in detail here.

References

1 Hasan, M. Z. & Kane, C. L. Colloquium: Topological insulators. *Rev. Mod. Phys.* **82**, 3045-3067 (2010).

2 Qi, X. L. & Zhang, S. C. Topological insulators and superconductors. *Rev. Mod. Phys.* **83**, 1057 (2011).

3 Armitage, N. P., Mele, E. J. & Vishwanath, A. Weyl and Dirac semimetals in three-dimensional solids. *Rev. Mod. Phys.* **90**, 015001 (2018).

4 Moore, J. E. The birth of topological insulators. *Nature* **464**, 194-198, (2010).

5 Chen, Y. L. *et al.* Experimental Realization of a Three-Dimensional Topological Insulator, Bi_2Te_3. *Science* **325**, 178-181 (2009).

6 Chen, Y. L. *et al.* Massive Dirac Fermion on the Surface of a Magnetically Doped Topological Insulator. *Science* **329**, 659-662 (2010).

7 Young, S. M. *et al.* Dirac Semimetal in Three Dimensions. *Phys. Rev. Lett.* **108**, 140405 (2012).

8 Wang, Z. *et al.* Dirac semimetal and topological phase transitions in A_3Bi (A=*Na, K, Rb*). *Phys. Rev. B* **85**, 195320 (2012).

9 Xu, S. Y. *et al.* Observation of Fermi arc surface states in a topological metal. *Science* **347**, 294-298 (2015).

10 Wan, X., Turner, A. M., Vishwanath, A. & Savrasov, S. Y. Topological semimetal and Fermi-arc surface states in the electronic structure of pyrochlore iridates. *Phys. Rev. B* **83**, 205101 (2011).

11 Abrikosov, A. A. Quantum magnetoresistance. *Phys. Rev. B* **58**, 2788-2794 (1998).

12 Zhang, W. *et al.* Topological Aspect and Quantum Magnetoresistance of beta-Ag_2Te. *Phys. Rev. Lett.* **106**, 156808 (2011).

13 Liu, Z. K. *et al.* Discovery of a Three-Dimensional Topological Dirac Semimetal, Na_3Bi. *Science* **343**, 864-867 (2014).

14 Liu, Z. K. *et al.* A stable three-dimensional topological Dirac semimetal Cd_3As_2. *Nat. Mater.* **13**, 677-681 (2014).

15 Neupane, M. *et al.* Observation of a three-dimensional topological Dirac semimetal phase in high-mobility Cd_3As_2. *Nat. Commun.* **5**, 4786 (2014).

16 Xu, S.-Y. *et al.* Discovery of a Weyl fermion semimetal and topological Fermi arcs. *Science* **349**, 613-617 (2015).

17 Yang, L. X. *et al.* Weyl semimetal phase in the non-centrosymmetric compound TaAs. *Nat. Phys.* **11**, 728-732 (2015).

18 Liu, Z. K. *et al.* Evolution of the Fermi surface of Weyl semimetals in the transition metal pnictide family. *Nat. Mater.* **15**, 27, (2016).

19 Jiang, J. *et al.* Signature of type-II Weyl semimetal phase in $MoTe_2$. *Nat. Commun.* **8**, 13973 (2017).

20 Young, S. M. & Kane, C. L. Dirac Semimetals in Two Dimensions. *Phys. Rev. Lett.* **115**, 126803 (2015).

21 Ali, M. N. *et al.* Butterfly Magnetoresistance, Quasi-2D Dirac Fermi Surfaces, and a Topological Phase Transition in ZrSiS. *Sci. Adv.* ***2***, *e1601742* (2016).

22 Xu, Q. N. *et al.* Two-dimensional oxide topological insulator with iron-pnictide superconductor LiFeAs structure. *Phys. Rev. B* **92**, 205310 (2015).

23 Bian, G. *et al.* Topological nodal-line fermions in spin-orbit metal $PbTaSe_2$. *Nat. Commun.* **7**, 10556 (2016).

24 Wu, Y. *et al.* Dirac node arcs in $PtSn_4$. *Nat. Phys.* ***12***, 667 (2016).

25 Schoop, L. M. *et al.* Dirac cone protected by non-symmorphic symmetry and three-dimensional Dirac line node in ZrSiS. *Nat. Commun.* **7**, 11696 (2016).

26 Neupane, M. *et al.* Observation of topological nodal fermion semimetal phase in ZrSiS. *Phys. Rev. B* **93**, 201104 (2016).

27 Wang, X. F. *et al.* Evidence of Both Surface and Bulk Dirac Bands and Anisotropic Nonsaturating Magnetoresistance in ZrSiS. *Adv. Electron. Mater.* **2**, 10, 1600228 (2016).

28 Lou, R. *et al.* Emergence of topological bands on the surface of ZrSnTe crystal. *Phys. Rev. B* **93**, 241104 (2016).

29 Singha, R., Pariari, A. K., Satpati, B. & Mandal, P. Large nonsaturating magnetoresistance and signature of nondegenerate Dirac nodes in ZrSiS. *Proc. Natl. Acad. Sci. USA* **114**, 2468-2473, (2017).

30 Hu, J. *et al.* Evidence of Topological Nodal-Line Fermions in ZrSiSe and ZrSiTe. *Phys. Rev. Lett.* **117**, 016602 (2016).

31 Hu, J. *et al.* Evidence of Dirac cones with 3D character probed by dHvA oscillations in nodal-line semimetal ZrSiS. *arXiv:1604.01567* (2016).

32 Yang, S.-Y. *et al.* Symmetry demanded topological nodal-line materials. *Adv. Phys. X* **3,** 1414631 (2018).

33 Liang, Q. F., Zhou, J., Yu, R., Wang, Z. & Weng, H. M. Node-surface and node-line fermions from nonsymmorphic lattice symmetries. *Phys. Rev. B* **93**, 085427 (2016).

34 Ekahana, S. A. *et al.* Observation of nodal line in non-symmorphic topological semimetal InBi. *New. J. Phys.* **19**, 065007 (2017).

35 Strocov, V. N. Intrinsic accuracy in 3-dimensional photoemission band mapping. *J. Electron. Spectrosc. Relat. Phenom.* **130**, 65-78, (2003).

36 Hong, G. H. *et al.* Measurement of the bulk and surface bands in Dirac line-node semimetal ZrSiS. *Chinese Phys. B* **27**, 017105 (2018).

37 Hu, J. *et al.* Quantum oscillation studies of the topological semimetal candidate ZrGeM (M = S, Se, Te). *Phys. Rev. B* **95**, 205134 (2017).

38 Guan, S. *et al.* Two-dimensional spin-orbit Dirac point in monolayer HfGeTe. *Phy. Rev. Mater.* **1**, 054003 (2017).

39 Schoop, L. M. *et al.* Tunable Weyl and Dirac states in the nonsymmorphic compound CeSbTe. *Sci. Adv.* **4**, 2317 (2018).

40 Takane, D. *et al.* Dirac-node arc in the topological line-node semimetal HfSiS. *Phys. Rev. B* **94**, 121108 (2016).

41 Li, Y. W. *et al.* Folded superstructure and degeneracy-enhanced band gap in the weak-coupling charge density wave system 2H-$TaSe_2$. *Phys. Rev. B* **97**, 115118 (2018).

Chapter 3

Electronic Structure and Unusually Robust Bandgap in a High Mobility Layered Oxide Semiconductor Bi_2O_2Se

2D semiconductors with high carrier mobility and moderate band gap are particularly attractive for their potential broad applications in fast, low power consumption, and ultra-small/thin electronic devices. In this chapter, we will discuss our recent study on the electronic structure of a newly discovered air-stable oxide semiconductor Bi_2O_2Se. By combining the use of ARPES and STM, we mapped out its complete band and spatial structures. Moreover, surface patterns were found on the cleaved sample surface, which consists of 50% Se vacancies. Remarkably, we found no evidence of undesired in-gap states even in the presence of these surface defects, which proves Bi_2O_2Se to be an ideal semiconductor.

3.1 Background and Introduction

3.1.1 Introduction to two-dimensional materials

Semiconductors are important materials, forming the foundation of the Information Age that dramatically affects our everyday life. During last several decades, electronic devices based on traditional semiconductors (e.g. silicon and germanium) have already created a new civilization of human beings. The famous Moore's law represents the high-speed development of electronic industry, which claims that the number of transistors in the processor or overall processing powers of computers will be doubled every two years. To keep this trend, there are two methods in general: One is to shrink the geometrical dimensions while the other is to find alternative new materials with better electronic performance[1]. The first method has been very successful in improving the performance of devices over the last 60 years. However, it gradually reaches the limit due to the increasing difficulty in the fabrication of the smaller transistor. Therefore, the only way left to sustain the success of Moore's law is to find alternative materials with revolutionary new concepts.

The isolation of graphene monolayer in 2004 by the Geim's group in Manchester opens a new phase of 2D materials[2]. In the past decade, numerous 2D materials have been discovered and intensively investigated, such as graphene[2-4], transition metal dichalcogenides (TMDs)[1,5-9] and black phosphors[5,10,11]. Ultimate thin electronic devices have been fabricated by different 2D materials exhibiting extraordinary electronic properties. Therefore, considering the layered nature, easy accessibility, and great electronic properties, 2D materials have already become the most promising candidates to be the next generation of semiconductors.

Many pioneer researches have been done on 2D materials, among which graphene is the most widely studied. The graphene is a robust atomically thin 2D honeycomb like carbon

sheet with ultra-high carrier mobility (>10,000 $cm^2/V{\cdot}s$ at room temperature)[2,4]. However, the lack of a sizable bandgap (zero gap in single layer and very small gap for multilayer graphene)[12,13] limits its application in field effect devices. Small band gap would make it hard to switch the logic circuits between "on" and "off" status. Typically, a current on/off ratio between 1×10^4 and 1×10^7 with a band gap over 400 meV is needed for any material that owns ambitious to replace silicon in traditional electronic industry[1]. There are other 2D materials, for example few layers TMDs, which exhibit sizable bandgap. It has been well known that monolayer MoS_2, one of the most representative TMDs, has a 1.8 eV band gap[1,6-9]. The easy accessibility of large MoS_2 sheets, produced by either exfoliation or CVD growth method, makes it possible to be fabricated into electronic devices. The first transistor with single layer MoS_2 has been reported in 2011, which reveals great turn on/off ability (Fig. 3.1)[9]. Nonetheless, the carrier mobility of MoS_2 thin flakes is usually less than 100 $cm^2/V{\cdot}s$ at room temperature, which restricts its further potential as an electronic device. More recently, few-layer black phosphorus has emerged as a good 2D semiconductor candidate, with both appreciable thickness-dependent bandgap (0.3 ~ 2.0 eV from bulk to monolayer) and relatively high carrier mobility (~1000 at room temperature)[10]. Unfortunately, its metastability at ambient environment hinders the potentially broad application[14].

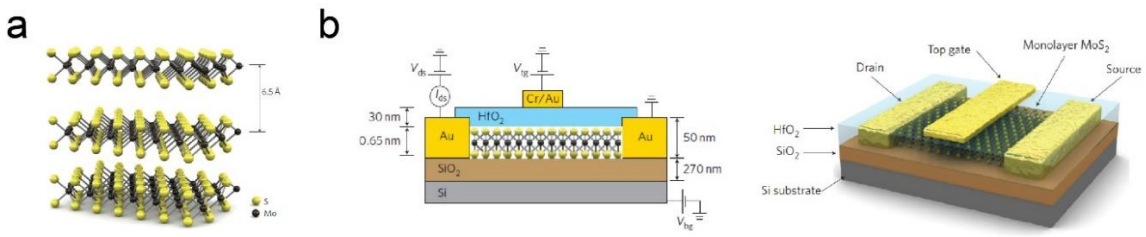

Fig. 3.1 MoS_2 and field effect transistor (FET). (a) Illustration of MoS_2 crystal structure. Monolayer MoS2 sheets can be obtained by using mechanical exfoliation method. (b) Monolayer MoS_2 sheet can be fabricated into FET devices, which exhibits good transport properties. Adapted from Ref. 9.

Although in recent years, researches have greatly improved the performance of electronic devices fabricated on the abovementioned 2D materials, it is still hard for any of those materials to substitute the traditional semiconductors in logic devices. Considering that, the search for new 2D candidates with excellent electronic performance, easy accessibility and stability in the ambient environment, still remains a very important and urgent topic in material researches.

3.1.2 Introduction to Bi_2O_2Se

Recently, Peng's group, our collaborator from Peking University, reported the superior transport properties of electronic devices fabricated on a bismuth-based oxychalcogenide 2D material, Bi_2O_2Se[15,16]. Compared with aforementioned 2D materials, Bi_2O_2Se appears to be a more promising 2D semiconductor candidate that can be broadly used in future electronic industry. The layered nature of Bi_2O_2Se makes it feasible to be fabricated into electronic devices down to few atomic layers, while the moderate band gap (~0.8 eV) and ultrahigh carrier mobility (~28,900 $cm^2/V{\cdot}s$ at 1.9 K) guarantee the extraordinary transport performance.

Most importantly, the air stability and easy accessibility (bulk crystal, few layers, and monolayer) of the material makes it ideal for future massive manufacturing in electronic industry.

As illustrated in Fig. 3.2(a), Bi_2O_2Se has a tetragonal crystal structure with I4/mmm space group. The planar covalently bonded $(Bi_2O_2)_n$ layers are sandwiched by square Se arrays with relatively weak electrostatic interactions. *Ab initio* calculation shows the existence of a moderate indirect band gap of ~0.85 eV (Fig. 3.2(b)), indicating its semiconducting nature. Single-crystalline Bi_2O_2Se thin film can be easily synthesized on mica through van der Waals epitaxy. Fig. 3.2(c) shows the optical image of the synthesized square Bi_2O_2Se sheets, with geometrical sizes more than 100 μm.

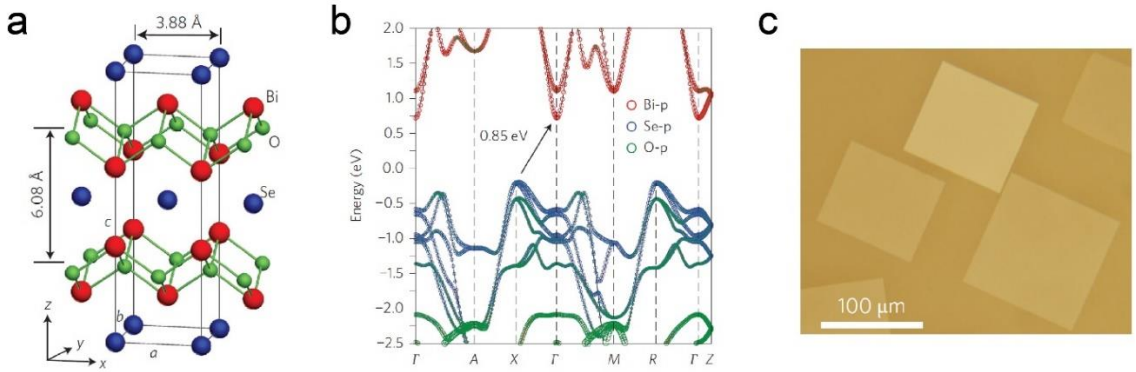

Fig. 3.2 Lattice and electronic structure of Bi_2O_2Se. (a) The layered crystal structure of Bi_2O_2Se with tetragonal $(Bi_2O_2)_n$ layers and Se_n layers alternately stacked along the c axis. (b) The calculated band structure and DOS of Bi_2O_2Se with a bandgap of ~0.85 eV. (c) A typical optical microscopy image of square Bi_2O_2Se nanoplates grown on mica. Adapted from Ref. 15.

High-quality Bi_2O_2Se flakes on mica were then fabricated into standard Hall-bar devices as illustrated in Fig. 3.3(a). The electron Hall mobility of the non-encapsulated Bi_2O_2Se flakes

reaches ~28,900 $cm^2/V{\cdot}s$ at 1.9 K (comparable to graphene) and ~450 $cm^2/V{\cdot}s$ at room temperature. Due to the long mean free path of the electrons with ultrahigh mobility, Shubnikov-de Haas (SdH) quantum oscillations are also observed in the measurement (Fig. 3.3(b)). By fitting the temperature dependence SdH oscillation amplitude, the cyclotron effective mass of the electron was estimated to be $(0.14 \pm 0.02)m_e$, which is consistent with theoretical calculation and ARPES experiment (discussed in section 3.2.3)

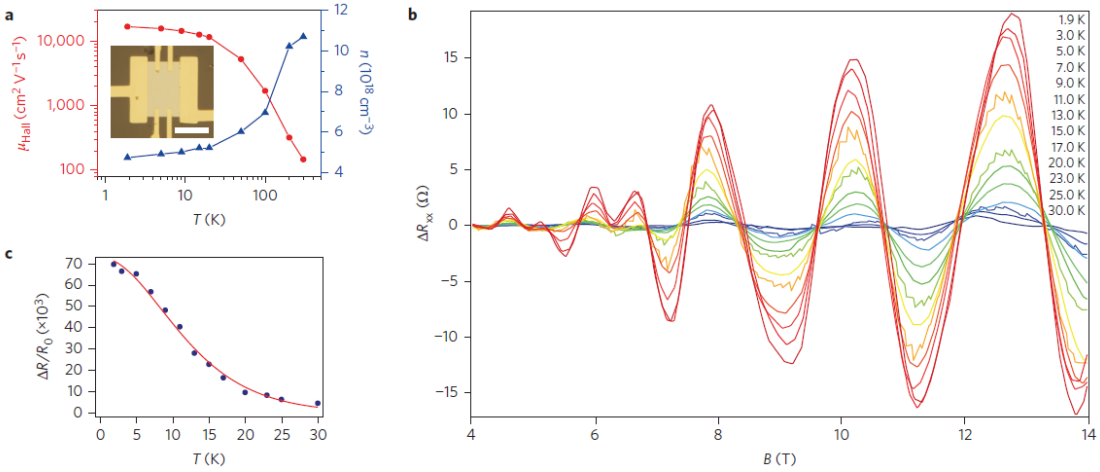

Fig. 3.3 Hall mobility and Shubnikov–de Haas (SdH) quantum oscillations in Bi_2O_2Se crystals. (a) Hall mobility (μ_{Hall}) and carrier density (n) as a function of temperature in a Bi_2O_2Se nanoplate. (b) The SdH oscillatory part of the longitudinal magnetoresistance ΔR_{xx} as a function of the applied perpendicular magnetic field measured in the temperature range from 1.9 to 30 K. (c) Temperature dependent $\Delta R/R_0$ values of the SdH oscillations and the Lifshitz-Kosevich fitting at 12.8T, giving a low cyclotron in-plane effective mass of $0.14 \pm 0.02)m_e$. Adapted from Ref. 15.

Such excellent electronic behaviors motivate the fabrication of FET devices based on high-quality Bi_2O_2Se thin flakes. As illustrated in Fig. 3.4(a), top-gated Bi_2O_2Se FET device was fabricated, with HfO_2 dielectric layer and Pd/Au metal electrodes. The device exhibits a

very high on/off ratio of ~10^6 at room temperature, which significantly exceeds the requirement of logic transistors (~10^4).

From all the above investigation, we can conclude that Bi_2O_2Se, an air-stable layered oxide, emerges as a promising new semiconductor with excellent electronic properties. The high carrier mobility, high current on/off ratio, moderate band gap together with air stability make it a rare promising 2D material candidate for the future electronics.

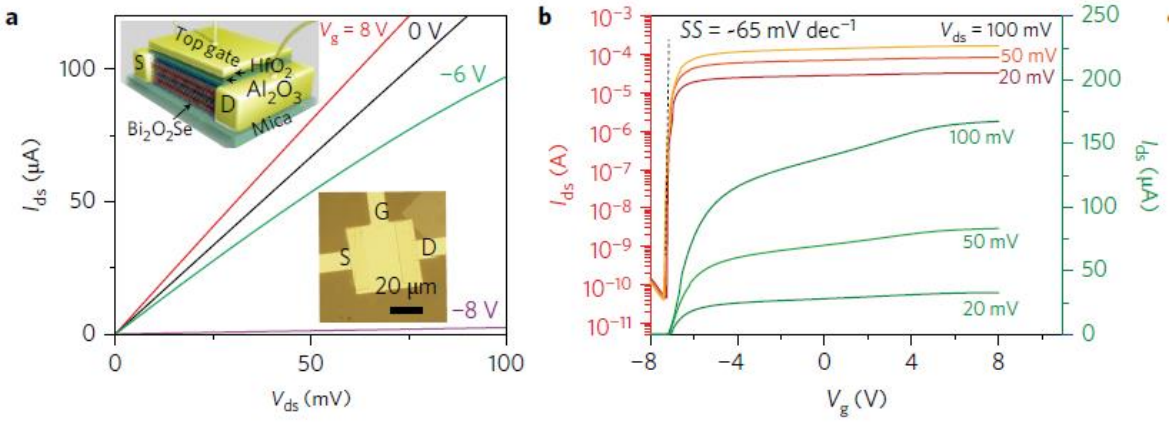

Fig. 3.4 Room temperature measurement of Bi_2O_2Se-channel FET devices. (a) Output curves obtained from a 6.2-nm-thick Bi_2O_2Se device a room temperature. Inset: schematic and optical microscopy image of the top-gated Bi_2O_2Se FET. (b) Top-gate transfer curves (I_{ds}-V_g) of the device with different source-drain voltages (100, 50, 20 mV), exhibiting a large on/off ratio of 10^6. Adapted from Ref. 15.

Besides its potential in electronic applications, Bi_2O_2Se is also a thermoelectric material[17] with the thermoelectric figure-of-merit *ZT* predicted as high as 1.42 (comparable to Bi_2Te_3, the best thermoelectric materials broadly used nowadays) if an in-plane strain is applied[18]. Moreover, as the Bi-O layer in Bi_2O_2Se is structurally compatible with many perovskite oxides that exhibiting rich and interesting physical phenomena (e.g.

ferroelectricity, magnetism, multiferroics and high-T_c superconductivity), it is possible to fabricate hybrid structures/superlattices between Bi_2O_2Se and various perovskite oxides (e.g. $Bi_2Sr_2Ca_{n-1}Cu_nO_{2n+4+x}$ series high-temperature superconductors, $SrTiO_3$, etc.) to pursue novel emergent physical phenomena in hybrid semiconductor-superconductor hybrid systems[19-23].

To realize the full potential of Bi_2O_2Se and explore its applications in electronic, thermoelectric and optoelectronic devices, a comprehensive understanding of its detailed electronic structures is essential. For this purpose, we combined the use of two experimental tools: angle-resolved photoemission spectroscopy (ARPES) and scanning tunneling microscopy (STM) to systematically map out the detailed band structure of Bi_2O_2Se. The cleavage surface of the crystal was revealed to possess intertwined weave pattern formed by Se atoms and vacancies. Surprisingly, all these Se vacancies would still retain the cleanness of the bandgap without introducing any undesired in-gap surface/edge states. And this makes Bi_2O_2Se an ideal semiconductor for future electronic applications.

3.2 Electronic structure of Bi_2O_2Se

3.2.1 Basic characterizations on Bi_2O_2Se single crystal

In our study, high-quality bulk Bi_2O_2Se single crystals were synthesized in a modified Bridgman method by Peng's group. High-resolution X-ray diffraction (XRD) was performed on the single crystal and diffraction patterns from different surfaces are shown in Fig. 3.5(a). Core level photoemission spectra (Fig. 3.4(b)) clearly shows the characteristic double peak of both Se 3*d* and Bi 5*d* orbitals, indicating the excellent quality of crystals.

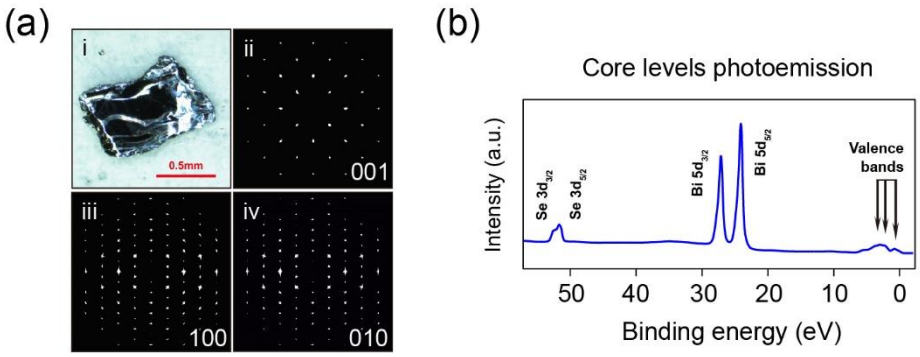

Fig. 3.5 XRD and photoemission spectrum of Bi_2O_2Se bulk single crystals. (a) (i) Image of a Bi_2O_2Se single crystal. (ii-iv) XRD pattern of the (001), (100) and (010) surface of Bi_2O_2Se. (b) Core-level photoemission spectrum, clearly showing the characteristic double peaks of Bi and Se.

The single crystal was then mounted into standard Hall-bar-like devices, which exhibits a very high residual-resistance ratio (RRR, $R_{xx,\,300\,K}/R_{xx,\,2\,K}$) of 585 (Fig. 3.6(a)). Ultra-high Hall mobility of 2.8×10^5 $cm^2/V{\cdot}s$ at 2.0 K was reached as shown in Fig 3.6(b). Shubnikov-de Haas (SdH) quantum oscillations are also observed at low temperature (Fig. 3.6(c)), indicating the long mean free path of the ultrahigh-mobility carriers. Temperature-dependent $\Delta R/R_0$ values of the SdH oscillations and the Lifshitz–Kosevich fitting give a low in-plane cyclotron effective mass m^* of ~0.16 m_e (Fig. 3.6(d)). These transport results illustrate the superior electronic properties of the material and also prove the good quality of our bulk Bi_2O_2Se single crystals.

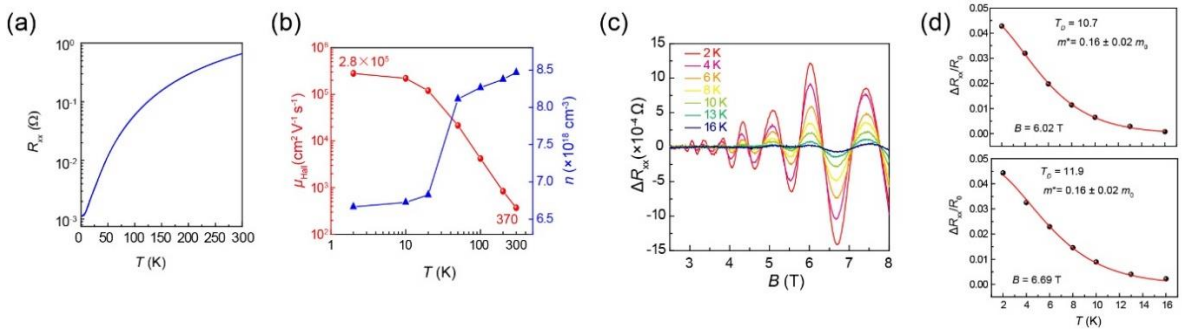

Fig. 3.6 Transport properties of bulk Bi_2O_2Se single crystal. (a) Resistance as a function of temperature, exhibiting a very high residual-resistance ratio (RRR, $R_{xx,\,300\,K}/R_{xx,\,2K}$) of 585. (b) Hall mobility (μ_{hall}) and carrier density (n) as a function of temperature in Bi_2O_2Se single crystal. The Hall mobility reaches ~2.8×10^5 $cm^2/V{\cdot}s$ at 1.9 K, and 370 $cm^2/V{\cdot}s$ at room temperature. (c) SdH oscillatory part of the longitudinal magnetoresistance as a function of applied perpendicular magnetic field. The non-oscillatory part was removed. (d) Oscillation amplitude $\Delta R_{xx}/R_0$ as a function of temperature T using the Lifshitz-Kosevich formula fitting at 6.02 T and 6.69 T, respectively.

3.2.2 General electronic structure

To reveal the detailed band structure of Bi_2O_2Se bulk crystal, we carried out ARPES experiment at I05 beamline of Diamond Light Source (DLS, UK). The high-quality single crystals were transferred into the UHV chambers and cleaved inside to expose fresh surface. Due to the weak interaction between Bi_2O_2 and Se layers as well as the strong in-plane bonding within the Bi_2O_2 layers, the cleavage of crystal tends to occur between two Bi_2O_2 layers, as illustrated in Fig. 3.7(a). The layered nature of the crystal results in flat cleavage plane which is ideal for ARPES measurement. Figure 3.7 (b) shows the related BZ of the I4/mmm tetragonal crystal structure with high symmetry points labeled. Large-scale energy contours of both conduction band minimum (CBM) (around 0.15 eV below Fermi level) and valence band maximum (VBM) (around the binding energy of 0.85 eV) are illustrated in Fig

3.7 (c) (a photon energy of 98eV was used to measure the Γ – X – M plane), which matches well with the BZs (blue lines). As the CBM locates at the Γ point while the VBM at the X point, an indirect bandgap of ~0.8 eV is formed. The high symmetry cut along X – Γ – X direction and related density of state (DOS) (Fig. 3.7(d)) clearly illustrates the clean indirect band gap, which is consistent with the *ab initio* calculation attached below. The calculation was performed by our collaborator Binghai Yan's group using the same method as discussed in chapter 2 (section 2.2.1).

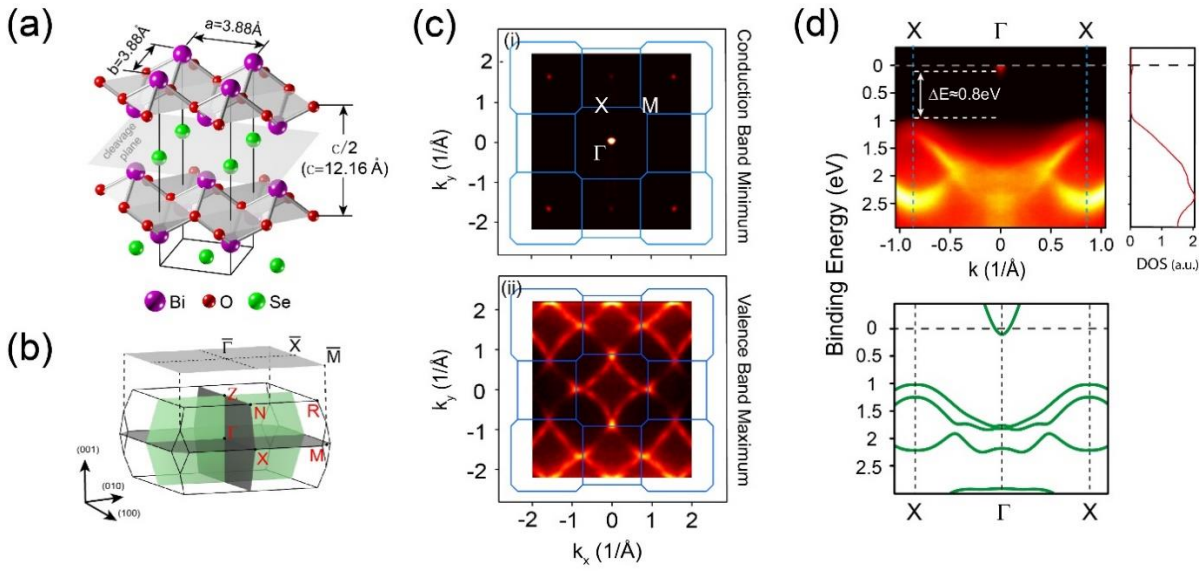

Fig. 3.7 General band structure of bulk Bi_2O_2Se single crystal. (a) Illustration of the crystal structure of Bi_2O_2Se, indicating the cleavage plane. (b) Schematic of the bulk BZ and surface projection. (c) Constant energy cut of Bi_2O_2Se at CBM and VBM. Blue grids indicate the BZ. (d) High symmetry cut along Γ-X direction and related DOS, showing the clean indirect band gap around 0.8eV, consistent with *ab initio* calculation.

However, the $k_x – k_y$ map above cannot prove that the band gap is really located along X – Γ – X direction. Since there is another degree of freedom in the 3D momentum space, which is the k_z. In our ARPES experiment, changing the energy of incident photons provides

us the ability to access band structure with different k_z. Therefore, to examine the band evolution along k_z direction, we performed the photon energy dependent experiment. The inner potential V_0 was determined according to the band periodicity along k_z direction, same as the procedure discussed previously in *M*SiS materials (Section 2.2.4)[24,25]. Therefore, in the following, we will directly go to the result while skipping the detailed analysis.

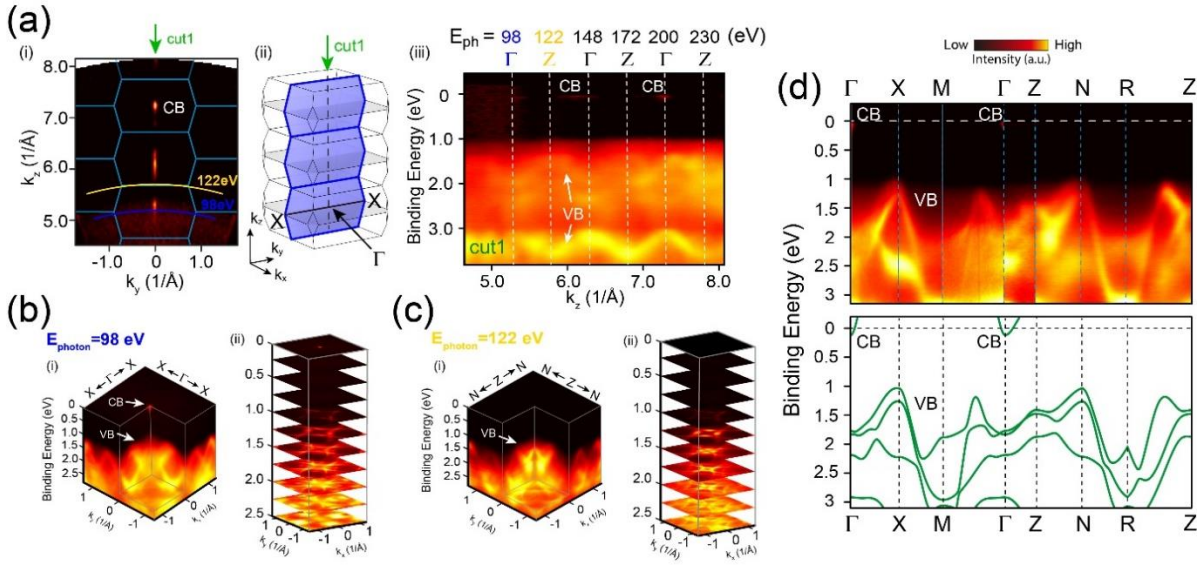

Fig. 3.8 Photon energy-dependence ARPES experiment on Bi_2O_2Se. (a) (i) Plot of the photoemission intensity at fermi surface (FS) on k_y-k_z plane. The FS contains a stretched-dot-like dispersion of conduction band, showing at Γ and missing at Z points. (ii) Schematic of BZ along k_z direction. Blue plane indicates the k_y-k_z plane in (i). (iii) Band dispersion along Γ–Z direction. Clear periodicity can be observed through wave-like valance bands. High symmetry points and related photon energies are marked above. (b) (i) 3D intensity plot of the photoemission spectra for 98 eV photons that cut through Γ ($k_z = 0$ plane). (ii) Slice plot of constant energy contours at different binding energy, showing the band evolution and the indirect bandgap. (c) Same as (b) with a photon energy of 122 eV that cuts through Z ($k_z = \pi/c$ plane). (d) General band evolution among high symmetry points, showing excellent agreement with theoretical calculation.

Figure 3.8(a)(i) shows the Fermi surface map of the k_y - k_z plane from the photon energy dependence experiment. It confirms the existence of the only electron pocket, appearing at Γ and missing at Z point. The band dispersions along Γ-Z direction (Fig 3.8(a)(iii)) clearly demonstrates the periodicity along k_z direction. High symmetry points are labeled above the figure with the related accessing photon energies. By fixing the incident photon energy at 98 eV and 122 eV, we are able to systematically map out the electronic structure of Bi_2O_2Se bulk crystal at Γ ($k_z = 0$) and Z ($k_z = \pi/c$) planes respectively. Detailed evolution of the band structure with binding energy is shown in Fig 3.8(b-c), which will be important for the understanding of the physical properties of Bi_2O_2Se (and its devices) at different doping levels. In addition, band dispersions of Bi_2O_2Se among all high symmetry points are exhibited in Fig. 3.8(d), showing very good consistency with calculation.

3.2.3 Electron and hole pockets

After establishing the overall band structure of Bi_2O_2Se, we now focus on the details of the FS pockets near the CBM and VBM, which dominate the transport properties for n- and p-type Bi_2O_2Se, respectively. As the Fermi-level of the as-grown sample is too close to the CBM which makes resolving the band dispersion difficult, we used the *in situ* potassium dozer equipped at the beamline to introduce the electron doping. Figure 3.9(a) illustrates the process of the potassium dosing as well as the core level photoemission curves before and after dosing. The appearance of extra potassium peak indicates the attachment of the potassium atoms onto the surface of Bi_2O_2Se. In the end, we successfully shifted the Fermi-level up by ~160 meV as illustrated in Fig. 3.9(b), without an obvious change of the band dispersions of Bi_2O_2Se. Therefore we were able to acquire the detailed dispersion of the parabolic electron pocket, as shown in Fig. 3.9(c) (dispersions) and Fig. 3.9(d) (stacking-plot

of constant energy contours). Combining the dispersions and the FS on k_x-k_y and k_y-k_z planes, the electron pocket shows an ellipsoidal shape (Fig. 3.9(e)), which is consistent with the calculation of the FS in momentum space (Fig. 3.9(f)).

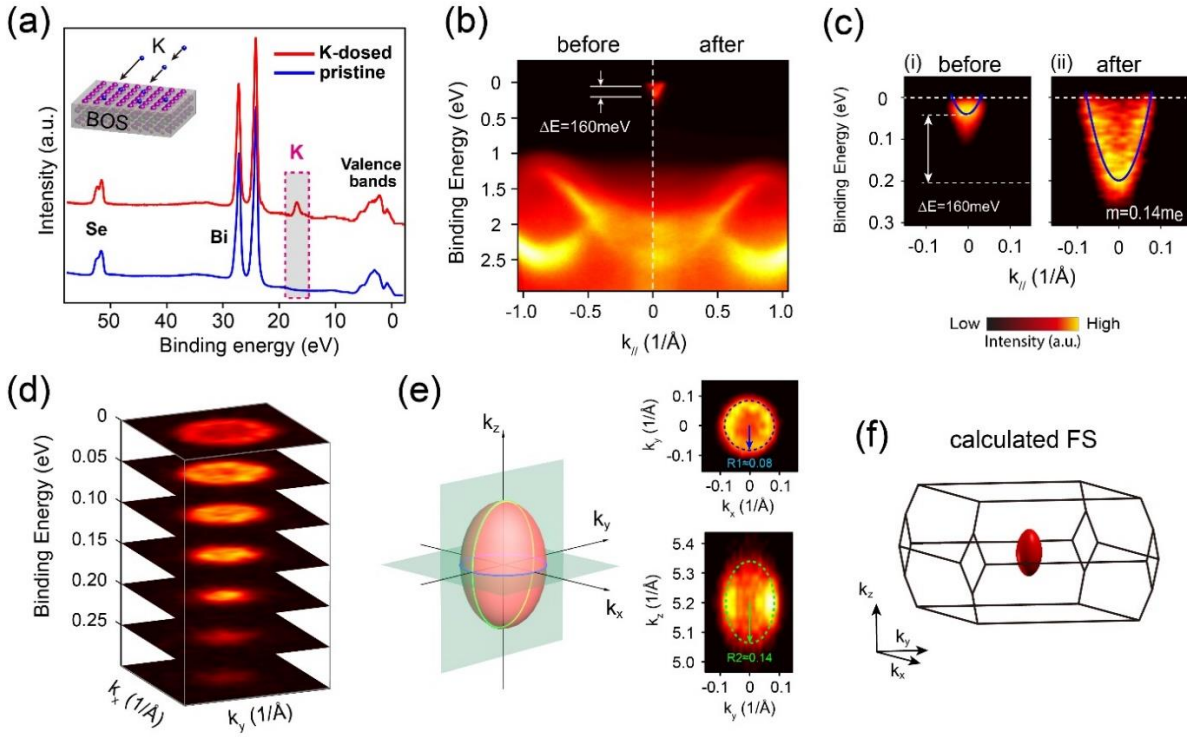

Fig. 3.9 Detailed structure of conduction band. (a) Core-level intensity spectrums before and after potassium dosing, showing the appearance of the characteristic peak of potassium. Inset: Illustration of dosing process. (b) Photoemission intensity plots of dispersions along Γ-X direction before and after dosing. Fermi energy (E_f) was lifted up by 160 meV, without changing general band structure. (c) Spectra of conduction band before and after dosing, showing a parabolic shape, with a small in-plane effective mass of $(0.14 \pm 0.02)m_e$. (d) Stacking plot of constant energy maps of the conduction band. (e) Photoemission intensity plots of FS on k_x-k_y and k_y-k_z plane, respectively. Conduction band was reconstructed to be an ellipsoid in 3d k-space. (f) Calculated FS, consistent with experiment result.

Furthermore, with detailed analysis, we are able to fit the dispersion of the pockets to deduce important parameters (e.g. effective mass, Fermi velocity), which are important to the transport properties of n- and p-type Bi_2O_2Se. As illustrated in Fig. 3.10(a), the dispersion of electron pocket was extracted by finding the peak positions from energy distribution curve (EDC), which was then fitted by a parabolic model $\boldsymbol{E = \frac{\hbar^2(k-k_0)^2}{2m^*} + E_0}$ (k_0 and E_0 are the relative momentum and binding energy with reference to the bottom of the conduction or the top of the valence band). The in-plane effective mass of electron $\boldsymbol{m^*}$ is estimated to be $\boldsymbol{(0.14\pm0.02)\ m_e}$ (m_e is the mass of a free electron), which is consistent with both calculation and transport experiment presented above. The related Fermi velocity is calculated as:

$$\boldsymbol{v_F = \sqrt{\frac{2|E-E_0|}{m^*}} = (3.78 \pm 0.01) \times 10^6 \sqrt{|E-E_0|(\mathrm{eV})}\,\mathrm{m/s}}$$

Similarly, as illustrated in Fig. 3.10**(**b**)**, the effective mass of hole pockets can also be determined. Since there are two hole pockets around X point, the EDCs are fitted using two Lorentz peaks. From the fitting result of the upper hole pocket, the in-plane effective mass is estimated to be $(-2.41\pm0.02)\ m_e$ along X–Γ direction, as well as $(-0.30\pm0.02)\ m_e$ along X–M direction.

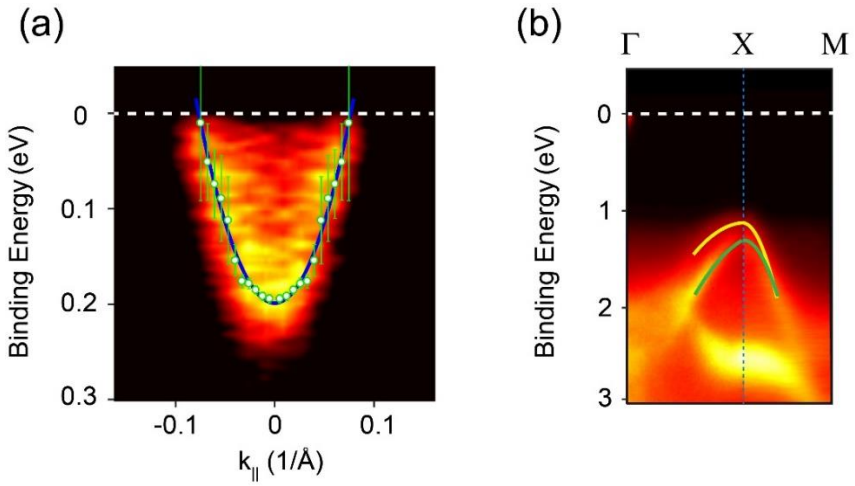

Fig. 3.10 Fitting of electron and hole pockets. (a) Photoemission spectrum of electron pocket located around Γ point as well as the fitting result. Green dots mark the peak positions of each EDC, while the blue solid line indicates the parabolic fitting result of these peak positions. (b) Photoemission spectrum of hole pockets around X point and related fitting result, using the same fitting process as described in (a).

Up until now, we have systematically revealed the general electronic structure of Bi_2O_2Se bulk crystal. The calculated indirect band gap was clearly observed in our spectra, while the photon energy dependent experiment confirms its location in 3D momentum space. Particularly, in our ARPES experiment, we found no evidence for the existence of any undesired in-gap states, which will be harmful to the potential industrial application of Bi_2O_2Se devices[26,27]. In addition, electron and hole pockets have been analyzed in detail. All the parameters deduced together with the band dispersions illustrated in our spectra will be a very important reference for the future research or application of this material.

3.3 STM study on cleaved surface

3.3.1 Formation of surface pattern

In the ARPES experiment above, the detected signal averages from the whole beam spot, with the size over tens of microns. Therefore, to study the local electronic structure, especially the formation of surface defects and its influence, further STM experiment has been carried out on the cleaved Bi_2O_2Se surface (experiment was done by Meixiao Wang, in Shanghai Tech University).

The STM experiments were carried out in UHV environment. Bi_2O_2Se single crystals were glued onto highly doped silicon wafers and cleaved in situ at room temperature. Cleaved samples were transferred to a cryogenic stage kept at 77 K for STM experiments. Chemically etched tungsten (W) tips were used for both imaging and tunneling spectroscopy. The tungsten tip is calibrated with the surface states of silver islands on Si(111)-7×7. Lock-in technique was employed to obtain dI/dV curves. A 5 mV modulation signal at 991 Hz was applied to the sample together with the DC sample bias.

As mentioned previously, the weak interaction between Bi_2O_2 and Se layers leads to a cleavage between two Bi_2O_2 layers. Therefore, considering the equivalency of the upper and bottom Bi_2O_2 layers, half Se atoms are supposed to be cleaved away while the other half remain on the cleavage surface (demonstrated in Fig. 3.11(a)). As a consequence, the cleavage will result in a half-Se cleavage surface, which sounds very reasonable considering the requirement of charge balance. To further enrich our assumption, we carried out *ab initio* calculation in terms of the formation energies of different cleavage surfaces. Our result indicates that the half-Se cleavage surface is indeed more energy favorable compared to full-Se or Bi cleavage surface. In addition, as no evidence of extra periodicity was observed in

our ARPES measurement, we assume that the Se atoms remained on the surface should be randomly distributed.

Now, we are very curious about what kind of surface pattern will be formed and what kind of influence it will generate on the electronic structure of Bi_2O_2Se. In general, the appearance of vacancies on the surface of semiconductor materials often leads to undesired surface or edge states which is harmful to the broad application in industry. Therefore, we wonder if the similar situation appears in the case of Bi_2O_2Se. To answer all these questions, we performed systematical STM and scanning tunneling spectroscopy (STS) experiments on the cleaved Bi_2O_2Se surface.

Large area STM image on the cleaved surface is illustrated in Fig. 3.11(b). The layered nature of Bi_2O_2Se is clearly presented by the large terraces with the step height of ~0.61 nm, which is exactly the length of c/2. Furthermore, we zoomed into one of the step edges to obtain some detailed information. As demonstrated in Fig 3.11(c), both the lower and upper layers contain the same weave pattern formed by the line-shape Se vacancies, constituting of ~50% of the total surface area (by counting the dominance rate of Se atoms from all STM images, some of which are not shown here). From the STM image with atomic resolution, the bright Se atoms as well as the dark Se vacancies can be easily distinguished. The distance between two Se atoms is measured to be around 0.39 nm, matching well with lattice constant. Therefore, we have confirmed that the cleaved surface of bulk Bi_2O_2Se crystal is indeed a half-Se cleavage surface as expected.

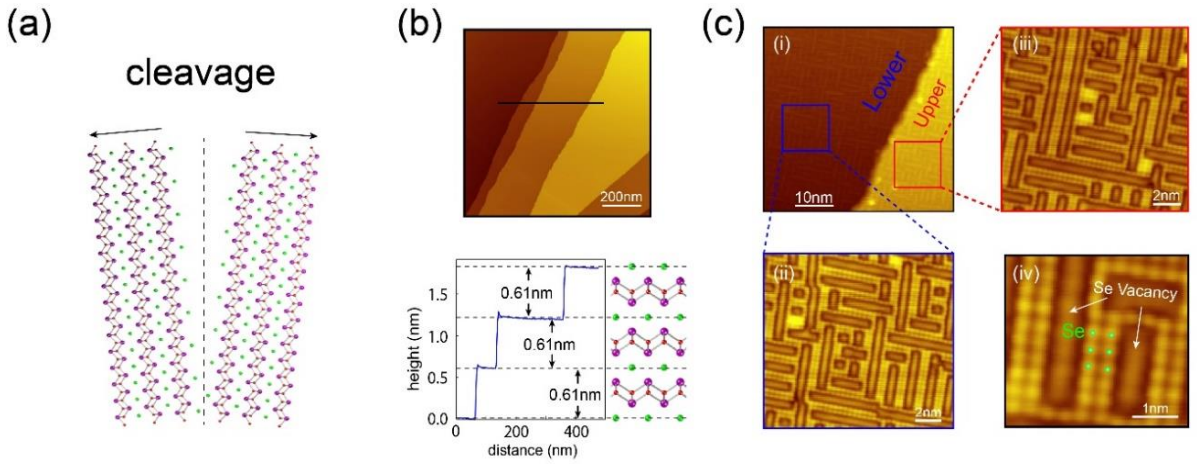

Fig. 3.11 Surface morphology of cleaved Bi_2O_2Se crystals. (a) Illustration of the cleavage process, due to the equivalency of the upper and bottom (Bi_2O_2) layers, half Se atoms are cleaved away while the other half remains. (b) Large-scale STM image of the cleaved Bi_2O_2Se surface. Step edges of ~0.61 nm are indicated. (c) (i) STM image around the step edge. (ii-iii) Zoomed-in details on both lower and upper layers respectively, showing uniform intertwined weave patterns formed on half-Se cleavage plane. (iv) Further zoomed-in image with atomic resolution, clearly illustrates the Se atoms and Se vacancies.

3.3.2 Dimer configuration

To further understand the formation of surface patterns, detailed analysis was performed on our data. As illustrated in Fig. 3.12(a), a Fast Fourier Transform (FFT) was carried out on a large scale STM image. The brightest spots on the image indicate a period of 4×Se-Se atomic distance, along both X and Y directions. This is caused by the fact that both Se atoms and the vacancies dimerize and form 2×n structures, as can be seen from the STM images with atomic resolution (Fig. 3.12(b)). The dimerized Se atoms and vacancies (which is the dimerized Se atoms on the other half of cleaved sample) then form the period along both X and Y directions, agreeing well with FFT result.

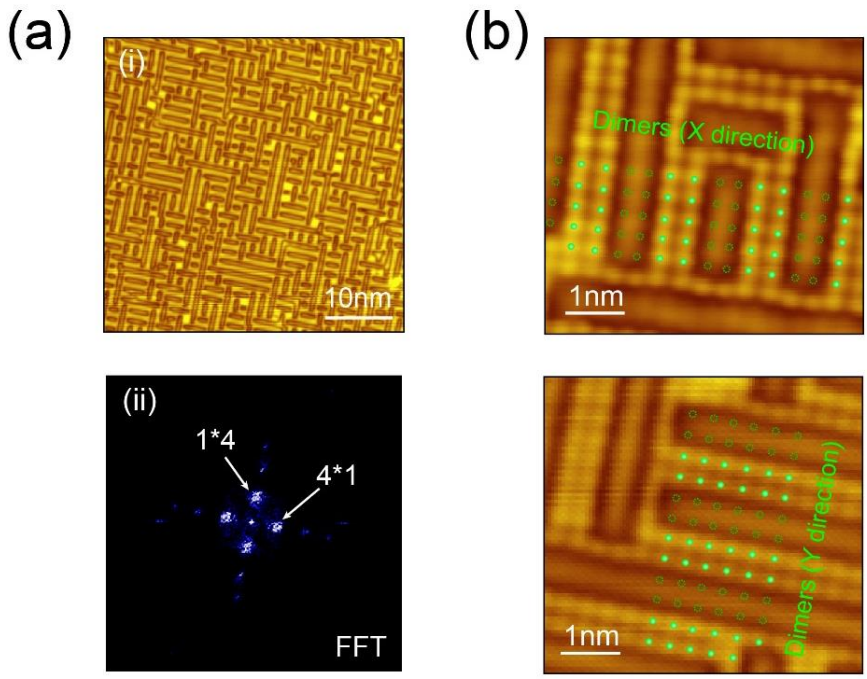

Fig. 3.12 Detailed surface structure and energy calculation. (a) (i) STM image of the cleaved Bi_2O_2Se surface. (ii) FFT indicated a periodicity with the size of 4 atoms. (b) Atomically resolved STM image shows that Se atoms and vacancies tend to appear in the form of dimers.

To understand these results, we carried out *ab-initio* calculation to estimate the formation energy of different Se-atom and vacancy configurations. Slab model (calculation performed by Gang Li from Shanghai Tech University) is used as illustrated in Fig. 3.13(a). Considering the 4-fold symmetry of the crystal, only one direction is considered here, (the configuration is simply extended along the other direction). The formation energy was calculated as following:

$$E_c = (E_{Se-atom\ chain+substrate} - E_{substrate})/N_{Se}$$

As expected, the configuration with Se-Se dimer and vacancy on each side (vacancy dimer) does show the lowest formation energy (most favorable), as illustrated in Fig. 3.13(b).

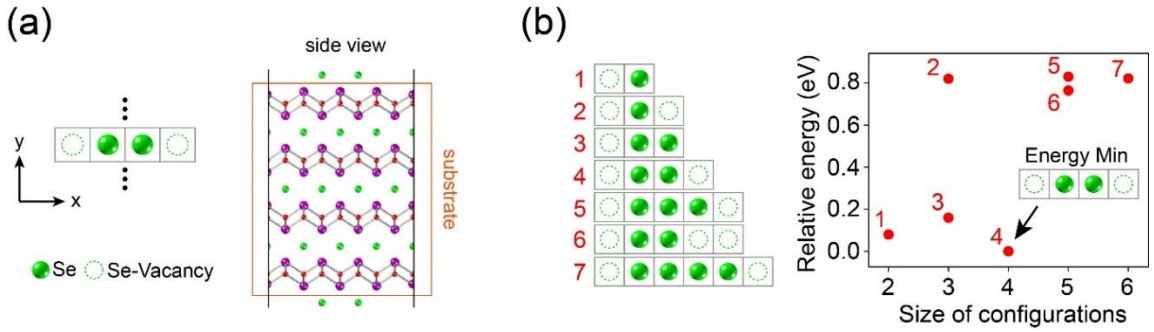

Fig. 3.13 Calculation of the formation energy of different configurations. (a) Slab model used for the calculation. (b) Calculated formation energies for different configurations. Se-Se dimer with vacancy on each side is most energy favorable.

3.3.3 Monte Carlo simulation

Since no evidence of extra periodicity is observed in our APRES experiment, we suspect that the dimerized Se atoms and vacancies on the cleaved surface are randomly distributed without the formation of higher order periodicity. To simulate this random distribution, we used the 'tile model' in Monte Carlo simulation (performed by my colleague Han Peng). Considering the equivalency of the x and y direction, the Se-Se dimer configuration discussed above was extended to form 4 × 4 building blocks for the simulation, as shown in Fig. 3.14(a). The Monte Carlo simulation shows a very similar surface pattern and FFT result to the real situation (comparing Fig 3.14(a) with Fig 3.12(a)). In addition, to prove the accuracy of our simulation, the quantitative comparison was made by counting the length of the vacancy dimers. The statistical results of both real image and the simulated image are demonstrated in Fig 3.14(b), which shows great consistency. Our result indicates that the

dimerized Se atoms and vacancies are indeed randomly distributed on the cleaved surface and the surface pattern can be easily simulated by very simple model.

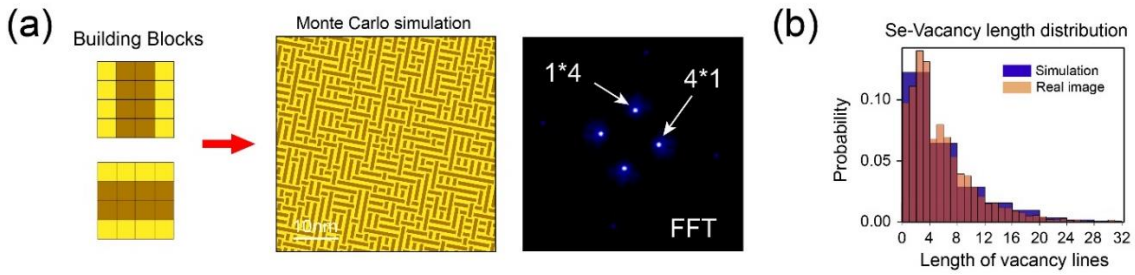

Fig. 3.14 Monte Carlo simulation of the surface pattern. (a) Monte Carlo simulation of the surface with the dimer configuration. The simulated patterns agree well with the real situation. (b) The statistical result on the probability of the length Se-vacancy chain, indicating the accuracy of the simulation.

3.3.4 Influence on the electronic structure

After understanding the formation of the surface pattern, our next question is whether this pattern will introduce any undesired surface or edge states. To find the answer, STS experiments were performed on special points of the cleaved surface. As illustrated in Fig. 3.15(a), STS spectra were taken at points both away from the step edge (point P1, P2) and in the vicinity of the step edge (point P3, P4). The dI/dV spectra from all four measurements clearly show the bulk band gap (~0.85 eV) without in-gap surface or edge states. In addition, the dI/dV spectra at 16 data points along a certain line on the surface (Fig. 3.15(b)) further confirm the uniformity of the band gap. Therefore, we conclude that the cleanness of the indirect band gap is preserved even in the presence of surface Se vacancies discussed above.

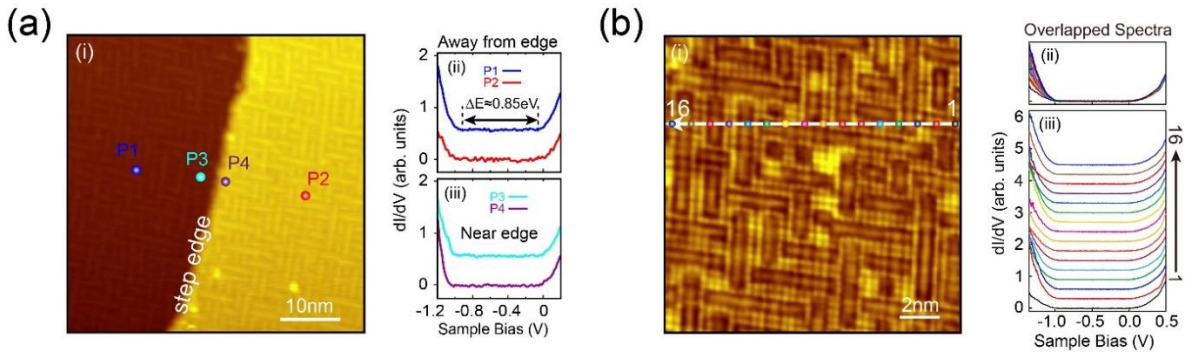

Fig. 3.15 Uniform clean band gap of Bi_2O_2Se. (a) STS spectra taken around and away from step edge, indicating a ~0.85 eV band gap free from the undesired surface or edge states. (b) STS spectra taken at 16 data points on the line indicated in the STM image, showing the uniformity of the clean band gap.

The cleanliness of the band gap is very important for the broad application of Bi_2Se_2O in industry, which will maintain its high transport behaviors. However, generally, the surface vacancy or reconstruction often introduce extra electronic states to the system. Therefore, it is actually a very interesting question that weather the pattern formed on the half-Se cleavage surface discussed above has any influence on the electronic structure of Bi_2Se_2O.

To understand the issue, slab model was used again to calculate the contribution of both Se-top atoms and Bi-top atoms (Se vacancies) to the DOS[28,29]. The result (illustrated in Fig 3.16(b)) indicates that the Se-top atoms and Bi-top atoms on the surface do introduce some extra states, however, only affects the electronic structure in conduction and valence bands. As a consequence, the cleanness of the band gap is guaranteed. The Se vacancies (electron donor) here do not form localized band inside the band gap, therefore cannot trap any electrons. In other word, Bi_2O_2Se will keep its high electronic performance even in the presence of surface vacancies. To verify that, STS experiments were performed precisely on

Se atoms and in the vacancies (Fig. 3.16(c)). And both the conduction and valence density of states show very good agreement with our calculation. During the experiment, we found that the large bias leads to the shift of Se atoms, therefore, the experiments for conduction and valence band can only be conducted separately.

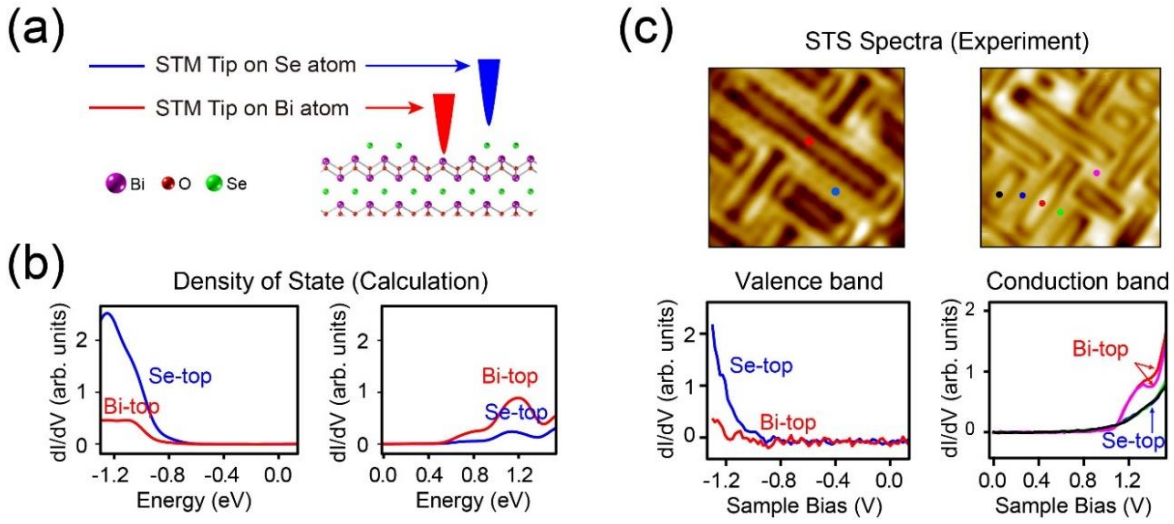

Fig. 3.16 Influence of surface pattern on the electronic structure of Bi_2O_2Se. (a) Illustration of STS measurements on Bi-top atoms and Se-top atoms. (b) Contribution of Bi-top atoms and Se-top atoms to the Density of States, in consistent with experiment. (c) STS spectra for both conduction and valence band respectively, indicating the non-existence of in-gap surface state introduced by Se-Se dimers and vacancies.

In conclusion, by performing STM experiments, we clearly observed the formation of surface pattern on the cleaved Bi_2O_2Se. Se atoms and vacancies are found to be dimerized and randomly distributed on the surface, which is theoretically explained from the energy aspect. A simple Monte Carlo model can easily simulate the formation of surface pattern, while the detailed STS experiments confirm that the surface vacancies will not introduce any

undesired in-gap states. Therefore, our experimental results suggest Bi_2O_2Se to be a robust 2D semiconductor material that can be used in future electronic industry.

3.4 Discussions and Perspectives

The spatial uniformity of the moderate band gap without undesired surface/edge states, together with its small carrier effective mass, layered nature and air stability makes Bi_2O_2Se an ideal semiconductor for future electronic applications. In this work, we systematically illustrated the electronic structure of Bi_2O_2Se and simulated its half-Se-coverage cleavage surface with simple models. The result not only deepens our understanding of this special material but also motivate the future study on the Bi_2O_2X (X = S, Se, Te) family of semiconductors.

In addition to the numerous advantages in the semiconductor field, Bi_2O_2Se also has great potential in fundamental research. As examples, the Bi-layer in Bi_2O_2Se forms a 2D square lattice with the Bi-Bi distance as 3.88Å, identical to that in the $Bi_2Sr_2Ca_{n-1}Cu_nO_{2n+4+x}$ series of unconventional high transition temperature superconductors (HTSC); and Bi_2O_2Se is also lattice matched with the commonly used substrate $SrTiO_3$ (cubic phase, lattice constant 3.9 Å). These structural compatibilities make it possible for the fabrication of semiconductor-HTSC hybrid junctions and novel interface 2D electron gas, thus opening the door for the study of numerous novel phenomena, such as topological superconductivity[19], Josephson junction field effect transistor[20], new superconducting optoelectronics[21,22] and novel lasers[23].

Based on the above discussion, further researches will be carried out on the material. As illustrated in Fig. 3.17, Bi_2O_2Se flakes were already successfully synthesized on both

Bi2212 superconductor and $SrTiO_3$ substrate (though the quality and size of the sample should be further improved). Currently, we are performing both transport measurement and Spatially resolved ARPES experiment (due to limited sample sizes) on the samples and we hope to get more exciting fundamental breakthroughs on this material system.

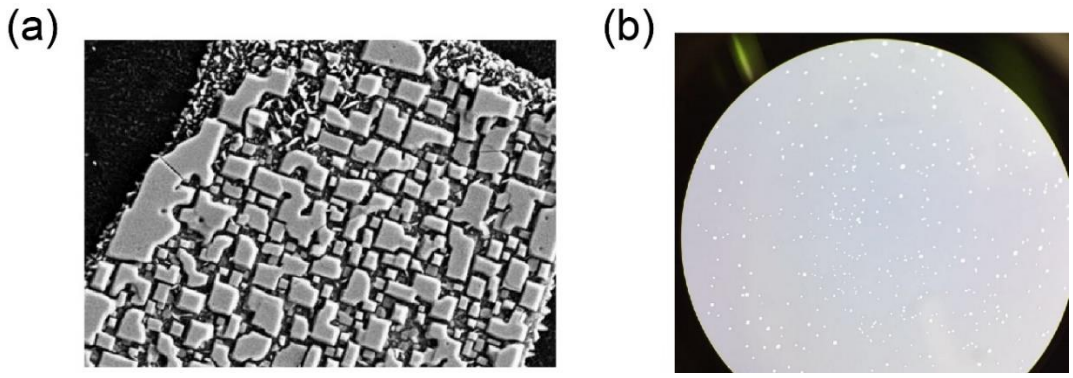

Fig. 3.17 Bi_2O_2Se grown on different substrates. (a) Bi_2O_2Se on Bi2212 superconductor. (b) Bi_2O_2Se flakes (small white squares) on $SrTiO_3$ substrate.

References

1 Fiori, G. *et al.* Electronics based on two-dimensional materials. *Nat. Nanotechnol.* **9**, 768-779 (2014).

2 Novoselov, K. S. *et al.* Electric field effect in atomically thin carbon films. *Science* **306**, 666-669 (2004).

3 Castro Neto, A. H., Guinea, F., Peres, N. M. R., Novoselov, K. S. & Geim, A. K. The electronic properties of graphene. *Rev. Mod. Phys.* **81**, 109-162 (2009).

4 Schwierz, F. Graphene transistors. *Nat. Nanotechnol.* **5**, 487-496 (2010).

5 Service, R. F. Beyond Graphene. *Science* **348**, 490-492 (2015).

6 Cui, X. *et al.* Multi-terminal transport measurements of MoS_2 using a van der Waals heterostructure device platform. *Nat. Nanotechnol.* **10**, 534-540 (2015).

7 Li, S. L., Tsukagoshi, K., Orgiu, E. & Samori, P. Charge transport and mobility engineering in two-dimensional transition metal chalcogenide semiconductors. *Chem. Soc. Rev.* **45**, 118-151 (2016).

8 Radisavljevic, B. & Kis, A. Mobility engineering and a metal-insulator transition in monolayer MoS_2. *Nat. Mater.* **12**, 815-820 (2013).

9 Radisavljevic, B., Radenovic, A., Brivio, J., Giacometti, V. & Kis, A. Single-layer MoS_2 transistors. *Nat. Nanotechnol.* **6**, 147-150 (2011).

10 Li, L. K. *et al.* Black phosphorus field-effect transistors. *Nat. Nanotechnol.* **9**, 372-377 (2014).

11 Qiao, J. S., Kong, X. H., Hu, Z. X., Yang, F. & Ji, W. High-mobility transport anisotropy and linear dichroism in few-layer black phosphorus. *Nat. Commun.* **5**, 4475 (2014).

12 Ohta, T., Bostwick, A., Seyller, T., Horn, K. & Rotenberg, E. Controlling the electronic structure of bilayer graphene. *Science* **313**, 951-954 (2006).

13 Zhang, Y. B. *et al.* Direct observation of a widely tunable bandgap in bilayer graphene. *Nature* **459**, 820-823 (2009).

14 Island, J. O., Steele, G. A., van der Zant, H. S. J. & Castellanos-Gomez, A. Environmental instability of few-layer black phosphorus. *2D Mater.* **2**, 011002 (2015).

15 Wu, J. X. *et al.* High electron mobility and quantum oscillations in non-encapsulated ultrathin semiconducting Bi_2O_2Se. *Nat. Nanotechnol.* **12**, 530, (2017).

16 Wu, J. X. *et al.* Controlled Synthesis of High-Mobility Atomically Thin Bismuth Oxyselenide Crystals. *Nano. Lett.* **17**, 3021-3026 (2017).

17 Zhang, K. Y. *et al.* Synthesis and thermoelectric properties of Bi_2O_2Se nanosheets. *Mater. Res. Bull.* **48**, 3968-3972 (2013).

18 Guo, D. L., Hu, C. G., Xi, Y. & Zhang, K. Y. Strain Effects To Optimize Thermoelectric Properties of Doped Bi_2O_2Se via Tran-Blaha Modified Becke-Johnson Density Functional Theory. *J. Phys. Chem. C* **117**, 21597-21602 (2013).

19 Lutchyn, R. M., Sau, J. D. & Das Sarma, S. Majorana Fermions and a Topological Phase Transition in Semiconductor-Superconductor Heterostructures. *Phys. Rev. Lett.* **105**, 077001 (2010).

20 De Franceschi, S., Kouwenhoven, L., Schonenberger, C. & Wernsdorfer, W. Hybrid superconductor-quantum dot devices. *Nat. Nanotechnol.* **5**, 703-711 (2010).

21 Recher, P., Nazarov, Y. V. & Kouwenhoven, L. P. Josephson Light-Emitting Diode. *Phys. Rev. Lett.* **104**, 156802 (2010).

22 Sasakura, H. *et al.* Enhanced Photon Generation in a Nb/n - InGaAs/p - InP Superconductor/Semiconductor-Diode Light Emitting Device. *Phys. Rev. Lett.* **107**, 157403 (2011).

23 Godschalk, F., Hassler, F. & Nazarov, Y. V. Proposal for an Optical Laser Producing Light at Half the Josephson Frequency. *Phys. Rev. Lett.* **107**, 073901 (2011).

24 Chen, Y. Studies on the electronic structures of three-dimensional topological insulators by angle resolved photoemission spectroscopy. *Front. Phys.* **7**, 175-192 (2012).

25 Damascelli, A., Hussain, Z. & Shen, Z. X. Angle-resolved photoemission studies of the cuprate superconductors. *Rev. Mod. Phys.* **75**, 473-541 (2003).

26 Berglund, C. N. Surface States at Steam-Grown Silicon-Silicon Dioxide Interfaces. *IEEE Trans. on Electron Devices* **13**, 701 (1966).

27 Statz, H., Demars, G. A., Davis, L. & Adams, A. Surface States on Silicon and Germanium Surfaces. *Phys. Rev.* **101**, 1272-1281 (1956).

28 Kresse, G. & Furthmuller, J. Efficient iterative schemes for ab initio total-energy calculations using a plane-wave basis set. *Phys. Rev. B* **54**, 11169-11186 (1996).

29 Tran, F. & Blaha, P. Accurate Band Gaps of Semiconductors and Insulators with a Semilocal Exchange-Correlation Potential. *Phys. Rev. Lett.* **102**, 226401 (2009).

Chapter 4

Development of Spatially Resolved ARPES Technique and Investigation on Square Graphene System

The development of new experimental instruments is essential for facilitating novel scientific research. Based on the general ARPES system, the spatially resolved ARPES technique has been recently developed, which features the ability to focus the incident beam in a submicron region. Using this new technique, the electronic structure of material systems with limited geometrical sizes can be easily investigated. In this chapter, we will introduce the basic concept of this advanced technique, and present our recent study on the square graphene system.

4.1 Background and Introduction

4.1.1 Development of the ARPES technique

The ARPES technique has been widely used to experimentally observe electron distributions inside solid materials. Over the last decades, we witnessed the great achievements made by using ARPES, including studies on unconventional superconductors, topological quantum materials, 2D materials etc[1-3]. Continuing efforts have been devoted to the further development of the ARPES technique. With the development of more advanced light sources (such as intense laser and synchrotron facility) and new generations of electron detectors, both the resolution and efficiency of ARPES measurements have been dramatically improved. However, the capability of ARPES nowadays is still limited, especially for the study of samples with limited size or lack of crystallinity. Considering that the ARPES technique is dedicated to reveal the comprehensive electronic states of materials, the state-of-art systems are designed to further explore these previously inaccessible materials.

Moreover, the complete description of an electron's state in the material requires not only the **energy (*E*)** and **momentum (*k*)**, which can be revealed by a standard ARPES system, but also the **position (*r*)**, **time (*t*)**, and **spin (σ)** information. Therefore, the development of future ARPES systems is to satisfy the abilities to probe these additional quantum numbers of electrons. Based on this idea, several advanced ARPES techniques have been brought forward. Spatially resolved ARPES[4-6] features its ability to focus the incident beam in a submicron region, which makes it possible to scan the sample surface and probe the electronic structure of certain spatial points. Time-resolved ARPES system (Tr-ARPES)[7,8] is designed to study the dynamics of electrons when the system experiences

perturbations. The incident laser beam is the combination of a pump pulse (used for perturbation) and a probe pulse (used for ARPES measurement). Spin-resolved ARPES[9,10] is equipped with the specially designed polarized target. The spin information of the photoelectrons can be determined through either a Mott scattering process or exchange scattering process.

These new techniques will become very powerful experimental tools in future material science research. Impressed by the great potential of these new techniques, besides the projects discussed in previous chapters, I have been working on the spatially resolved ARPES system during my DPhil studies as well. The spectromicroscopy beamline at Elettra synchrotron is the main system I have been using and the basic experimental setup has been introduced in Chapter 1. In the following, I will mainly introduce the recent developments of this special technique and my own results based on it.

4.1.2 Spatially resolved ARPES technique

A traditional standard ARPES system is indeed very powerful owing to its high energy and momentum resolutions. However, its large beam spot size (usually tens to hundreds of microns) limits its performance in material systems with small geometrical sizes. Therefore, the straight forward idea to solve the problem is to restrict the size of the incident beam and develop a spatially resolved ARPES system. As a consequence, the new technique is used to probe the electronic structure of such material systems that have spatial limitations, as illustrated in Fig. 4.1[11].

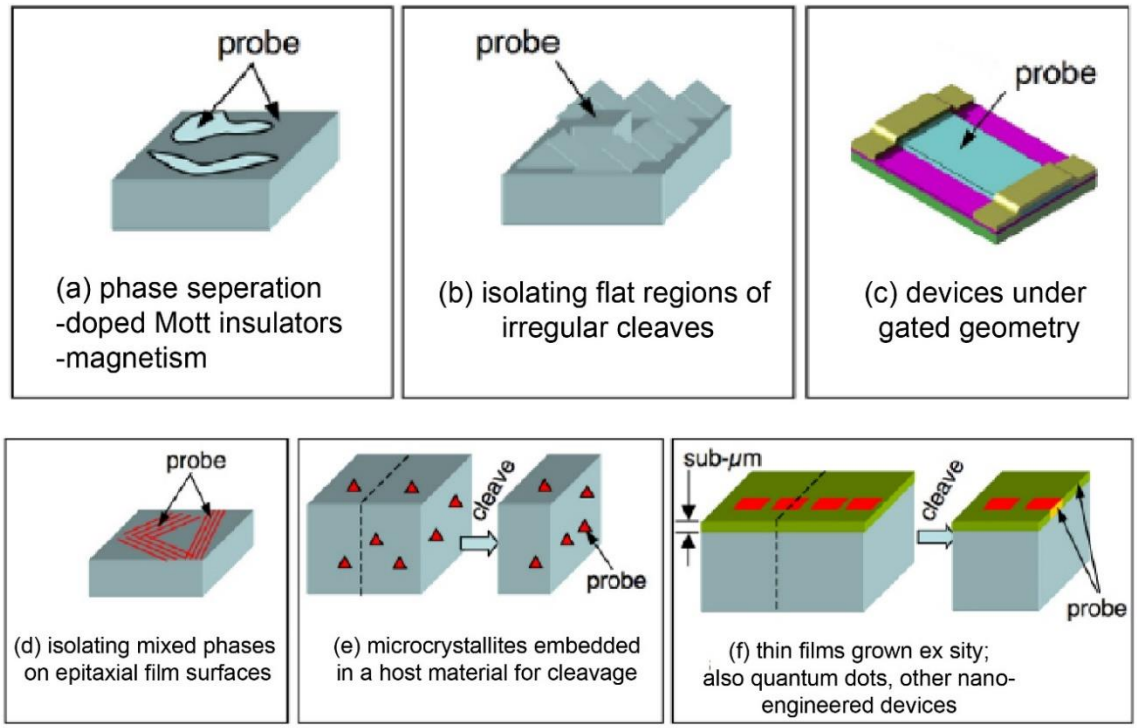

Fig. 4.1 Sample geometries which require a usage of spatially resolved ARPES system. Adapted from Ref. 11.

Doped Mott insulators and magnetic materials often form domains with different phases or magnetic properties on the surface of sample (e.g. $MnSi^{12}$). The size of the domain is typically around tens of microns. As a consequence, even the smallest beam spot of general ARPES system will cover and average the signals from different domains, and can therefore not distinguish the characteristic features of each domain. Moreover, as discussed in the previous chapters, single crystals for ARPES measurements are usually cleaved inside UHV chambers to obtain fresh and clean surfaces. However, the real situation is that usually only the layered materials can be easily cleaved, which results in large, ideal surfaces with a single crystal domain. The cleaved surfaces for other bulk materials are often very rocky, and contain small domains from different lattice faces. The condition becomes even messier if certain unusual planes are required (e.g. side cleavage of layered materials…). Now, with

the help of spatially resolved ARPES technique, not only the effect from adjacent crystal domains will be easily eliminated but also other different cleavage surfaces can be studied during the same experiment by merely shifting the beam spot. In this way, the efficiency and accuracy of ARPES experiments will be greatly improved.

The successful isolation of monolayer graphene in 2004[13] greatly motivates the research on 2D materials[14-16]. The 2D research field has quickly become one of the hottest areas in material science. Widely used fabrication methods including mechanical exfoliation, chemical vapor deposition (CVD) provide high-quality 2D films with a domain sizes around tens of microns[17,18]. The sample size is sufficient for transport or optical experiment, but still insufficient to perform a standard ARPES measurement. Therefore, the timely appearance of the spatially resolved ARPES technique provides us with great opportunities to study the electronic structure of these magic 2D sheets. In addition, electronic devices have been successfully fabricated based on these 2D materials (e.g. FET made with MoS_2[19], black phosphorus[20]…), showing great potential for future application in the electronic industry. With the help of spatially resolved ARPES, we will be able to directly visualize the electronic structure of these materials which is extremely important in testing their behaviors under different situations. Besides, the combination of spatially resolved ARPES with the gating geometry of devices further provides a new method in fundamental research that enables us to directly probe the unoccupied states in solids. Last but not least, as illustrated in Fig. 4.1, spatially resolved ARPES is also capable on the studies of epitaxial film surfaces with mixed phases, micro-crystallites embedded in materials, edge states of materials etc. In conclusion, this new tool will be in high demand in future scientific research.

Several spatially resolved ARPES at synchrotron light sources have already been built worldwide including Beamline 7 at Advanced Light Source (USA), ANTARES at Soleil synchrotron (France), Spectromicroscopy at Elettra (Italy) and Beamline I05 at Diamond

Light Source (UK, recently opened to users). I was lucky to have the opportunity to visit all these extraordinary beamlines during my DPhil study. The spectromicroscopy at Elettra is the place I spent most of my time. As has been introduced previously in Chapter 1, optical mirrors (Schwarzschild objectives) are used on the beamline to focus the incident beam, which limits the availability of the incident photon energy (27 eV or 74 eV)[6]. To fix the sample stage during the experiment, the small electron analyzer was equipped within the main chamber, which can move freely along two angle directions. Thanks to the great efforts of beamline scientist Alexei Barinov and other supporting staffs, the system is adjusted to be very stable and user-friendly during experiments. Many important achievements have recently been reached on this beamline which serves to be pioneering works in spatially resolved ARPES research field. In the following, we will introduce several typical works recently done by both our and Wilson's group at Warwick University.

Graphene has a high potential for future electronics due to its unique electronic properties. The interlayer coupling in a twisted bilayer graphene (tBLG) system leads to the formation van Hove singularities (vHSs) with enhanced density of states. As a consequence, the system exhibits great potential in ultrafast photodetection considering its strong light-matter interaction as well as the selectively enhanced photocurrent generation[21]. In our spatially resolved ARPES investigation[22], graphene domains with different thickness (bare copper, mono-, bi- and tri-layer graphene) can be clearly distinguished, as illustrated in the real space photoemission scanning map of the tBLG sample (Fig. 4.2(a)). The measured Dirac dispersions of graphene around the K point in reciprocal space are shown in Fig. 4.2 (b), which clearly indicates the vHSs in twisted bi-layer and tri-layer graphene respectively.

TMDs are another hot topic in the 2D material research field[14]. In our spatially resolved ARPES experiment, we studied the evolution of the band structure of MoS_2 according to the thickness of the sample[23]. Real space photoemission mapping (Fig. 4.2(c))

clearly illustrates the exfoliated 2H-MoS_2 flakes with different thicknesses (from multi-layer to monolayer), which can be easily identified by comparing related optical image over the same region. Band structure in each area were carefully investigated and we clearly identified the phase transition from indirect to direct band gap when the thickness is reduced to a monolayer (Fig. 4.2(d-e), more details can be found in *Ref. 23*). Furthermore, Wilson's group recently studied the electronic structure of van der Waals heterostructures based on TMDs materials by using this system[24]. As illustrated in Fig. 4.2(f), in contrast to the band structure of monolayer $MoSe_2$ or WSe_2, the $MoSe_2$/WSe_2 heterostructure clearly shows the pronounced hybridization between the two layers.

From the discussion above, we have briefly introduced the basic concept of the newly developed spatially resolved ARPES system as well as some recent studies. The successful investigation of relatively simple material systems makes us confident about this new technique and motivate further researches on more challenging topics. Based on this consideration, my journey in spatially resolved ARPES technique starts from a relatively easy material system, square graphene, which I will introduced in the following sections. After that, in the last part of this chapter, I will also briefly introduce some of our recent investigations which are still in progress.

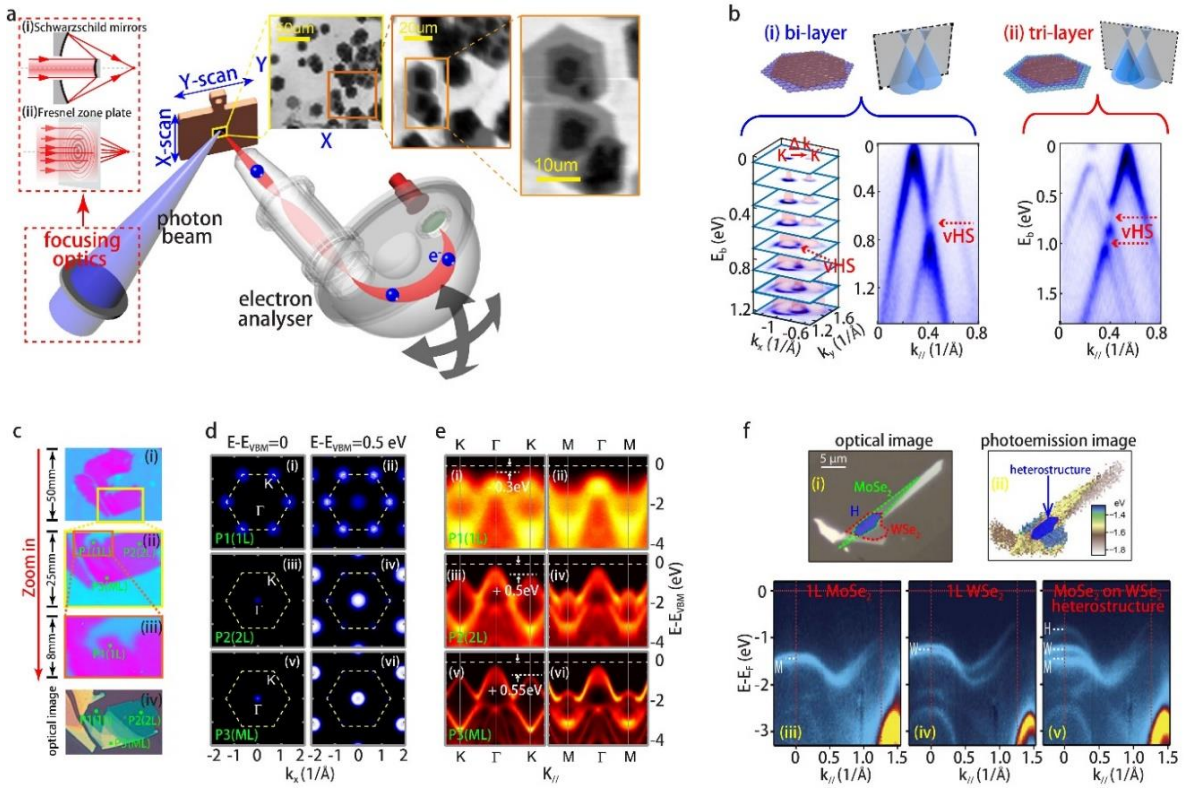

Fig. 4.2 Recent achievements of spatially resolved ARPES on the study of low-dimensional materials. (a) Illustration of the spatially resolved ARPES equipment settings. With either focusing optics (Schwarzschild mirrors) or zone plates, size of the incident beam can be limited into submicron region. This enables the scanning of the sample surface and the probing of electronic structure at certain spatial position. As an example, real space scanning of twisted bi-layer graphene is shown on the side. (b) Measurements on twisted bi-, tri-layer graphene, showing clearly vHSs. Adapted from Ref. 22. (c-e) Nano-APRES study on the evolution of band structures from multilayers to monolayer of MoS_2 thin flakes Adapted from Ref. 23. (f) Spatially resolved ARPES study on the $MoSe_2/WSe_2$ heterostructure. Adapted from Ref. 24.

4.1.3 Introduction to square graphene system

For a long time, great efforts have been devoted to improving the method of mass fabrication of high-quality large-scale graphene sheets applicable in industry. Cu foil are the most promising catalytic substrate to grow large graphene sheet via CVD[17,18]. However, the

quality of large-scale CVD graphene films is still worse than the mechanically exfoliated ones[25-28]. Therefore, further improvement of the growth method is still needed.

Recently, Peng's group from Peking University reported a rapid growth method of large single-crystal graphene on commercial copper foils[29]. Both the growth rate and quality of the graphene films are far better than those in the previous studies. As demonstrated in Fig. 4.3(a), large commercial Cu foils are firstly rolled or vertically stacked with an interlayer distance around tens of micrometers before entering the CVD system. Large square graphene films can be grown with a diagonal size up to 3 mm within only 10 mins of growth time (Fig. 4.3(b)). Therefore, the maximum growth rate of graphene sheet reaches 300 μm min^{-1}, which is considerably fast than the previous reports. The high quality of the graphene sheets reported was verified by transmission electron microscopy (TEM), selected area electron diffraction (SAED) and Raman spectra. The group ascribed the ultrahigh growth rate to the so-called molecular flow mode during CVD process. H_4 and CH_4 gases are trapped in the narrow spaces between stacked Cu foils, leading to a higher colliding frequency that enhances local concentration of carbon flux therefore accelerates its interaction with Cu foil.

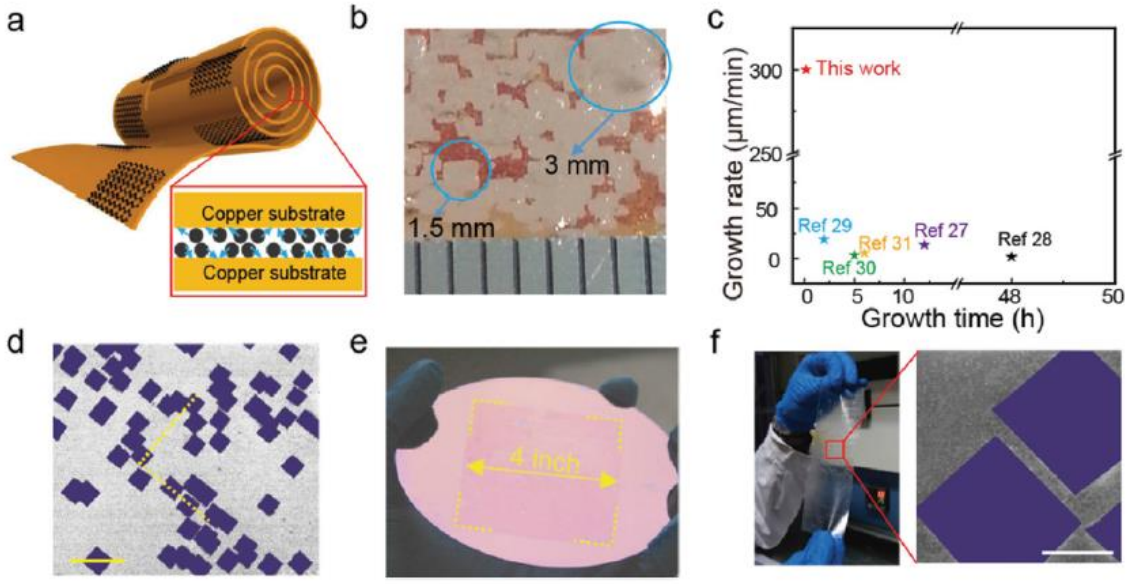

Fig. 4.3 Fast growth of large single-crystalline graphene arrays on copper foils. (a) Schematic of the fast growth method. Inset: schematic of H_2/CH_4 transport and decomposition under molecular flow. (b) Image of graphene domains grown on inner surface of the stacked Cu foils. (c) Growth rate and growth time comparison of millimetre-sized single-crystalline graphene domains produced by different growth methods. (d) SEM image of the square graphene arrays on Si/SiO_2 substrate transferred from the inner surface of the stacked Cu foil. (e) Contrast-enhanced photograph of the continues graphene film transferred onto 4 inch Si/SiO_2 wafer. (f) Image of single-crystalline graphene arrays transferred onto PET substrate (left) and the corresponding SEM image (right). Scale bar: 100 μm. Adapted from Ref. 29.

Another interesting phenomenon in this work is the formation of square-shaped graphene, instead of the ordinary hexagonal ones. As can be clearly seen in Fig. 4.3(d), all the graphene grains have square shapes with their sides perfectly aligned. Different grains touch each other and merge into larger graphene sheet with presumably the same orientation. This point is very important for the growth of large-scale high-quality graphene films. The report suggests that the formation of the square shapes may be caused by the surface reconstruction of the underlying Cu foil. As illustrated in Fig. 4.4, during the

growing process, the high temperature leads to a reconstruction on the surface of Cu foil, which turns the multi-domain Cu surface into inch-sized Cu (001) single surface. The formed single crystal surface greatly enables the rapid growth of graphene grains, while its four-fold symmetry may lead to the formation of the square shapes graphene.

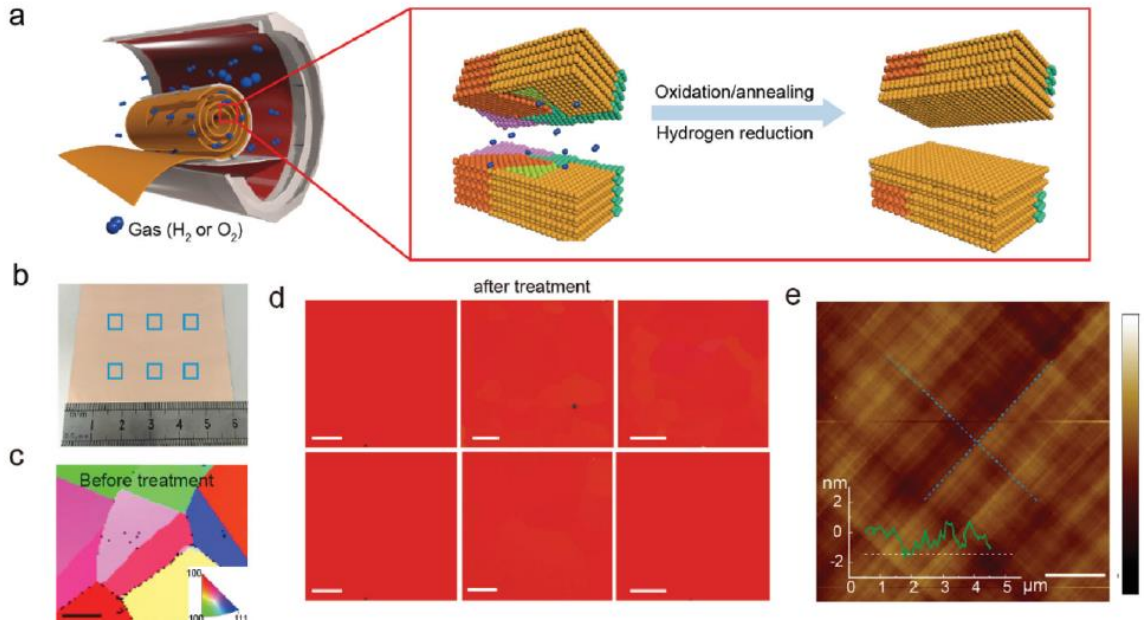

Fig. 4.4 Surface engineering of polycrystalline Cu foil. (a) Schematic of the production of single-crystalline Cu with (001) orientation on the surface of polycrystalline Cu foil. (b-c) Image and EBSD map of Cu foil before monocrystallization treatment. (d) EBSD maps of the Cu foil after treatment, taken at regions indicated in (b). (e) AFM image for the Cu foil, showing the direction of Cu atomic steps. Adapted from Ref. 29.

In conclusion, Peng's group creatively brought up a fast growth method to obtain large uniform graphene sheets through very simple procedures. The development of this new method buries the giant gap between conceptual and experimental availability for the wide applications of graphene materials.

Nonetheless, despite its great importance, many questions remain unclear in this material system. For instance, we wonder whether each individual graphene grains share the same crystal orientations (the alignment of square shape may not necessarily lead to the alignment of crystal structure). Besides, will the quality of the graphene be deteriorated after their merging between different grains? Also, is there any quantitative relation between the crystal orientations of square graphene sheets and the underlying Cu (001) surface with four-fold symmetry?

To answer these questions, we can probe the electronic structure of both graphene sheets and underlying Cu at different spatial points. Therefore, the spatially resolved ARPES system is required for the investigation. The penetration of the photoelectrons enables us to accumulate the signals from both graphene and underlying Cu, which may give some hint for the reason why the square shape is formed.

4.2 Study of square graphene system

4.2.1 Basic operations in spatially resolved ARPES

Based on motivations above, we carried out spatially resolved ARPES experiments on the square graphene system at the Spectromicroscopy beamline. In contrast to single crystals which can be cleaved to expose fresh surface, 2D material can only be annealed it to get rid of unwanted air contaminations attached to the sample surface. As a consequence, the square graphene samples were annealed first in the UHV interface chamber at around 400 ℃ for 2 hours, before going into the main chamber for ARPES measurement.

Figure 4.5(a) illustrates the basic measuring geometry in spatially resolved ARPES experiment. With the x and y motors of the sample stage, we are able to scan the sample surface with small steps (e.g. 0.5 μm). Figure 4.5(b) illustrates a typical real space scanning of the sample together with the related optical image. Signals from both graphene and underlying Cu substrate are simultaneously accumulated by the electron analyzer. The energy window of the analyzer was chosen to be around 2 eV below Fermi level, where the intensity is dominated by the electrons originated from *d* band of Cu. Therefore, the signal will be much weakened at the places covered by graphene. Graphene grains can be easily distinguished with very high spatial resolution.

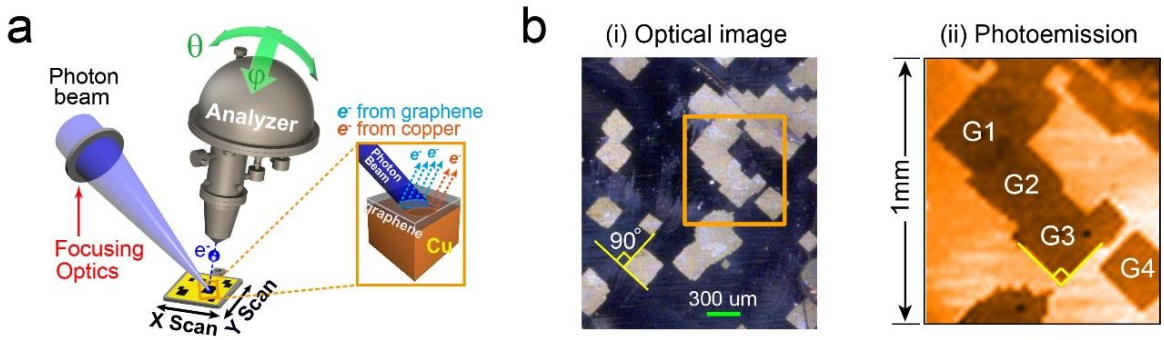

Fig. 4.5 Spatially resolved ARPES measurement on graphene on Cu foil. (a) Schematic of spatially resolved ARPES measurement on graphene on Cu foil. The penetration of the photon beam enables the probing of band structures from both graphene and Cu. (b) (i) Real image of square graphene on Cu foil. (ii) Real space scanning, illustrating the same region. Intensity of the map is selected from the *d* band of Cu. Therefore, the signal is blocked where there is graphene.

The next step is the measurement of the electronic structure of graphene. As introduced in Chapter 1, the electron analyzer at the beamline can be rotated freely along both θ and φ directions, to accumulate photoelectrons from different angles. Therefore, we

fixed the beam spot on the graphene sheet, and systematically rotate analyzer to map out the band dispersion in full reciprocal space. The band structure of graphene features its Dirac dispersions at six K (K') points in its BZ, as illustrated in Fig. 4.6. A slice plot of constant energy contours clearly shows the Dirac dispersion of the graphene, which confirms the high quality of the film. Remarkably, the appearance of only one set of Dirac cones indicates that the graphene film studied is a monolayer.

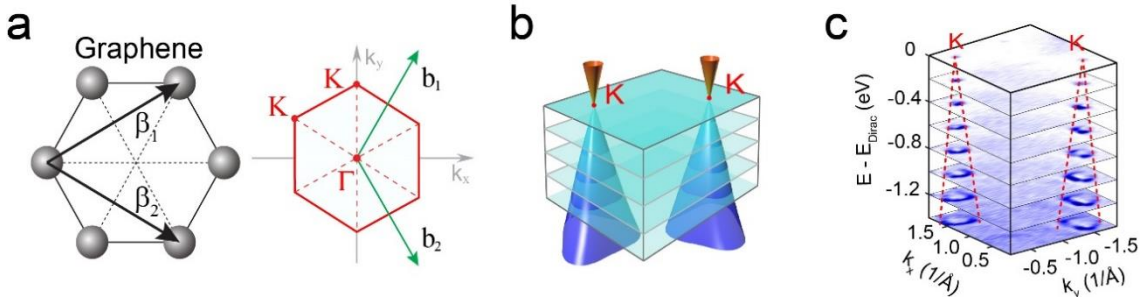

Fig. 4.6 Crystal structure of graphene and the measurement of Dirac cones. (a) Crystal structure of graphene and the related BZ. The Dirac cones locate at the K(K') point in reciprocal space. (b) Illustration of the evolution of Dirac cones according to binding energy. (c) Slices plot of the measured Dirac cones of the square graphene on Cu.

4.2.2 Quality and orientation of graphene grains

Based on the above general operations for both real space and reciprocal space mapping, we are now able to perform further investigations of the system. As described previously, aligned square graphene grains merge together to form larger graphene sheets. It is interesting to know if the different grains have the same crystal orientation. If so, do the merged regions still maintain the good quality and crystal orientation? To answer the questions, we performed intensive ARPES measurements on graphene grains from two

different samples labeled as Sample A and Sample B (from different growth batches). The real space scanning of Sample A and B are displayed in Fig. 4.7(a) and (e), respectively. In Sample A, we aim to compare the electronic structures of graphene among merged grains together with an isolated unmerged one. While in Sample B, we focus on the merging region between two grains. The constant energy contours cutting through the Dirac points in momentum space at each data positions are shown in Fig. 4.7(b) and (f), respectively. Evidently, from each graphene domain, only a single set of Dirac points are observed as expected, proving their monolayer nature.

As the result, in Fig. 4.7(b) or (f), we can see that the graphene dispersions from different data points on the same sample are almost identical in momentum space, which can be verified by overlapping these measurements together for comparison (Fig. 4.7(c) for Sample A and Fig. 4.7(g) for Sample B). The slight variation of the Dirac point positions is caused by the experimental uncertainty resulting from the surface unevenness of the Cu foil (corrugation is common in commercial Cu foils used in CVD growth) and the angle variation due to the rotation of electron analyzer in ARPES measurement. Since the orientation of the band structure in momentum space is reciprocal to the lattice orientation in real space, the good agreement of the band structures indicates that the lattice orientation of different graphene grains in each sample is also well aligned, which is consistent with reported selected-area electron diffraction measurements[29].

In the case of sample B, we find that the merged regions between different grains also show high crystalline quality with the same lattice orientation as individual grains. As illustrated in Fig. 4.7(e), B2 resides in the merged area of two graphene grains BG1 and BG2. The related measurement shows matched orientation to their neighboring grains. This observation suggests that the individual graphene grains can merge into a larger sheet with

similar crystalline orientation, making our CVD growth a promising method to grow large-scale graphene sheets with high quality.

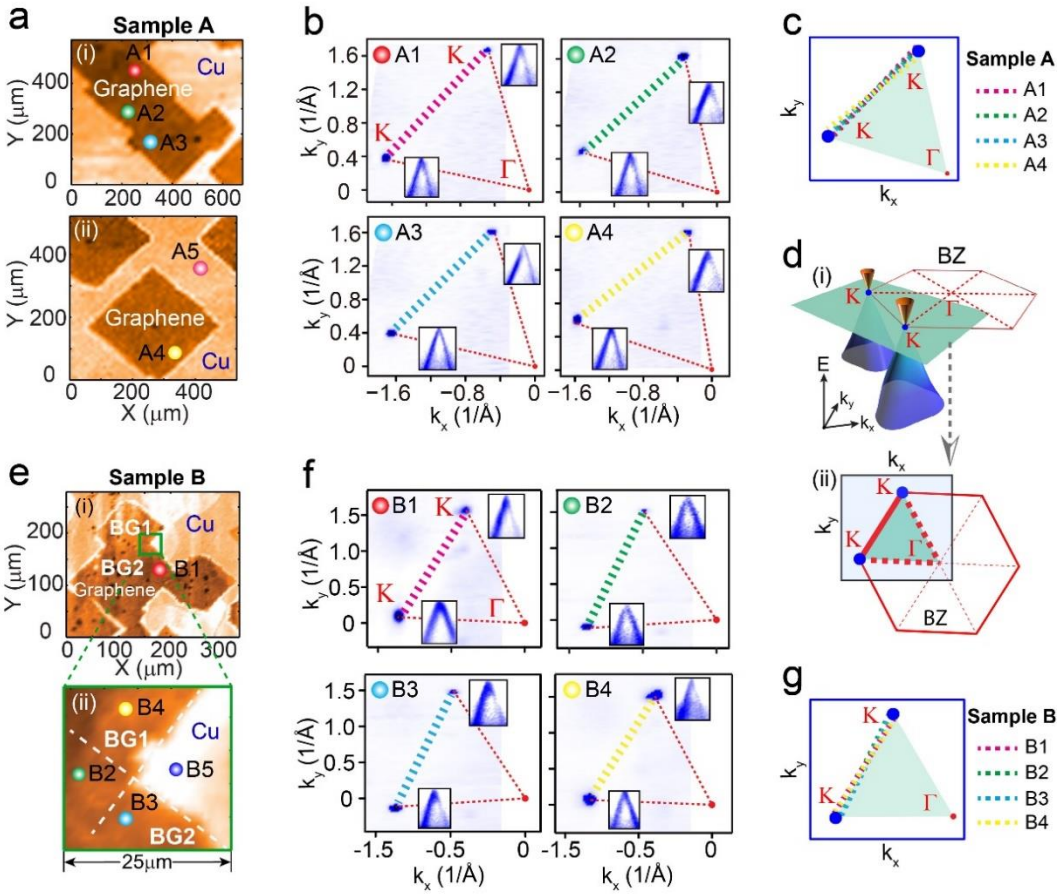

Fig. 4.7 Orientation of single-layer square graphene grains. (a) 2D real-space maps of Sample A. (b) Constant energy contours (crossing the Dirac points in the momentum space) measured at data positions indicated in (a). (c) K – K directions from all four measurements, showing the same orientation. (d) Schematic of Dirac cones of graphene and constant energy contour crossing the Dirac points. (e-g) Same as (a-c) for sample B.

4.2.3 Orientation relations with underlying Cu

After establishing that the square-shaped grains are indeed single-layer graphene sheets with aligned crystal orientation, we can further investigate if and how their electronic structures, square shape, and lattice orientation are related to those of the underlying Cu foil. The result of the investigation may help to understand the role of Cu substrate in the CVD growth that is still under debate[30-37].

First, we measured the electronic structure of bare Cu by focusing the photon beam to Cu substrate next to the graphene grains (Fig. 4.8(a)). The constant energy contour of Cu *d* band (-2.3 eV binding energy, Fig. 4.8(b)) clearly shows four-fold symmetry with the periodicity (~ 2.5 $Å^{-1}$) consistent with the Cu (001) surface. In order to further check the uniformity of the Cu substrate, an unfocused photon beam (> 50 μm beam spot size) was used (Fig. 4.8(e), 100 eV photons were used to enhance the Cu *sp* band near E_F). Remarkably, the sharp single-domain Fermi-surface with four-fold symmetry clearly demonstrates the single crystalline nature of Cu (001) substrate in large area that was also confirmed by electron back-scatter diffraction (EBSD) measurements[29].

Next, we moved the photon beam to the adjacent graphene grain, where the band structures of graphene and Cu substrate can be simultaneously measured. The spectra taken at aforementioned graphene data points (Fig. 4.7(a),(e)) from both Sample A and B are displayed in Fig. 4.8(d). In addition to the square-shaped band contours (from Cu substrate), additional triangular band contours centered at the K points originated from the Dirac cones of the graphene grains were also spotted. With band structures from both graphene grains and the Cu substrate, the relation between their orientations can be quantitatively examined. The angle α (Fig. 4.8(f)) was defined to be the angle between the $K - K'$ direction of the graphene BZ and the $X - M$ direction of the Cu (001) BZ. Interestingly, after comparing

different graphene grains from Sample A and B (Fig. 4.8(f)), we find that although in each sample the values of α are consistent for different graphene grains (considering the substrate corrugation and experimental uncertainty), α is clearly different between different samples. Therefore, we conclude that the crystal orientation of graphene grains are not determined by the underlying Cu lattice. And the formation of the square shape may not have any relation with the crystal orientation of graphene.

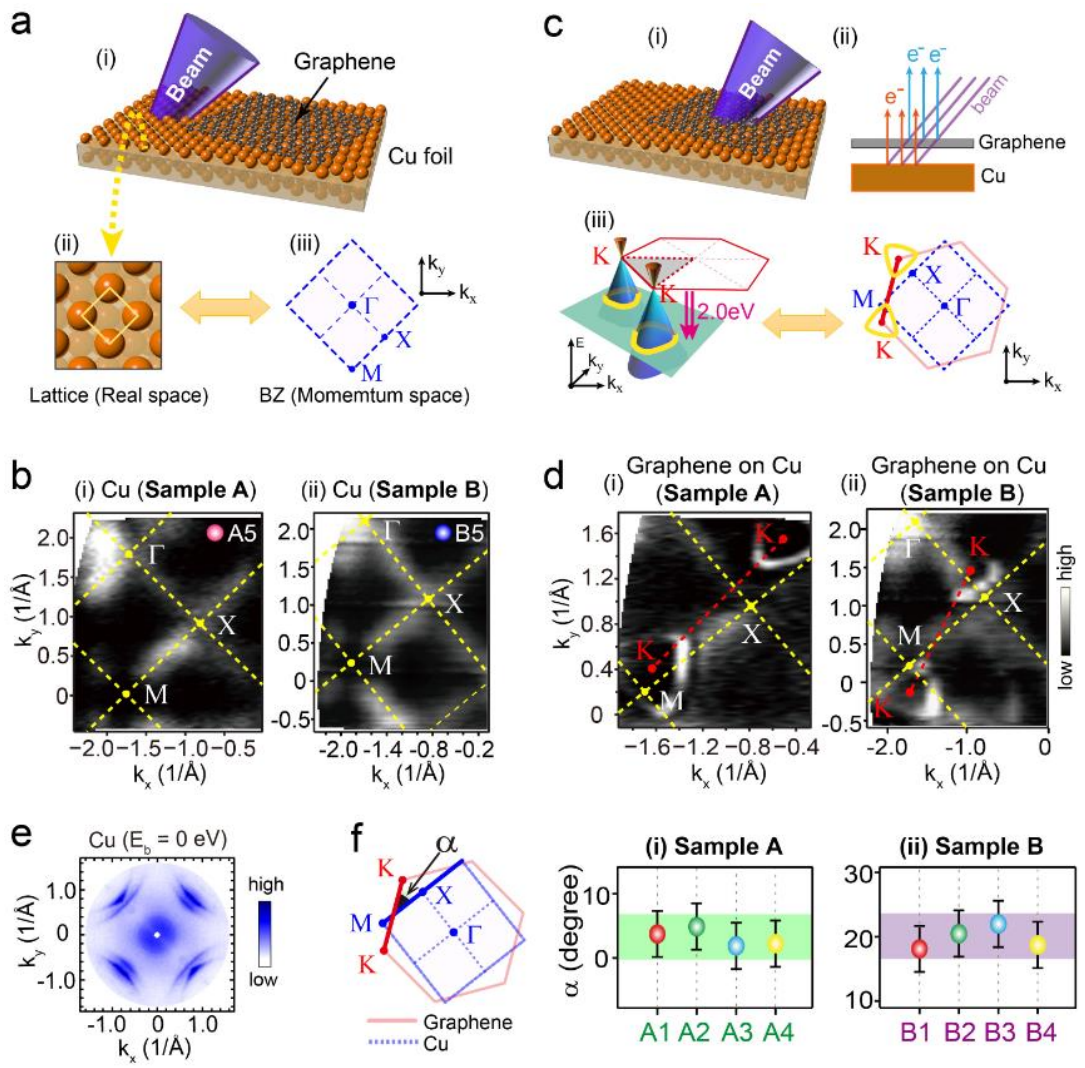

Fig. 4.8 Alignment of Graphene grains and underlying Cu substrate. (a) Schematic of the measurement on bare copper. (b) Band contour at binding energy -2.3 eV showing the four-fold symmetry of Cu (001) orientation. Data points illustrated in previous figure (Fig. 4.7). (c) Schematic of the measurement on graphene. Signals from both graphene and copper can be obtained. Orientation relation between graphene and copper can be deduced. (d) Band contour at binding energy -2.3 eV showing both four-fold symmetrized copper *d* band and Dirac cones from graphene. (e) Fermi surface of the Cu substrate stemming from the *sp* band, measured at the ANTARES beamline with unfocused photon beam (beam size > 50 μm).Four-fold symmetry proves the (001) orientation of Cu. (f) Position dependence of α (defined as the angle between the K - K direction of graphene and the X-M direction of Cu substrate). An error bar of ±3° is applied, considering both the wrinkled nature of Cu foils and instrumental resolution.

4.2.4 Possible growth mechanism

However, there is another possibility that the sides of the square shape may be aligned with lattice directions of Cu. To verify that, we convert our orientation from momentum space to real space (the electronic structure orientation in momentum space is reciprocal to the lattice orientation in real space).

In Fig. 4.9, the reconstructed graphene lattice orientation, the geometrical side orientation of the grains, and the high-symmetry directions in reciprocal space of the Cu (001) surface (with which lattice orientation of Cu can be deduced), are plotted together. The zigzag and armchair edges are roughly aligned with the sides of the graphene grain in Sample A, while misaligned in Sample B, again confirming our previous conclusion. Despite this difference, both samples show that the sides of the graphene grains (blue dashed lines in real-space maps) are significantly parallel to the $X - M$ direction of the Cu substrate (i.e. the Cu <110> direction, yellow dashed lines in reciprocal-space maps).

This correspondence in both samples suggests that certain Cu atomic direction plays an important role in the growth of the square graphene grains. Figure 4.9(c) shows a possible picture where graphene grains preferentially nucleate and extend along the Cu <110> step edge (since atomic steps on Cu foils were spotted in atomic force microscope measurements[30]). In this regard, the shape and orientation of graphene grains are highly influenced by the Cu (001) crystalline surface structure.

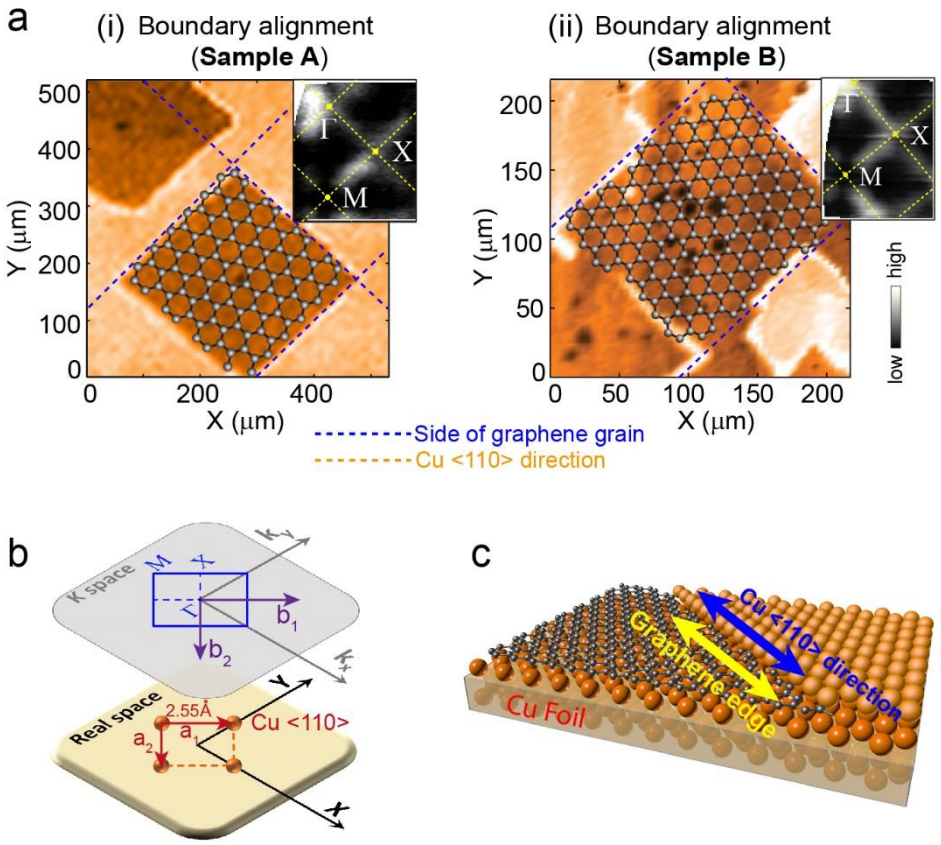

Fig. 4.9 Alignment of Graphene and Copper in real space. (a) Alignment relations of graphene and copper on sample A and B, respectively. The boundaries of the graphene (dashed blue lines) are aligned with high symmetry directions (dashed yellow lines) of copper (001) surface. (b) Direction relation between momentum space and real space of copper (001) surface. (c) Sides of square graphene are parallel aligned with <110> direction of underlying copper atoms.

In summary, we successfully applied the state-of-art spatially resolved ARPES technique for the systematic study of the electronic structure of aligned square graphene system. The high quality and well-aligned orientation of the graphene sheets are confirmed by our result (only some of the data are illustrated, we also examined many insulated squares and the orientation of them are the same for a given sample). Besides, we revealed that the crystalline surface structure of the Cu foils plays an essential role in the formation of

the square shape graphene during CVD growth. Most importantly, our work demonstrates the potential of this new experimental technique in the study of low-dimensional materials down to atomic thickness and sub-micrometer lateral size.

After the successful investigation on the square graphene system, we found it to be a very good platform to perform more challenging work. In the following, our recent work on the artificially stacked tBLG will be introduced.

4.3 Study on artificially stacked graphene

4.3.1 Fabrication of stacked graphene sample

Many heterostructures of layered materials with van der Waals interlayer interaction have recently been designed in order to artificially create some special electronic structures[16]. Graphene is inevitably the center of the research due to its robustness and special electronic properties. As has been introduced at the beginning of the chapter, tBLG exhibits a van Hove singularity which leads to strong light-matter interaction as well as selectively enhances photocurrent generation[21]. However, the current CVD growth method of tBLG suffers from limited domain size and uncontrollable angle. Therefore, there is not yet any reliable scalable production method to fabricate high-quality tBLG with controlled angles.

With the high-quality monolayer graphene sheet fabricated from aforementioned fast growth method, we developed a facile method to create large domain tBLG structure with controlled twisted angles by simply stacking two square graphene together. The important role of spatially resolved ARPES in the work is that the quality of the stacked graphene

sheets and the realization of interlayer coupling can be examined by detecting the characteristic Dirac cones as well as the VHS in the band structure.

Figure 4.10 introduces the process of our fabrication method together with basic characterizations. Three simple steps are included: (i) Polymethyl methacrylate (PMMA) is coated onto the monolayer square graphene grown on copper foil, before the copper foil is removed by $Na_2S_2O_8$ solution. (ii) Graphene attached on transparent PMMA is stacked onto another graphene domain on copper foil, with controlled angle under an optical microscope. (iii) The heterostructure was baked to increase interlayer interaction and then the PMMA was removed by acetone. During the process, the PMMA only touches the outer surface of the upper graphene layer, the interlayer space between two graphene sheets remains free from polymer contamination therefore enabling the appearance of interlayer coupling.

Using this method, tBLG samples with different twist angles can be easily fabricated as illustrated in Fig. 4.10(b) (since we already know from previous discussion that the graphene square for a given sample has the same crystal orientation). SAED experiments were performed on both graphene domains as well as the overlapping region (Fig. 4.10(c)). From the diffraction pattern, the twist angle can be easily determined.

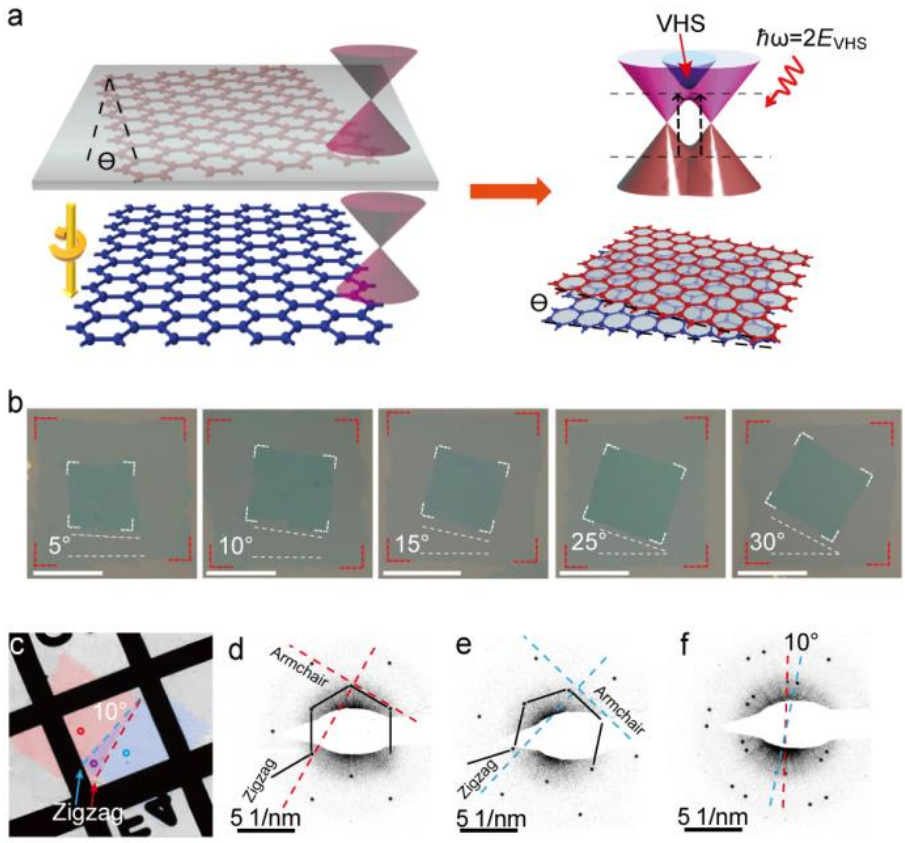

Fig. 4.10 Artificially stacked square graphene. (a) Schematic of the stacking process and the formation of vHS in tBLG. (b) Optical images of as-prepared large-domain tBLG with controlled angles on SiO_2/Si substrates. Scale bar: 100 μm. (c) Low-magnification TEM image of the tBLG domains. Two graphene layers and overlapped region are labeled with different colors. (d-f) Corresponding SAED patterns showing signal from two graphene domains and the overlapped region.

4.3.2 Electronic structure of stacked graphene

Spatially resolved ARPES was performed on the fabricated tBLG sample. Similar to our operations in the previous study on square graphene system, the tBLG sample was also annealed at 400℃ for 2 hours before being transferred into the main chamber. During the real space scanning over the sample surface, an energy window that covers *d* band of copper

was again selected. As illustrated in Fig 4.11(a), large square graphene sheet with two smaller stacked graphene was clearly spotted.

By placing the beam spot onto one of the smaller graphene grains, we were able to probe the electronic structure of tBLG. Two sets of characteristic Dirac band dispersions from two graphene layers are illustrated in the slice plots of constant energy contours (Fig. 4.11(b)). The intersection point of the two Dirac cones was labeled with a red arrow. From the band dispersion spectrum cutting through the intersection point (Fig. 4.11(c)), a mini gap opening was clearly observed, which can be better illustrated by the related DOS. This gap opening originates from the interlayer coupling between two graphene layers and leads to the formation of vHS in tBLG system, as demonstrated previously in Fig. 4.10(a). Furthermore, a twisted angle of ~19.5° can be deduced from constant energy contour (Fig. 4.11(d)), which cut through Dirac points of two graphene layers.

The tBLG sample was later examined by Raman spectrum and further fabricated into high-performance photodetectors, of which the details can be found in our publication.

In conclusion, we have successfully prepared the large domain tBLG sample with controlled twist angle through a clean transferring method. By using the spatially resolved ARPES system, we successfully verified the good quality of our sample and addressed the formation of interlayer coupling in the system. Our study paves the way for further spatially resolved ARPES studies on artificially created heterostructures, which exhibit novel physical phenomena.

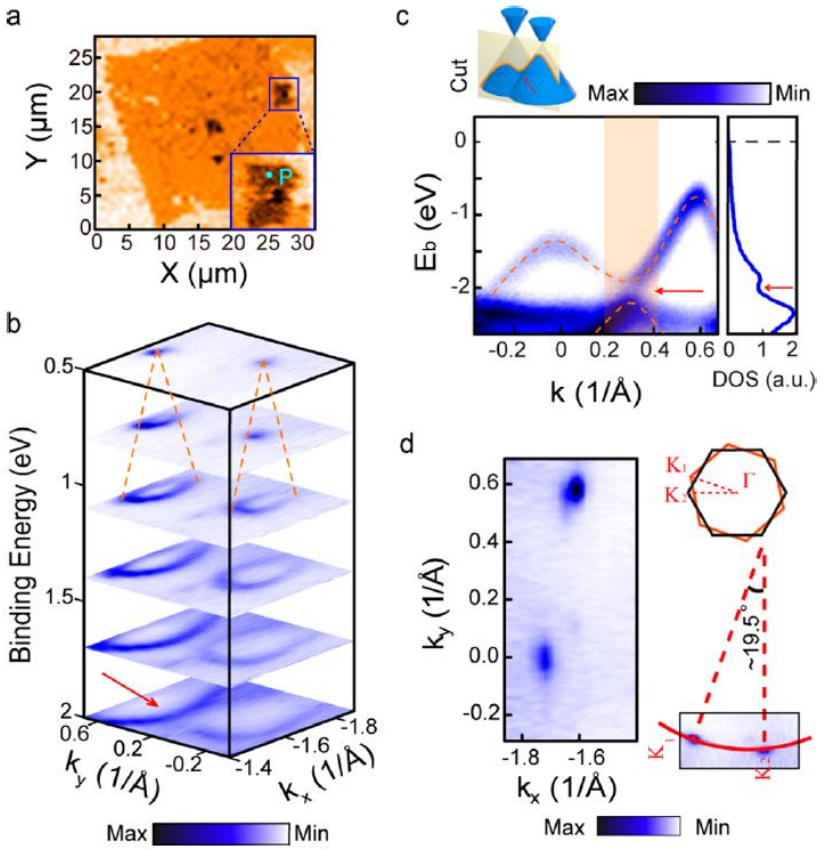

Fig. 4.11 Spatially resolved ARPES experiment on artificially stacked square graphene. (a) 2D real-space micro-ARPES map of the tBLG. (b) Stacking plots of the constant-energy contours at different binding energy of as-prepared tBLG. (c) Band dispersion showing the intersection of two Dirac cones and the emergence of a vHS. (d) Constant energy contour crossing Dirac points showing a twisted angle around 19.5 °.

4.4 Perspective of spatially resolved ARPES research

From the above investigations, we have proved the importance of the spatially resolved ARPES technique for novel scientific research. The small incident beam spot provides us with the ability to study the electronic structures of spatially limited material

systems. In the following, we will briefly introduce some of our recent projects, which are still in progress.

4.4.1 2D materials and heterostructures

Research on 2D materials is a very important topic in condensed matter physics. Due to their exquisite physical, electrical, mechanical and optical properties, thin films bounded by van der Waals force, such as graphene, hexagonal boron nitride (hBN), TMDs, etc., are of extensive research interest.

In these materials, the strong covalent bonds keep the stability of these 2D material sheets, while the relatively weaker interlayer van der Waals force makes it possible to fabricate rich heterostructures even by simply stacking them together[16]. In this way, electronic structures could be artificially controlled and new states would be fabricated by certain stacking sequences (as illustrated in Fig. 4.12(a)). For instance, giant renormalization of the spin-orbit coupling was observed in single layer WS_2 on a hBN substrate (WS_2/hBN heterostructure)[38], indicating that the electronic properties are widely tunable in TMD/hBN heterostructures. Practically, many of the van der Waals heterostructures have been proved to be ideal playgrounds for the investigation of both fundamental physics properties as well as possible applications. Considering the miniature sizes of these heterostructures (~ on the order of microns), spatially resolved ARPES is a natural choice for studying their electronic structures.

At the moment, we are working on several new 2D material systems as well as their heterostructures. For example, tellurium thin films are proposed to be promising semiconductors[39]. Topological mosaic patterns are expected to appear in the TMD bi-layer heterostructures[40]. More recently, the very exciting discovery of strongly correlated electron

states and unconventional superconducting states in twisted bi-layer graphene systems[41,42] also motivate us a lot for the study on its detailed electronic structure.

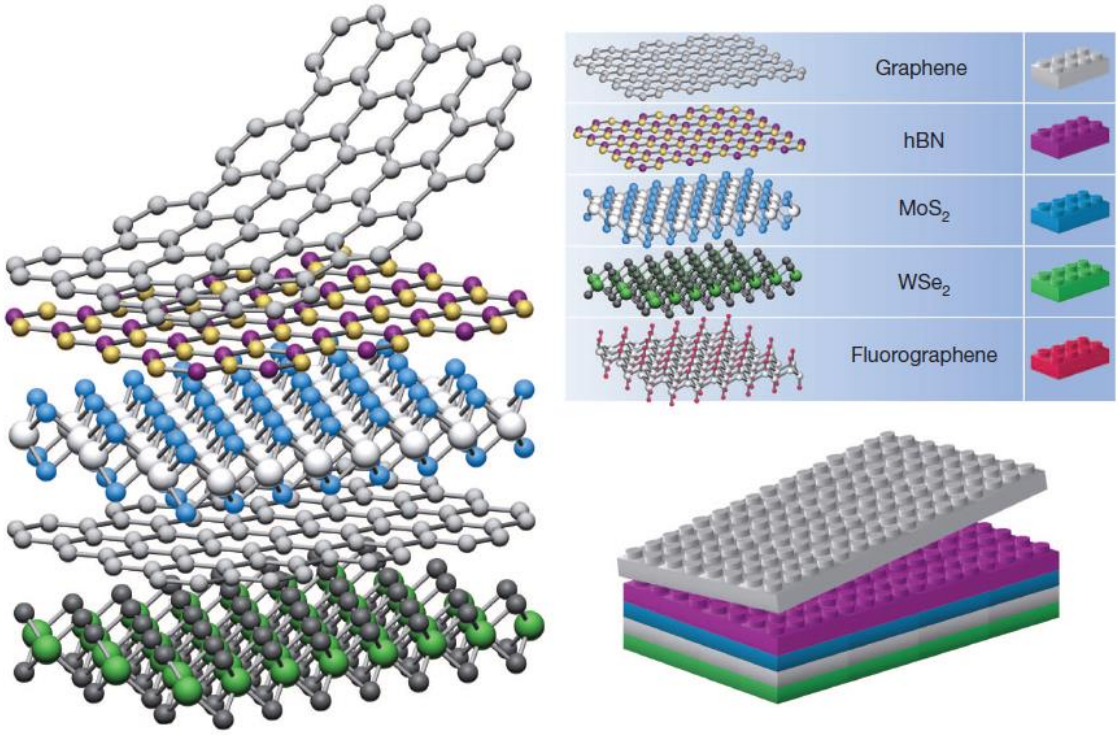

Fig. 4.12 Building van der Waals heterostructures. If one considers 2D crystals to be analogous to Lego blocks (right panel), the construction of a huge variety of layered structures becomes possible. Conceptually, this atomic-scale Lego resembles molecular beam epitaxy but employs different "construction" rules and a distinct set of materials. Adapted from Ref. 16.

4.4.2 Devices and gating technique

Tuning the carrier concentration of low dimensional materials with external influence leads to the appearance of exotic electronic and photonic properties. Electric gating can

introduce phase transitions such as superconductivity[43], charge density waves[44] and Lifshitz transition. In the past years, the ion-liquid method has been widely employed for electric gating which is far more efficient than the conventional dielectric method[45]. However, the overlay of liquid electrolyte over sample materials makes the surface measurements (e.g. ARPES, STM) impossible. Additionally, the reaction between the liquid electrolyte and target materials often limit the application of this method.

Recently, a new gating method, using solid ion electrolyte, was developed[46]. Similar to the ion-liquid gating, solid ion gating can also achieve very large electronic tuning range, while it avoids the disadvantages of the ion-liquid gating. More importantly, this method does not cover the top sample surface (Fig. 4.13(a)) thus making it compatible with the spatially resolved ARPES study. The method has recently been successfully demonstrated in tuning the superconducting property of iron chalcogenide FeSe films[46]. The T_c is tunable from 10~46.6 K, together with significant increase in the carrier concentration (up to 1 electron per iron). Therefore, the gated FeSe system proves to be a good platform to study the keen relationship between electronic structure and superconductivity.

The development of ARPES-gating technique itself is extremely meaningful in the sense of directly visualizing unoccupied states in solids. Currently, we are working on developing this special technique using the well-understood materials (e.g. graphene and MoS_2). If successful, we will further apply this technique to the study of more interesting systems, such as FeX (X=S, Se, Te) thin films which demonstrate enhanced T_c by solid electrolyte gating.

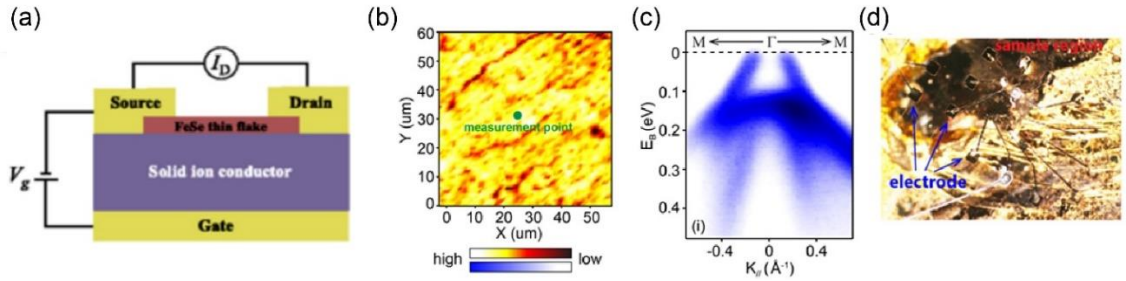

Fig. 4.13 ARPES-gating technique. (a) Schematic of solid ion gating method[46]. (b) Spatial mapping of FeS through spatially resolved ARPES technique measured in BL I05-nanoARPES branch, DLS. **(c)** Measured photoemission spectrum at marked point in (b). (d) A typical gating device we measured with spatially resolved ARPES system.

References

1 Damascelli, A., Hussain, Z. & Shen, Z. X. Angle-resolved photoemission studies of the cuprate superconductors. *Rev. Mod. Phys.* **75**, 473-541 (2003).

2 Lu, D. H. *et al.* Angle-Resolved Photoemission Studies of Quantum Materials. *Annu. Rev. Conden. Ma. P.* **3**, 129-167 (2012).

3 Chen, Y. Studies on the electronic structures of three-dimensional topological insulators by angle resolved photoemission spectroscopy. *Front. Phys.* **7**, 175-192 (2012).

4 Rotenberg, E. & Bostwick, A. microARPES and nanoARPES at diffraction-limited light sources: opportunities and performance gains. *J. Synchrotron Radiat.* **21**, 1048-1056 (2014).

5 Avila, J. *et al.* ANTARES, a scanning photoemission microscopy beamline at SOLEIL. *J. Phys. Conf. Ser.* **425**, 192023 (2013).

6 Dudin, P. *et al.* Angle-resolved photoemission spectroscopy and imaging with a submicrometre probe at the SPECTROMICROSCOPY-3.2L beamline of Elettra. *J. Synchrotron Radiat.* **17**, 445-450 (2010).

7 Turcu, I. C. E. *et al.* Ultrafast science and development at the Artemis facility. *Proc. SPIE.* **7469**, 746902 (2010).

8 Sobota, J. A. *et al.* Ultrafast Optical Excitation of a Persistent Surface-State Population in the Topological Insulator Bi_2Se_3. *Phys. Rev. Lett.* **108**, 117403 (2012).

9 Okuda, T. *et al.* A new spin-polarized photoemission spectrometer with very high efficiency and energy resolution. *Rev. Sci. Instrum.* **79**, 123117 (2008).

10 Hsieh, D. *et al.* Observation of Unconventional Quantum Spin Textures in Topological Insulators. *Science* **323**, 919-922 (2009).

11 Rotenberg, E. First Results of the MAESTRO beamline. *ALS Users' meeting* (2016).

12 Figueroa, A. I. *et al.* Strain in epitaxial MnSi films on Si(111) in the thick film limit studied by polarization-dependent extended x-ray absorption fine structure. *Phys. Rev. B* **94**, 174107 (2016).

13 Novoselov, K. S. *et al.* Electric field effect in atomically thin carbon films. *Science* **306**, 666-669 (2004).

14 Fiori, G. *et al.* Electronics based on two-dimensional materials. *Nat. Nanotechnol.* **9**, 768-779 (2014).

15 Service, R. F. Beyond Graphene. *Science* **348**, 490-492 (2015).

16 Geim, A. K. & Grigorieva, I. V. Van der Waals heterostructures. *Nature* **499**, 419-425 (2013).

17 Li, X. S. *et al.* Large-Area Synthesis of High-Quality and Uniform Graphene Films on Copper Foils. *Science* **324**, 1312-1314 (2009).

18 Mattevi, C., Kim, H. & Chhowalla, M. A review of chemical vapour deposition of graphene on copper. *J. Mater. Chem.* **21**, 3324-3334 (2011).

19 Radisavljevic, B., Radenovic, A., Brivio, J., Giacometti, V. & Kis, A. Single-layer MoS_2 transistors. *Nat. Nanotechnol.* **6**, 147-150 (2011).

20 Li, L. K. *et al.* Black phosphorus field-effect transistors. *Nat. Nanotechnol.* **9**, 372-377 (2014).

21 Yin, J. B. *et al.* Selectively enhanced photocurrent generation in twisted bilayer graphene with van Hove singularity. *Nat. Commun.* **7**, 10699 (2016).

22 Peng, H. *et al.* Substrate Doping Effect and Unusually Large Angle van Hove Singularity Evolution in Twisted Bi- and Multilayer Graphene. *Adv. Mater.* **29**, 1606741 (2017).

23 Yuan, H. T. *et al.* Evolution of the Valley Position in Bulk Transition-Metal Chalcogenides and Their Monolayer Limit. *Nano. Lett.* **16**, 4738-4745 (2016).

24 Wilson, N. R. *et al.* Determination of band offsets, hybridization, and exciton binding in 2D semiconductor heterostructures. *Sci. Adv.* **3**, e1601832 (2017).

25 Mesaros, A., Papanikolaou, S., Flipse, C. F. J., Sadri, D. & Zaanen, J. Electronic states of graphene grain boundaries. *Phys. Rev. B* **82**, 205119 (2010).

26 Yazyev, O. V. & Louie, S. G. Electronic transport in polycrystalline graphene. *Nat. Mater.* **9**, 806-809 (2010).

27 Yu, Q. K. *et al.* Control and characterization of individual grains and grain boundaries in graphene grown by chemical vapour deposition. *Nat. Mater.* **10**, 443-449 (2011).

28 Kim, D. W., Kim, Y. H., Jeong, H. S. & Jung, H. T. Direct visualization of large-area graphene domains and boundaries by optical birefringency. *Nat. Nanotechnol.* **7**, 29-34 (2012).

29 Wang, H. *et al.* Surface Monocrystallization of Copper Foil for Fast Growth of Large Single-Crystal Graphene under Free Molecular Flow. *Adv. Mater.* **28**, 8968-8974 (2016).

30 Khomyakov, P. A. *et al.* First-principles study of the interaction and charge transfer between graphene and metals. *Phys. Rev. B* **79**, 195425 (2009).

31 Kim, H. *et al.* Activation Energy Paths for Graphene Nucleation and Growth on Cu. *ACS. Nano.* **6**, 3614-3623 (2012).

32 Rasool, H. I. *et al.* Atomic-Scale Characterization of Graphene Grown on Copper (100) Single Crystals. *J. Am. Chem. Soc.* **133**, 12536-12543 (2011).

33 Zhang, Y. F. *et al.* Defect-like Structures of Graphene on Copper Foils for Strain Relief Investigated by High-Resolution Scanning Tunneling Microscopy. *ACS. Nano.* **5**, 4014-4022 (2011).

34 Zhang, X. Y., Xu, Z. W., Hui, L., Xin, J. & Ding, F. How the Orientation of Graphene Is Determined during Chemical Vapor Deposition Growth. *J. Phys. Chem. Lett.* **3**, 2822-2827 (2012).

35 Liu, L. *et al.* Unusual role of epilayer-substrate interactions in determining orientational relations in van der Waals epitaxy. *P. Natl. Acad. Sci. USA* **111**, 16670-16675 (2014).

36 Klaver, T. P. C., Zhu, S. E., Sluiter, M. H. F. & Janssen, G. C. A. M. Molecular dynamics simulation of graphene on Cu (100) and (111) surfaces. *Carbon* **82**, 538-547 (2015).

37 Wu, P., Zhang, W. H., Li, Z. Y. & Yang, J. L. Mechanisms of Graphene Growth on Metal Surfaces: Theoretical Perspectives. *Small* **10**, 2136-2150 (2014).

38 Katoch, J., et al. Giant spin-splitting and gap renormalization driven by trions in single-layer WS_2/h-BN heterostructures. *Nat. Phys.* **1**, 335 (2018).

39 Zhu, Z. L. *et al.* Multivalency-Driven Formation of Te-Based Monolayer Materials: A Combined First-Principles and Experimental study. *Phys. Rev. Lett.* **119**, 106101 (2017).

40 Tong, Q. J. *et al.* Topological mosaics in moire superlattices of van der Waals heterobilayers. *Nat. Phys.* **13**, 356-362 (2017).

41 Cao, Y. *et al.* Unconventional superconductivity in magic-angle graphene superlattices. *Nature* **556**, 43, (2018).

42 Cao, Y. *et al.* Correlated insulator behaviour at half-filling in magic-angle graphene superlattices. *Nature* **556**, 80, (2018).

43 Costanzo, D., Jo, S., Berger, H. & Morpurgo, A. F. Gate-induced superconductivity in atomically thin MoS_2 crystals. *Nat. Nanotechnol.* **11**, 339, (2016).

44 Yu, Y. J. *et al.* Gate-tunable phase transitions in thin flakes of 1T-TaS_2. *Nat. Nanotechnol.* **10**, 270-276, (2015).

45 Goldman, A. M. Electrostatic Gating of Ultrathin Films. *Annu. Rev. Mater. Res.* **44**, 45-63 (2014).

46 Lei, B. *et al.* Tuning phase transitions in FeSe thin flakes by field-effect transistor with solid ion conductor as the gate dielectric. *Phys. Rev. B* **95**, 020503 (2017).

Chapter 5

Summary and conclusions

In this chapter, we will briefly summarize our experimental results and main conclusions in my graduate research.

In previous chapters, the three parts of my graduate research has been demonstrated in details. Here, we will give a brief review of our main achievements.

For the study on Dirac line-nodes semimetals *M*SiS (*M* = Zr, Hf):

Topological Dirac semimetals represents a new state of quantum matter that offers a platform for realizing many exotic physical phenomena. Recently, new types of Dirac semimetals with robust Dirac line nodes have been proposed that extend the bulk band linear touching from discrete point to one-dimensional lines. By using ARPES, we explored the electronic structure of the non-symmorphic crystals *M*SiS (M = Zr, Hf). Remarkably, by mapping out the band structure in the full 3D BZ, we observed two sets of Dirac line-nodes in parallel with the k_z–axis and their dispersions. Interestingly, along directions other than the line-nodes in the 3D BZ, the bulk degeneracy is lifted by SOC in both compounds with larger magnitude in HfSiS. Our work not only experimentally confirms a new Dirac line-node semimetal family protected by non-symmorphic symmetry, but also helps understanding and further exploring the exotic properties as well as practical applications of the *M*SiS family of compounds.

For the study on layered oxide semiconductor Bi_2O_2Se:

Semiconductors are essential materials in modern world that affect our everyday life. 2D semiconductors with high mobility and moderate bandgap are particularly attractive nowadays due to their potential application in fast, low power and ultra-small/thin electronic devices. In our study, we investigate the electronic structures of a new layered air-stable oxide semiconductor, Bi_2O_2Se with ultrahigh mobility (~2.8×10^5 $cm^2/V\cdot s$ at 2.0K) and moderate bandgap (~0.8eV). By combining the use of ARPES and STM techniques, we systematically mapped out its complete band structures with key parameters (e.g. the effective mass, Fermi-velocity and the bandgap, etc.). Remarkably,

the unusual spatial uniformity of the bandgap without undesired in-gap states on sample surface with up to ~50% defects makes Bi_2O_2Se an ideal semiconductor for future electronic applications. In addition, the structural compatibility between Bi_2O_2Se and interesting perovskite oxides (e.g. cuprate high transition temperature superconductors and commonly used substrate material $SrTiO_3$) further makes hetero-structures between Bi_2O_2Se and these oxides possible platforms for realizing novel physical phenomena.

For the study on square graphene system by spatially resolved ARPES:

The development of new experiment instruments is essential in facilitating the related scientific researches. Based on the general ARPES system, spatially resolved ARPES technique has been recently developed, which features the ability to focus the incident beam into submicron region. With this new technique, electronic structure of the material systems with limited geometrical sizes can be easily investigated.

By using the technique, we studied the electronic structure of square graphene sheets grown on Cu substrate. The high quality (with aligned orientation) of individual square graphene sheets as well as their merged regions is verified. By simultaneously measuring the graphene sheets and their substrate copper foil, we not only established the (001) copper surface structure, but also discovered that the square graphene sheets' sides align with the <110> copper direction, suggesting an important role of copper substrate in the growth of square graphene sheets – which will help the development of effective methods to synthesize high-quality large-size regularly shaped graphene sheets for future applications.

In addition, large-domain twisted bi-layer graphene (tBLG) was artificially constructed from the monolayer square graphene sheets. With spatially resolved ARPES system, we successfully located the sample position and studied the electronic structure

of tBLG. The van Hove singularity caused by the interlayer interaction was directly illustrated in our measurement.

Our work demonstrates the effectiveness of spatially resolved ARPES in exploring low-dimensional materials down to atomic thickness and submicron lateral size.